MODELLING MEMS DEFORMABLE MIRRORS FOR ASTRONOMICAL ADAPTIVE OPTICS

by

Célia Blain
B.Sc., Université Joseph Fourier, Grenoble, France, 2004
M.Sc., Observatoire de Paris-Meudon, France, 2005

A Dissertation Submitted in Partial Fulfillment of the
Requirements for the Degree of

DOCTOR OF PHILOSOPHY

in the Department of Mechanical Engineering

MODELLING MEMS DEFORMABLE MIRRORS FOR ASTRONOMICAL ADAPTIVE OPTICS

by

Célia Blain
B.Sc., Université Joseph Fourier, Grenoble, France, 2004
M.Sc., Observatoire de Paris-Meudon, France, 2005

Supervisory Committee

Dr. Colin Bradley, Co-Supervisor
(Department of Mechanical Engineering)

Dr. Olivier Guyon, Co-Supervisor
(Department of Mechanical Engineering)

Dr. Kim Venn, Outside Member
(Department of Physics and Astronomy)

Supervisory Committee

Dr. Colin Bradley, Co-Supervisor
(Department of Mechanical Engineering)

Dr. Olivier Guyon, Co-Supervisor
(Department of Mechanical Engineering)

Dr. Kim Venn, Outside Member
(Department of Physics and Astronomy)

ABSTRACT

As of July 2012, 777 exoplanets have been discovered utilizing mainly indirect detection techniques. The direct imaging of exoplanets is the next goal for astronomers, because it will reveal the diversity of planets and planetary systems, and will give access to the exoplanet's chemical composition via spectroscopy. With this spectroscopic knowledge, astronomers will be able to know, if a planet is terrestrial and, possibly, even find evidence of life. With so much potential, this branch of astronomy has also captivated the general public attention.

The direct imaging of exoplanets remains a challenging task, due to (i) the extremely high contrast between the parent star and the orbiting exoplanet and (ii) their small angular separation. For ground-based observatories, this task is made even more difficult, due to the presence of atmospheric turbulence. High Contrast Imaging (HCI) instruments have been designed to meet this challenge.

HCI instruments are usually composed of a coronagraph coupled with the full on-axis corrective capability of an Extreme Adaptive Optics (ExAO) system. An efficient coronagraph separates the faint planet's light from the much brighter starlight, but the dynamic boiling speckles, created by the stellar image, make exoplanet detection

impossible without the help of a wavefront correction device.

The Subaru Coronagraphic Extreme Adaptive Optics (SCExAO) system is a high performance HCI instrument developed at Subaru Telescope. The wavefront control system of SCExAO consists of three wavefront sensors (WFS) coupled with a 1024-actuator Micro-Electro-Mechanical-System (MEMS) deformable mirror (DM).

MEMS DMs offer a large actuator density, allowing high count DMs to be deployed in small size beams. Therefore, MEMS DMs are an attractive technology for Adaptive Optics (AO) systems and are particularly well suited for HCI instruments employing ExAO technologies. SCExAO uses coherent light modulation in the focal plane introduced by the DM, for both wavefront **sensing** and **correction**. In this scheme, the DM is used to introduce known aberrations (speckles in the focal plane), which interfere with existing speckles. By monitoring the interference between the pre-existing speckles and the speckles added deliberately by the DM, it is possible to reconstruct the complex amplitude (amplitude and phase) of the focal plane speckles. Thus, the DM is used for wavefront sensing, in a scheme akin to phase diversity.

For SCExAO and other HCI systems using phase diversity, the wavefront compensation is a mix of closed-loop and open-loop control of the DM. The successful implementation of MEMS DMs open-loop control relies on a thorough modelling of the DM response to the control system commands. The work presented in this thesis, motivated by the need to provide accurate DM control for the wavefront control system of SCExAO, was centred around the development of MEMS DM models.

This dissertation reports the characterization of MEMS DMs and the development of two efficient modelling approaches. The open-loop performance of both approaches has been investigated. The model providing the best result has been implemented within the SCExAO wavefront control software.

Within SCExAO, the model was used to command the DM to create focal plane speckles. The work is now focused on using the model within a full speckle nulling process and on increasing the execution speed to make the model suitable for on-sky operation.

Contents

List of Tables

List of Figures

ACKNOWLEDGEMENTS

Colin and Olivier, I want to start by thanking you both for giving me the chance to become part of the Adaptive Optics family. Olivier, for introducing me to this amazing field when I was still an undergrad student, for sharing your passion, and for initiating the chain reaction that brought me where I am today. And Colin, for welcoming me into your group and for giving me this unique opportunity to transform the Adaptive Optics world into a permanent component of my life. Thank you both for your support, patience, and leadership, for sharing your knowledge and experience, for making Victoria and Hilo my second homes away from home, and for becoming true friends along the way.

Frantz, Chris, and Vincent, thank you for the many hours you spent helping me during my stays at Subaru and for making sure I could still enjoy some of the spirit of Aloha.

Olivier (Lardière) and Dave, thank you for your patient explanations and for always creating a nice and friendly work environment.

Raphaël, I'm happy you came to live in Victoria for a little while. You have been watching over me since the first day we met at Subaru. Thanks for being a true friend, and for always being available when I need help, explanations, or a listening ear over endless shortcut lava walks.

Onur, you also watched over my shoulder when I first arrived in Victoria. Thank you for easing the transition to my Canadian life, for always being fun, and for becoming a real friend. Laurie, Kate, and Ryan, thank you for being fun office mates.

Rodolphe, thank you for your guidance and encouragements along my first few years at UVic.

Kim, thanks for your enthusiasm and for always taking an interest and following my progress.

I would also like to thank the Subaru staff members, especially Hiroshi Karoji, Hideki Takami, and Nobuo Arimoto, who have always welcomed me at Subaru and gave me the opportunity to access this exceptional telescope. I feel very lucky to have been able to spend so much time at the summit of Mauna Kea during my PhD.

Anne-Claire, Mahssa, Audrey, Seb, Floflo, Sophie, Emeric, Guillaume, and David, thanks for keeping in touch, despite the many years I spent away from France.

Jeff, thank you for your support, encouragement, patience, and love. Thank you for always finding the right words to comfort me when I needed it and for being so

much fun. Amon and Timber, thank you for being able to turn any bad day into a good one.

To my wonderful aunts, cousins, uncles and grandmother, thank you for being so caring and loving, and for being such an amazing family. It has been hard to spend all this time away from you all.

And to my parents, thank you for being the best of all possible, for always having been so supportive, understanding, and encouraging. Thank you for the infinite care and love. All of this has been possible, because of you.

DEDICATION

This is dedicated to my parents, to whom I owe everything,
Nicole Blain and *Michel Protin*,
and to my aunt,
Michèle,
for the countless hours she spent teaching me physics through my high school years.

Do there exist many worlds, or is there but a single world? This is one of the most noble and exalted questions in the study of Nature.
Albertus Magnus, 13^{th} Century.

Chapter 1

Introduction

The direct detection, imaging, and analysis of exoplanets is an exciting and active area of astronomy. The research will yield new information about the formation, evolution, diversity, categorization, and chemical composition of exoplanets. Research in the area has also captivated the interest of the general public, due to the potential of discovering the existence of other life forms in the universe.

As of July 2012, a total of 777 exoplanets were recorded[1]. The barriers to exoplanet imaging are (i) the extremely small angular separation between the primary star and the exoplanet, and (ii) the immense contrast in luminosity between the primary and the planet. As a result, most known exoplanets have been discovered using indirect detection methods, which consist of utilizing the primary stellar parameters variation (mainly luminosity variation or motion) to infer the presence of the companion.

New direct imaging techniques, commonly referred to as High Contrast Imaging (HCI), are being implemented. They consist of a combination of high efficiency instruments to extract the faint planet light from the bright stellar glare and directly image the exoplanet. Direct detection and imaging with HCI techniques will supplement the information that has been acquired on (i) the solar system planets (collected through observation and space probes) and (ii) the current sample of known exoplanets. More importantly, direct imaging is key to spectroscopic analysis.

When a coherent source illuminates an object with a surface roughness on the scale of the wavelength or when the light emitted by a distant incoherent object has prop-

agated through random inhomogeneities associated, for example, with atmospheric turbulence, the interference of the many partial waves in the reflected or propagated light (having random amplitudes and phases) produces intensity fluctuations in the final images. These intensity fluctuations consist of complex patterns of bright and dark areas[34]. Such patterns are commonly referred to as speckles.

The atmospheric turbulence above the telescope and the optics along the light path generate (i) fast and (ii) static and slowly varying optical aberrations in the wavefront. Adaptive Optics (AO) systems combine wavefront sensing, real-time software control, and adaptive optical elements to compensate for most of the fast and slow atmospheric turbulence above the telescope.

However, AO systems do not provide perfect turbulence compensation and for exoplanets located at separation from the host star of less than one arcsecond, the uncorrected (residual) static and slowly varying aberrations create speckles at the focal plane of HCI instruments. Such speckles are the current limitation to direct imaging.

Indeed, these speckles and the optical signal from an exoplanet are indistinguishable without (i) advanced post-processing techniques, such as Angular Differential Imaging (ADI)[54], Spectral Differential Imaging (SDI)[68], and Polarimetry Differential Imaging (PDI)[66], or without (ii) advanced active techniques, such as Extreme Adaptive Optics (ExAO) systems coupled with coronagraphic devices. ExAO systems are specifically designed to provide extremely precise on-axis wavefront control and are suitable for use with a coronagraph. Coronagraphs are used to reduce the star flux without lessening the flux of off-axis sources.

The most recently developed HCI systems rely on the integration of state-of-the-art AO systems with high performance coronagraphs and the implementation of algorithms dedicated to minimize focal plane speckles.

Several pathfinder instruments under development, such as the Gemini Planet Imager (GPI)[51], the Spectro-Polarimetric High contrast Exoplanet Research (SPHERE) at the Very Large Telescope (VLT)[63], and the Subaru Coronagraphic Extreme AO instrument (SCExAO)[57, 59, 41] are dedicated to reaching detection contrast levels

of up to $\sim 10^{-7}$ and detecting exoplanets of type "young Jupiter" orbiting young stars located in our solar neighbourhood (up to $\sim$ 150 parsec away).

Direct imaging exoplanet surveys will accompany the development and on-sky implementation of GPI and SPHERE. The Subaru Strategic Exploration of Exoplanets and Disks (SEEDS) survey started in October 2009 and is scheduled to use 120 nights of Subaru time over 5 years. SEEDS will examine 500 nearby young stars (distance within 200 parsec) using the combination of two of the telescope's instruments, AO188 and HiCIAO.

However, the combination "AO188-HiCIAO" cannot achieve the high Strehl ratio (the ratio of the peak intensity of the image to that of a perfect imaging system operating at the diffraction limit) targeted by SPHERE and GPI. SCExAO is, thus, under development at the Subaru Telescope to push the current exoplanet imaging limit by searching for smaller and fainter planets located close to their primary star (few AU to $\sim$100 AU). SCExAO is equipped with a 1024-actuator Micro-Electro-Mechanical-System (MEMS) deformable mirror (DM), a high efficiency Phase-Induced Amplitude Apodized (PIAA) coronagraph, and three types of wavefront sensors (WFS). The SCExAO wavefront control architecture relies on a high degree of control of the MEMS DM, combining closed-loop and open-loop control schemes to both compensate for residual atmospheric turbulence and perform speckle control in the focal plane.

The focus of this dissertation is the integration of the MEMS DMs into SCExAO and the development of a DM model that will help push the limits of SCExAO's imaging abilities.

1.1 Exoplanet traditional detection methodologies

Four main traditional techniques have been used to detect exoplanets: the radial velocity, the transit, the gravitational micro-lensing, and the timing of periodic time signatures (for example, changes in the astrometric position of the primary star). However, only the radial velocity and transit techniques resulted in a consequent number of detections.

The radial velocity technique relies on evaluating the line of sight motion of the star when influenced by the presence of an orbiting object. According to Newtonian laws of mechanics, two objects of mass M_s and M_p (with M_s as the star mass $\gg$ M_p as the planet mass) follow ellipsoidal orbits, centred on the centre of mass of the system. The star's apparent motion can, thus, be measured (i) directly using precise astrometry (when the star component is moving transversally in the sky) or (ii) indirectly using the Doppler effect[1] (when the star component is moving along the line of sight). The star's motion can then be interpreted in order to deduce information on the companion's mass and orbital properties (period, eccentricity, semi-major axis). The radial velocity technique has generated approximately 80% of the known exoplanets.

The transit technique consists of analysing the star flux variation with time. A planet passing in between the observer and the star occults a fraction of the stellar disk, producing a diminution of the flux reaching the observer. As a result, tracking periodic star flux diminutions allows one to detect the presence of a companion. The probability of finding a system with an adequate alignment of the star and the companion along the line of sight evolves as $1/a$, with a being the semi-major axis of the planetary orbit. Therefore, the quantity of exoplanets detected with the transit technique has been more limited.

The properties of exoplanets discovered with traditional methods have been constrained by the technology (see Fig. 1.1): the planets must be massive (typically 10 to 1000 times the mass of Earth) and located in the inner region of the planetary system.

To study exoplanets located at more than a few AU from the host star and to perform planetary chemical analysis, direct imaging is required.

[1]The shift of the spectral properties of a given object provides information about the star's motion. A wavelength increase (corresponding to a shift toward the red) is observed when the source moves away from the observer. Similarly, a wavelength decrease (or blue shift) is observed when the source moves toward the observer.

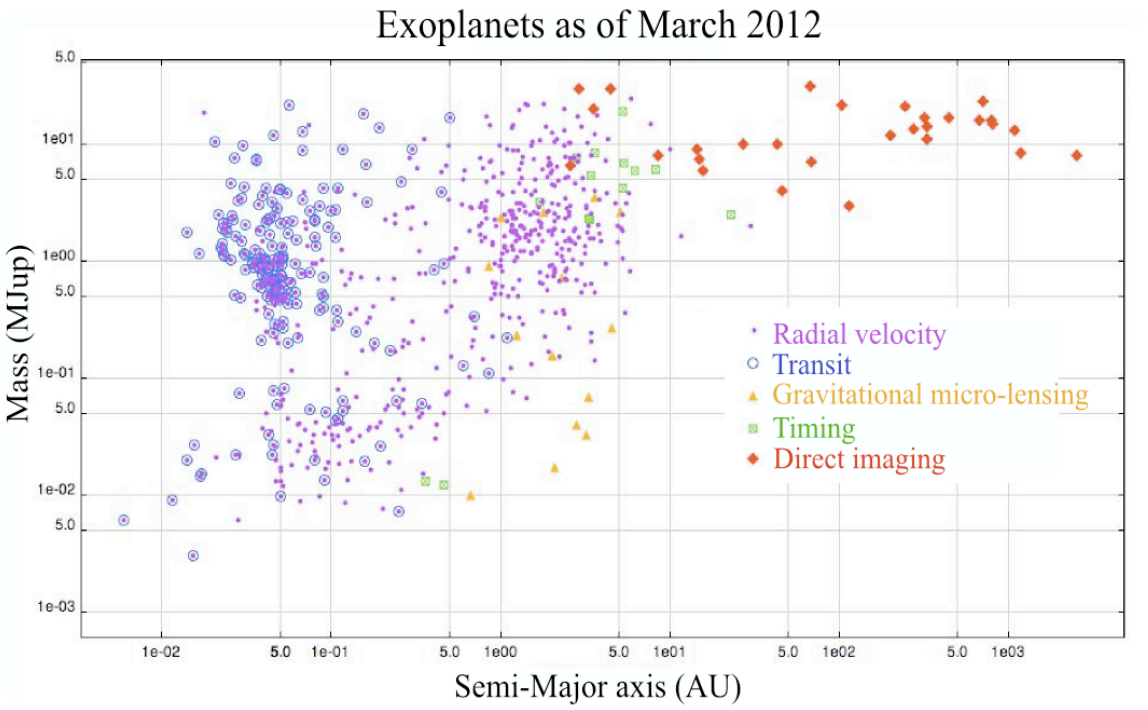

Figure 1.1: *Graphic showing the distribution of planet mass versus semi-major axis for the known exoplanets as of March 2012. The number of successful detections for each detection technique (radial velocity, direct imaging, transit, timing and micro-lensing) is specified with color markers. The radial velocity and transit techniques clearly dominate. Data have been taken from exoplanet.eu (Courtesy of Raphaël Galicher).*

1.2 Direct detection and imaging of exoplanets employing high contrast imaging

In the last decade, direct imaging of exoplanets became possible with the development of high contrast imaging techniques[55, 56].

Direct imaging will supplement information acquired on (i) the solar system planets (collected through observation and space probes) and (ii) the sample of 777 exoplanets already discovered. Access to a larger and more diversified sample of bodies will allow detailed studies of planet formation and evolution. It will also reveal the diversity of planets and planetary systems and aid in their categorization.

In addition, direct detection gives access to the planet's chemical composition via spectroscopy. Planet spectroscopic properties will be invaluable (i) to determine

planetary environmental characteristics (presence of an atmosphere or liquid water on the surface) and (ii) to detect biomarkers (specific chemical components). Eventually, spectroscopic study will help to determine, if a planet is terrestrial, and possibly even find evidence of life[65].

Many surveys complementary to the radial velocity, transit, and micro-lensing searches are planned for the next decade. Such surveys will reveal the existence of new planets located at larger angular separations and will give access to the planetary's atmosphere chemical composition. For example, the Subaru SEEDS survey will probe approximately 500 nearby solar-type or more massive young stars in the hope of detecting young giant planets. SEEDS will be able to detect planets with a mass between one and thirteen times the mass of Jupiter. The target stars have been selected in near star-forming regions and open clusters with ages spanning ∼1-10 Million years (Myr) and ∼100-500 Myr (and up to ∼1 Gyr for the oldest nearby stars), respectively.

The Subaru Telescope is a state-of-the-art 8.2-meter ground-based telescope, built by the National Astronomical Observatory of Japan (NAOJ) and located on the summit of Mauna Kea in Hawaii at 4200 m (Fig. 1.2).

Figure 1.2: *Left, the Subaru Telescope on the summit of Mauna Kea. Right, the telescope inside the dome (Courtesy of Subaru Telescope).*

1.3 Ground-based observations

1.3.1 Light propagation through the telescope

A wavefront coming from a distant star can be described mathematically in the pupil plane by the following complex function,

$$\psi = Ae^{i\phi} \tag{1.1}$$

A and ϕ are the amplitude and phase of the wavefront respectively.

The star light is collected by the instrument detector. The detector measures the light intensity I, defined by,

$$I = \mid \psi \mid^2 \tag{1.2}$$

The Point Spread Function (PSF) of an optical system is the image of a point source, defined as the squared modulus of the Fourier Transform (FT) of the pupil function ψ across the pupil. The image formed in the focal plane of the instrument detector is described in the spatial domain by the convolution of the object and the PSF.

Without central obstruction or turbulence, the telescope PSF is named the Airy disk, described as a pattern of rings of decreasing intensity and produced by Fraunhofer diffraction through a circular aperture. As illustrated in Fig. 1.3, the first dark ring (first zero on the transversal cut) is located at an angular distance of $1.22\lambda/D$.

When the PSF undergoes diffraction from the telescope and instrument's optics, the final image obtained on the detector is called "diffraction limited". For an aberration free image, the incident phase across the pupil is equal to zero ($\phi = 0$ in Eq. 1.1). A diffraction-limited image is the best theoretical image that can be obtained with a given optical system when no disturbances occur.

The diffraction limit or spatial resolution of the telescope, R_d, is usually given in arcsec and is defined by the full width half max (FWHM) of the Airy disk,

$$R_d = 1.02\,\frac{\lambda}{D} \tag{1.3}$$

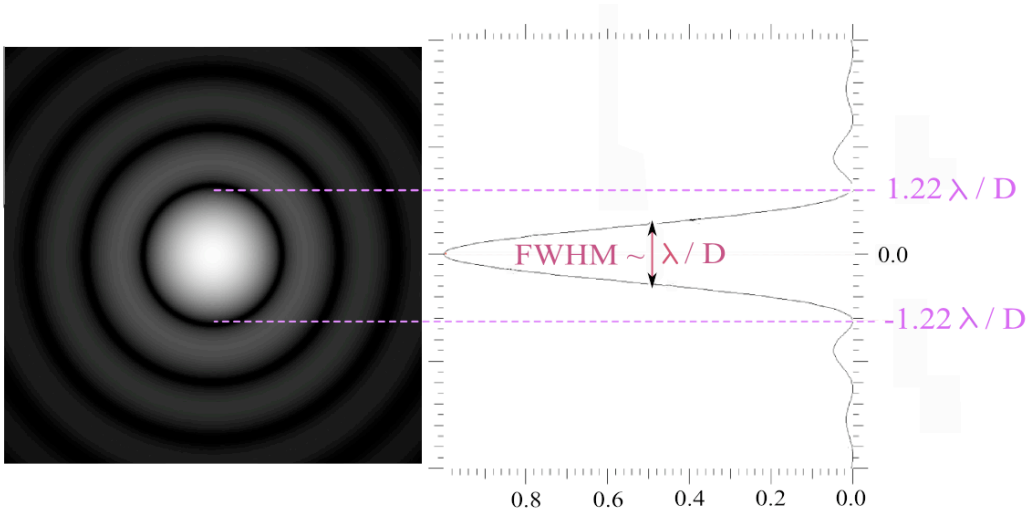

Figure 1.3: *Airy disk for a circular aperture (left) and transversal cut of the normalized intensity profile (right).*

with D the telescope aperture diameter and λ the wavelength of observation.

For a given wavelength of observation, increasing the primary mirror diameter (thus increasing the spatial resolution) will allow the detection of exoplanets located closer to the star.

1.3.2 Optical aberration created by the atmosphere

The atmosphere is the thin layer of gases retained by the Earth's gravity. The effect of the atmospheric turbulence on celestial lights is challenging for ground-based telescopes with primary mirror diameters larger than the Fried parameter, which is typically 10 to 15 cm. Current ground-based telescopes with 5 to 10-meter primary mirrors and future generations of telescopes with 30 to 42-meter primary mirrors are, thus, highly affected by this phenomenon.

The air of the atmosphere undergoes turbulent mixing through wind shear and convection (see illustration in Fig. 1.4). At ground level, the heated air (represented in red) rises into upper colder air cells (shown in blue), expands, and continues to rise while the colder air cells descend toward the ground. The high winds, especially the ones associated with the jet stream, participate in this turbulent mixing and large

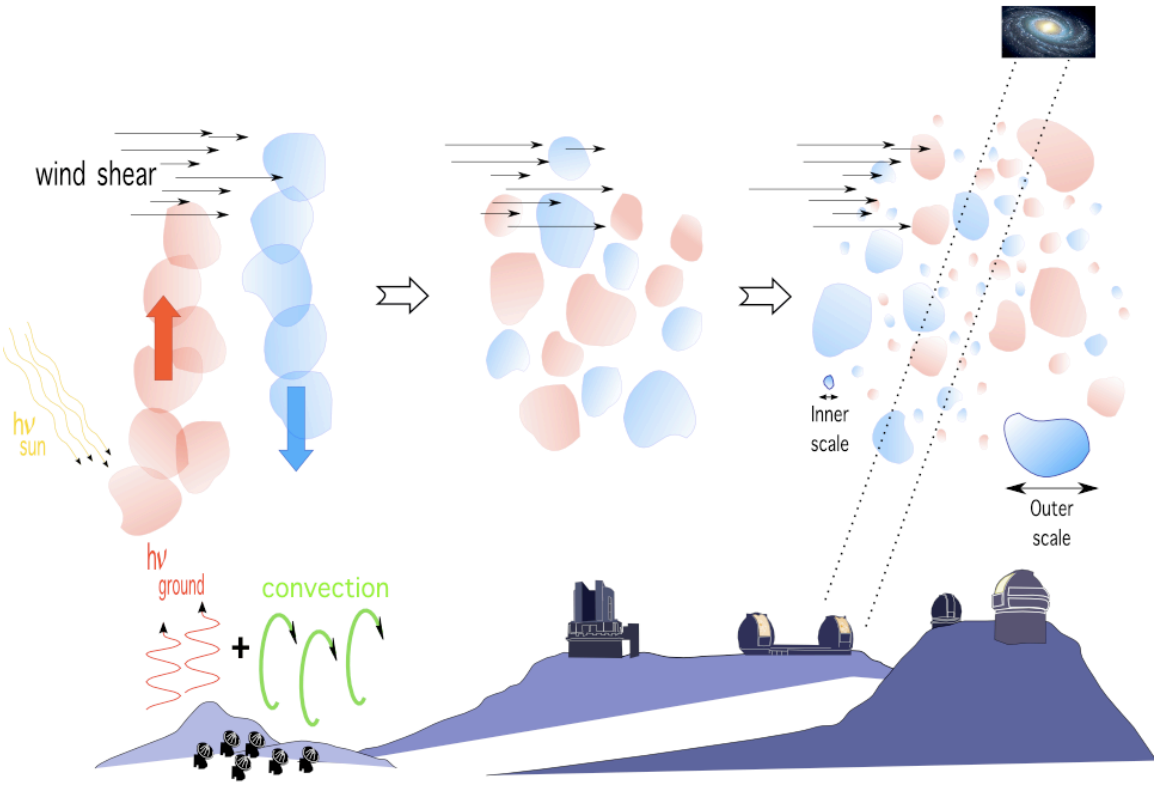

Figure 1.4: *Illustration of the turbulent mixing phenomenon in the Earth's atmosphere.*

cells break down into smaller cells through wind sheer and friction.

The optical refractive index of a specific cell is dependent on its conditions of pressure and temperature[2]. The atmosphere can, thus, be described as a moving mix of cells of various sizes, pressure, and temperature. The light passing through several cells will, thus, encounter different refractive indices. The speed of light is tied to the optical refractive index. Variations in the optical refractive index induce phase fluctuations, or delay, across the parallel-plane wavefront that passes through the atmosphere.

An aberrated wavefront can be written as the following complex function,

$$\psi_{turb} = \psi \; . \; A_{turb} \; e^{i\phi_{turb}} \tag{1.4}$$

[2]Since the atmosphere is mostly in pressure equilibrium on small scales, only the fluctuations in temperature really matter as they trigger fluctuations in density.

where ψ is defined by Eq. 1.1, and A_{turb} and ϕ_{turb} are the amplitude and phase distortion due to the turbulence, respectively.

The Kolmogorov model, commonly used to describe atmospheric turbulence, describes the Fried parameter r_0 as an indication of the strength of the phase fluctuations. Indeed, r_0 corresponds to the diameter of a circular telescope aperture, for which the atmospheric phase perturbations begin to limit the image resolution, typically, 10 to 15 cm in the visible wavelengths. According to this model, for a telescope aperture diameter larger than r_0, the telescope spatial resolution becomes,

$$R_{turb} = \frac{\lambda}{r_0} \tag{1.5}$$

For an aberrated image, the phase component of the complex amplitude function across the pupil does not equal zero. The theoretical unaberrated Airy disk pattern is altered and the light coming from the on-axis star is scattered randomly around the image centre in a wide halo.

Compensating for turbulence effects and optical aberrations from the telescope's and instrument's optics is, thus, a first critical step toward direct detection of exoplanets. The technical solution, named Adaptive Optics, was first proposed in the 1950's[7]. AO technologies have been extensively developed for astronomical purposes since the 1990's and each 10-meter class telescope is now equipped with an Adaptive Optics system.

1.4 Subaru's facility AO system

Subaru is an altitude-azimuth telescope equipped with four foci: Prime, Cassegrain and two Nasmyths. The IR-dedicated Nasmyth focus is equipped with AO188, an AO facility instrument dedicated to compensate phase aberrations generated by the atmospheric turbulence and optical defects along the light path.

Subaru's AO188 system, illustrated in Fig. 1.5, is composed of the following major

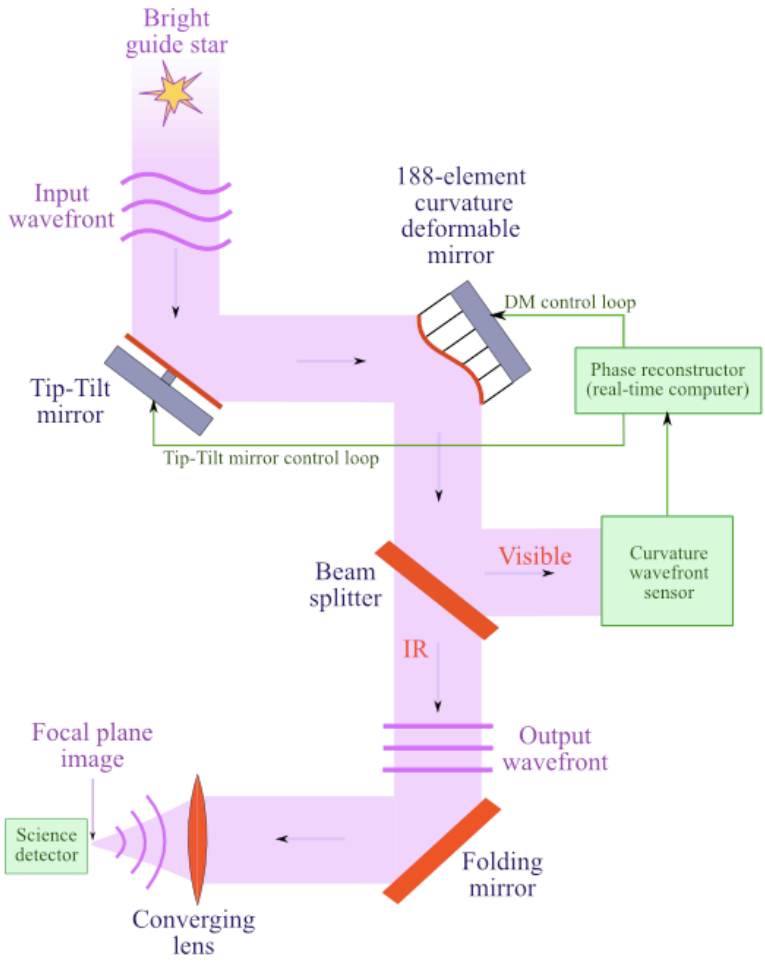

Figure 1.5: *Schematic of Subaru's AO188.*

subsystems:

- A bright on-axis natural guide star (NGS) provides light to measure the wavefront aberrations.

- A tip-tilt mirror (TTM) corrects the low order/high power tip and tilt modes of the turbulence (see Appendix A).

- A 188-element bimorphe curvature deformable mirror provides phase modulation through the action of sandwiched piezoelectric materials poled through the thickness. Electrodes are uniformly distributed along the device and a reflective coating is applied on the front face of the disk. A voltage applied to the electrode creates a local electric field through the thickness of the device.

The resulting piezoelectric effect causes the electrode to expand or contract in the area and, therefore, the device curves over the actuated area[27]. The commands sent to the DM actuators shape the DM surface to restore the wavefront parallel-plane properties after reflection onto the DM.

For a pupil function ψ defined by Eq. 1.1, the complex conjugate function $\overline{\psi}$ can be written as,

$$\overline{\psi} = Ae^{-i\phi} \tag{1.6}$$

where $e^{-i\phi}$ represents the phase term of the complex amplitude function.

Analytically, adding the phase component of ψ to the phase component of the complex conjugate function results in the cancellation of the phase term. An aberrated wavefront (a complex amplitude function for which the phase term, $e^{i\phi}$ does not equal one) can, thus, be corrected by implementing this addition using the AO system.

The deformable mirror is the element of the AO system that physically implements the phase addition using the principle of phase conjugation, illustrated in Fig. 1.6. The incident light (in purple) comes from the top and is reflected onto the DM. When the DM is flat (left image), the direction of propagation is reversed, but the phase component on the reflected wavefront (in yellow) is identical. When the DM is actuated (right image), the phase component in the reflected wavefront is cancelled and the wavefront parallel-plane property is recovered.

The shape applied to the DM creates phase delays in different locations of the incoming beam. These phase delays correspond to a modification of the light optical path length on each point and, after reflection onto the DM surface, the wavefront phase term, $e^{i\phi}$, is reduced to one. Using measurements of the pupil plane wavefront, the phase aberrations are estimated and the DM is shaped to add an optical aberration to the incident wavefront corresponding to only half of the magnitude of the shape of the incoming wave.

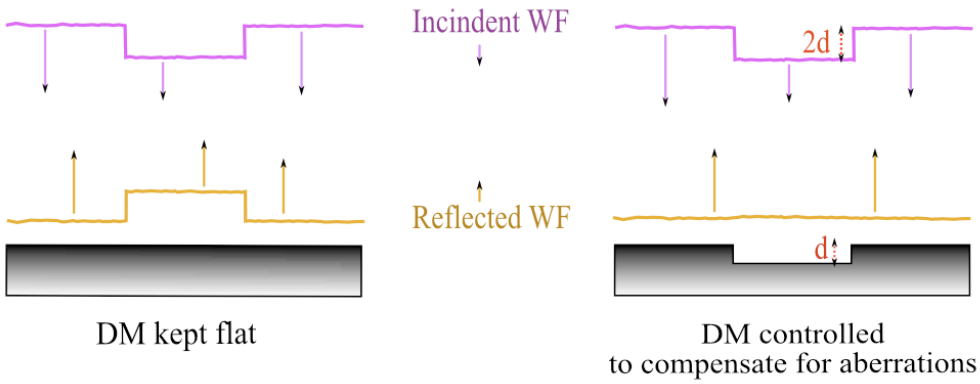

Figure 1.6: *Illustration of the principle of phase conjugation using a deformable mirror.*

The DM has a limited number of actuators N_{act} and, therefore, can only correct a limited number of modes. As a result, the correction of the wavefront is not perfect.

With N_{actlin} the linear number of actuator (number of actuators across the DM), the highest spacial frequency corresponding to the highest order aberration to be corrected by the DM is defined by,

$$F_{max} = \frac{N_{actlin}}{2D} \tag{1.7}$$

with D, the pupil diameter.

The DM corrects only for a limited number of spatial frequencies ($\leq F_{max}$). The uncompensated spatial frequencies will induce speckles in the focal plane and spread energy on the detector. DMs with a high density of actuators are, thus, preferable for high performance ExAO systems.

• A curvature wavefront sensor measures the wavefront aberrations (wavefront sensing). A beam splitter is inserted into the light path. The visible wavelengths from the guide star light are directed towards the WFS, while the infrared wavelengths are sent to the science detector.

• A real-time computer (RTC) (the control system) (i) analyses the wavefront

information collected by the WFS to deduce the phase information (wavefront reconstruction), then (ii) converts the phase aberrations into commands to send to each actuator of the deformable mirror (wavefront correction). The DM, WFS and RTC interact in a closed-loop fashion. In a closed-loop configuration, the DM is located upstream of the WFS, allowing the WFS to see the DM response to commands sent by the control computer. The feedback between the DM and the WFS allows for readjustment of the DM commands between iterations in order to both (i) compensate the current measured phase aberrations and (ii) check the DM shape to detect and correct possible miscalculations or previous measurement errors.

The iterative process between DM motion and WFS measurements requires a finite amount of executing time which is defined as the control frequency. The effect on the image is not instantaneous and the lag is the cumulative effect of (i) the wavefront measurement and analysis by the WFS, (ii) the control system computation time to convert the phase information into DM commands, (iii) the data transfer between the control system and the DM, and (iv) the DM response.

The DM response is fast and usually considered negligible in the estimation of the control frequency. The closed-loop control frequency must be fast enough for the AO system to compensate for the turbulence-induced aberrations. The closed-loop bandwidth must be comparable to one over the coherence time, otherwise the phase correction applied by the DM corresponds to a wavefront shape that no longer exists. To follow the turbulence in real time and provide an efficient wavefront correction, current AO systems typically run at frequencies equal or greater than 500 Hz.

• A science detector (SD), typically a high-resolution camera or a spectrograph, records the final image or spectrum.

The combined action of the TTM, DM, WFS and RTC is designed to remove the incoming wavefront aberrations in order to restore the original parallel-plane wave-

front's property on the SD.

AO188 is a classical single conjugated AO (SCAO) system, in which the DM is optically conjugated to the ground layer of turbulence. Leaving AO188, the wavefront contains uncompensated residual aberrations of $\backsim$200 nm rms.

Sec. 1.5 describes how the residual slowly varying and static aberrations limit the detection and imaging capabilities of HCI instruments by creating speckles, in the planet research area, which can hide or be mistaken for a planet. AO188's wavefront aberration compensation level is not sufficient to reach the high contrast level required for planet imaging. A deeper layer of correction is, thus, needed and high contrast imaging instruments, such as SCExAO, become critical.

1.5 High contrast imaging

1.5.1 Limitations to high contrast imaging

The angular separation between the planet and the primary star is very small ($\sim$0.1 arcsec for an Earth-like planet and 0.5 arcsec for a Jupiter-like planet for a system located at 10 parsec) and the typical luminosity contrasts between the star and an exoplanet range from 10^{-4} to 10^{-10}. As a result, when observed with a telescope from Earth, the light of the faint exoplanet appears hidden in the glare of the bright primary star.

Fig. 1.7 illustrates the difficulty behind direct exoplanet detection. The residual starlight intensity obtained with a classical AO system is represented by the red continuous plot. Well below, the residual planet intensity is represented by the dashed purple plot. The zero on the horizontal axis represents the centre position of the star with the planet located at an angular separation of 0.5 arcsec. To detect the planet, the residual starlight intensity level after calibration/subtraction must be brought below the residual planet's intensity level. The dark orange dashed plot represents how high contrast imaging (combining AO and PSF calibration) alters the residual star's PSF in order to bring the residual star intensity level below the residual planet intensity level.

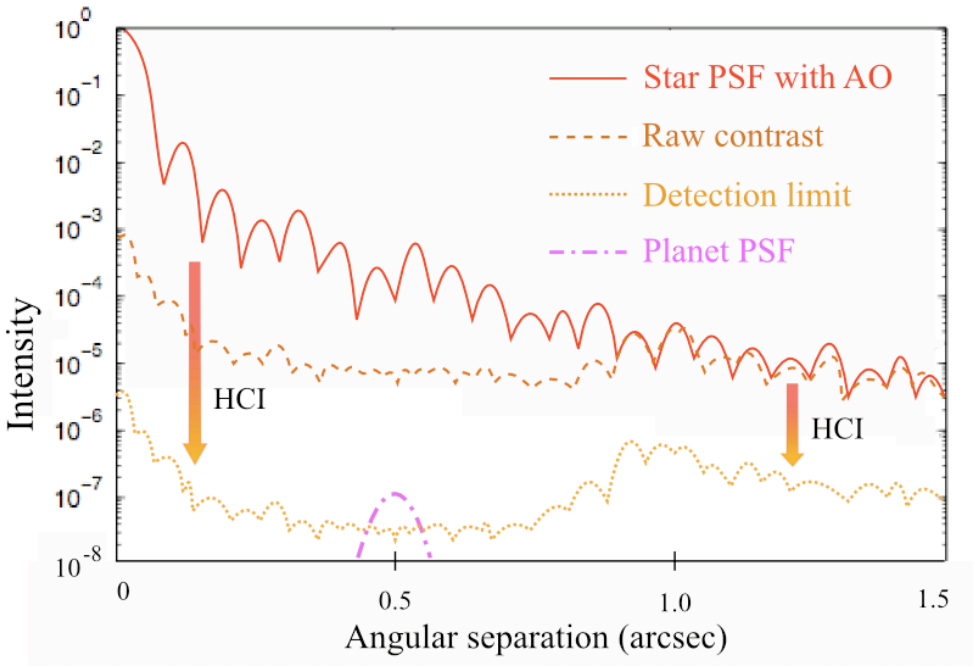

Figure 1.7: *Illustration of the effect of high contrast imaging techniques on the star PSF.*

For ground-based observations, using AO allows the compensation of most of the aberrations generated by atmospheric turbulence and optical defects on the telescope and instruments. Many astronomical science targets, whose study relies on ground-based observations and thus suffer from wavefront distortions, greatly benefit from the level of correction provided by classical AO systems. However, Fig. 1.7 shows direct detection of exoplanets puts much more severe constraints on the wavefront correction level and exceeds what can be provided by classical AO.

Leaving the AO system, the beam still contains unseen, thus, uncompensated slowly varying and quasi-static wavefront aberrations that evolve over time scales of minutes to hours. These residual wavefront errors are created by (i) non-common path aberrations (NCPA) in the instrument's optics and (ii) by a small fraction of uncompensated slowly varying components of the atmospheric turbulence. NCPAs are aberrations in the optical path not seen by the wavefront sensor. For example, this phenomenon occurs in classical AO systems where the science camera and the wavefront sensor are on different optical paths, as illustrated in Fig. 1.5 for AO188.

Speckle noise arises from random intensity patterns produced by the mutual interference of a set of wavefronts, which are due to rapid atmospheric phase fluctuations. For long exposure images, perfectly static aberrations create speckles that can be measured once during the observation and removed later with post-processing techniques. Fast varying speckles average out to a smooth floor and add photon noise in the final image. The temporal evolution of the slowly varying and quasi-static wavefront errors is such that the resulting artifact speckles become a significant source of speckle noise and, as a result, must be sensed and corrected directly during a science observation. The exposure time has a great impact on which speckles will contribute to the speckle noise on the final image. For short exposure time, all speckles are frozen and contribute to the speckle noise. For an exposure time T, only the speckles evolving over a period longer than T contribute to the speckle noise.

Slow and quasi-static aberrations are, thus, the current limiting factor that compromise unambiguous direct planet detection. Indeed, such aberrations diffract and scatter the starlight and result in partially coherent starlight interfering at various angles of arrival. Such interferences, named artifact speckles in the following, are copies of the unaberrated star PSF. Located at various discrete locations in the image plane, they can be easily misidentified as planets[53], thus compromising an unambiguous planet detection.

1.5.2 Coupling ExAO to coronagraphy

Direct detection of exoplanet is only possible, if the light distribution in the final PSF has been altered in a way that brings the residual planet light to a detectable level.

The schematic in Fig. 1.8 gives an overview of the high contrast imaging process by showing the evolution of the star PSF on the detector after the different levels of correction.

As illustrated, several levels of wavefront correction are, thus, necessary and consist roughly of the following four steps:

- Perform a first level of compensation to gather the starlight spread over the wide halo and recover a Airy disk-like PSF. This can be performed by an AO

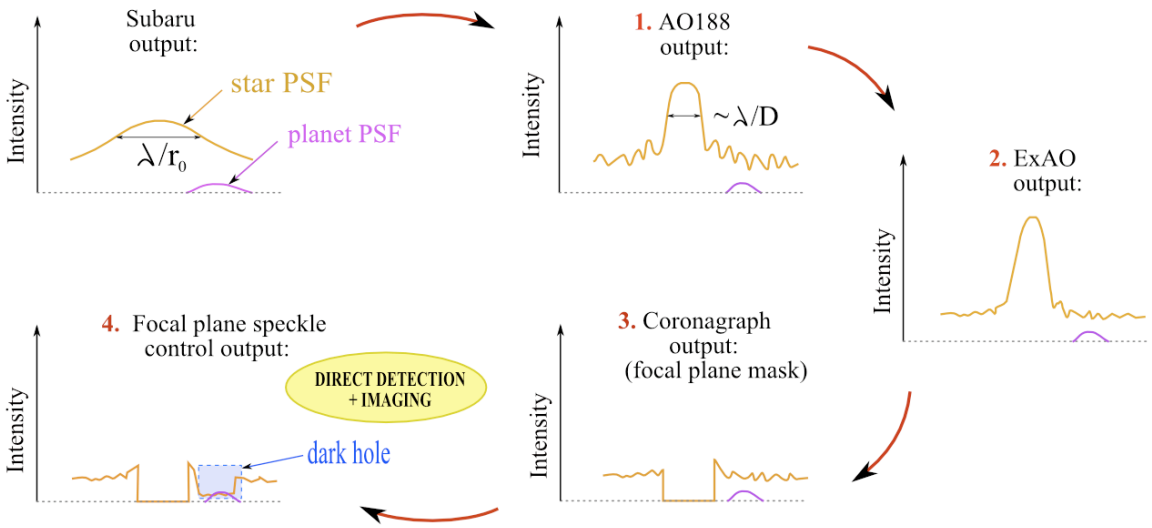

Figure 1.8: *Overview of the high contrast imaging process.*

system like AO188 (step 1. in Fig. 1.8).

• Concentrate the starlight inside the core of the Airy-disk using ExAO (step 2. in Fig. 1.8).

• Obscure the light of the primary star using a high efficiency coronagraph (step 3. in Fig. 1.8).

• Using ExAO, add a deeper level of correction in a targeted zone in which each slowly varying and quasi static artifact speckle is probed and removed, leaving only the signal from a real companion to shine through (step 4. in Fig. 1.8).

We note that the residual planet light may still be fainter than the residual star light, even after all the steps described above and, therefore, a successful detection could require additional post processing and calibration.

In order to (i) overcome the very high luminous ratio and the small angular separation between the planet and the primary star and (ii) minimise the slow and quasi static speckles, which significantly reduce the dynamic range, high contrast imaging instruments are designed as a combination of (i) a high performance coronagraph, which reduces the diffracted starlight (bright diffraction rings and halo) at the planet

location and (ii) an ExAO system, which uses a DM and focal plane speckle control algorithms to create a targeted region in the image, the dark hole, where the intensity level of the slow and quasi static artifact speckles are brought below the planet residual intensity level. The dark hole is visible on the right image in Fig. 1.9. We note that in this figure, the contrast values (color bars) are not representative of expected on-sky performance. The focal plane speckle control process will be described in more detail in Sec. 1.5.3.

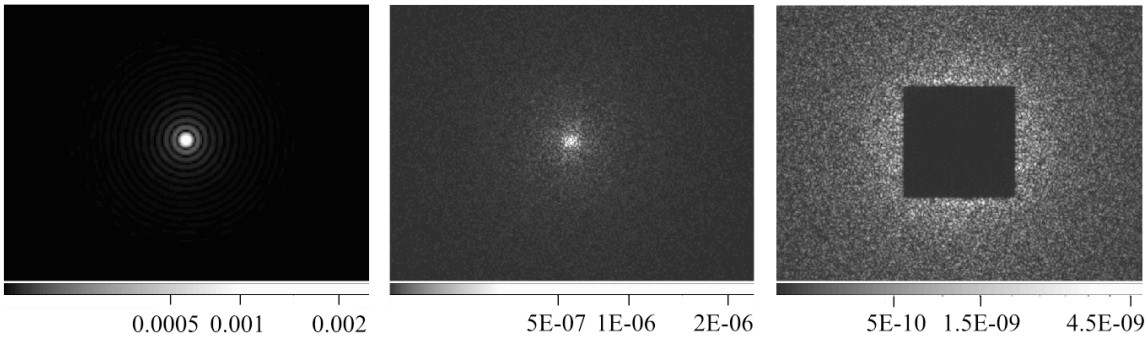

Figure 1.9: *Left, image obtained without the coronagraph. Middle, image obtained with the coronagraph. Right, image obtained with the coronagraph and the DM, showing the creation of the dark hole area (Courtesy of Raphaël Galicher).*

Even relatively high-order AO systems (using a DM with a large number of actuators) do not yield a perfect correction and ExAO systems, such as SCExAO, become necessary to perform further wavefront correction and create the dark hole area. The achievable contrast is directly related to the quality of the wavefront. Thus, obtaining the desired high contrast in the dark hole puts demanding requirements on the wavefront control system.

In contrast to what is done with traditional AO systems, ExAO instruments can perform focal plane speckle control and simultaneously use their DM for wavefront correction and wavefront sensing purposes. Indeed, once most of the low and high order aberrations ($\leq F_{max}$), due to atmospheric turbulence and instrument's NCPAs, have been removed by the AO188 and the ExAO systems, the beam is left with static and slowly varying aberrations generating artifact speckles in the focal plane. The final step for the direct detection and imaging of exoplanets, thus, relies on measuring and compensating for these residual speckles to create the speckle-free zone: the dark

hole.

1.5.3 Focal plane speckle control

Probing and removing speckles, based on interferometric subtraction techniques, rely on the proper use of the speckle spatial coherence property. Indeed, unlike the light from the companion planet, the artifact residual speckles arising from the light of the primary star are coherent with it. Superimposing artificially generated anti-speckles on the artifact speckles can allow for the efficient removal of the artifact speckles.

Several speckle control schemes are possible, for example, using the Electric Field Conjugation (EFC)[20, 32, 33] or iterative speckle nulling methods [52], or using the Self-Coherent Camera (SCC) approach[9, 28, 29, 30]. All schemes rely on the same theoretical background.

Assuming one wants to test the light, in a given location of the focal plane image, in order to check if this light comes from a genuine structure or is simply a residual speckle. The light from the core of the PSF must be sent to this location (a speckle from the core PSF is artificially added to the light at this location). The two "light samples" are defined by the complex amplitudes $\psi_1(t) = A_1(t)\ e^{i\phi_1(t)}$ and $\psi_2(t) = A_2(t)\ e^{i\phi_2(t)}$.

If the light samples are spatially coherent, interference fringes will be formed. The on-axis intensity *I(t)* in the focal plane is given by the superposition of the waves (the sum of the complex amplitudes),

$$\begin{aligned} I(t) &= \mid \psi_1(t) + \psi_2(t) \mid^2 \\ &= \mid \psi_1(t) \mid^2 \ + \ \mid \psi_2(t) \mid^2 \ + 2 \mid \psi_1(t) \mid\mid \psi_2(t) \mid cos(\phi_2(t) - \phi_1(t)) \end{aligned} \tag{1.8}$$

where $2 \mid \psi_1(t) \mid\mid \psi_2(t) \mid cos(\phi_2(t) - \phi_1(t))$ represents the interference between the two light samples.

If the two light samples are incoherent (if the light at this location comes from an

exoplanet), they cannot interfere and the intensity *I(t)* in the focal plane is the sum of their intensities only,

$$I(t) \;=\; |\,\psi_1(t)\,|^2 \;+\; |\,\psi_2(t)\,|^2 \tag{1.9}$$

To probe the artifact speckles, the DM is used to introduce a diversity in the wavefront, while a camera records its impact on the final focal plane image. Indeed, speckles can be created in the focal plane by applying a sinusoid shape on the DM surface. Such "DM-generated" speckles will be coherent with the starlight as they are produced by reflecting a portion of the starlight onto the DM. One can thus interfere DM-generated speckles with the existing artifact speckles (Eq. 1.8). By monitoring these interferences, it is possible to reconstruct the complex amplitude (amplitude and phase) of the focal plane speckles.

Once the artifact speckles have been sensed, the DM can be used to generate anti-speckles to be superimposed onto the artifact speckles and clear the area from any artifact speckle. The DM is, thus, used for (i) speckle probing (wavefront sensing), in a scheme akin to phase diversity and (ii) speckle suppression (wavefront correction).

If the star has a companion, the DM-generated speckles and the exoplanet light will be incoherent and will not interfere destructively. When the speckle probing and suppressing process is completed, any structure left in the area should unambiguously indicate the presence of an exoplanet.

Using the DM to create the dark hole and reduce artifact speckles below the planet level has been successfully implemented in several laboratory experiments[71, 72]. This scheme has been implemented in SCExAO wavefront control systems as the core strategy to reach high contrast. The first laboratory experiment with SCExAO achieved a raw contrast in the dark hole area of up to 10^{-4}[44].

Fig. 1.10 shows an example of high contrast results achieved with SCExAO using a simple speckle nulling control loop[58]. The dark hole area is indicated by the black rectangular box. Panel (a) shows the starting point of the loop, with the DM in its nominal flat-map configuration. Note that in addition to some low-spatial frequency

aberrations (created by a static turbulence plate), most of the speckles present at the starting point are located along the diffraction spikes created by the spider arms of the telescope pupil. Panel (b) shows the result of 50 speckle nulling iterations, working on up to 10 speckles at a time. Most speckles present in the dark hole area before running the speckle nulling loop have disappeared in image (b).

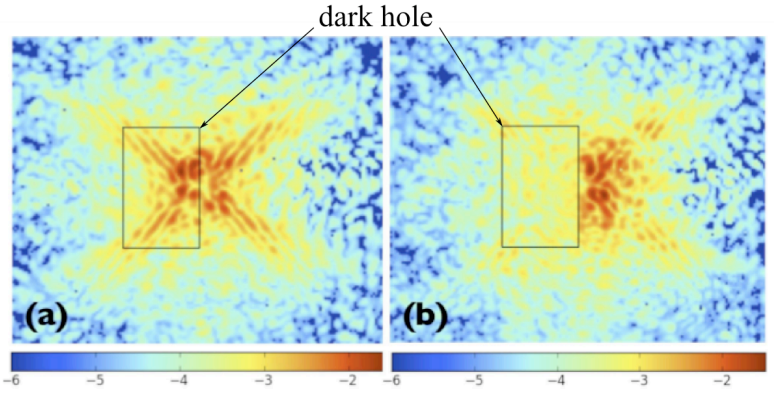

Figure 1.10: *Example of a high contrast result obtained with SCExAO using a simple speckle nulling control loop (Courtesy of Frantz Martinache).*

1.5.4 The Subaru Coronagraphic Extreme Adaptive Optics system

SCExAO[44] is a versatile platform allowing the rapid investigation of new techniques related to coronagraphy, wavefront sensing technologies, and high contrast direct imaging of exoplanets. SCExAO is built on a small optical bench (∼1.2 x 0.9 meters) located on the infrared Nasmyth platform and is designed to be inserted between two of Subaru Telescope's instruments, AO188[60] and HiCIAO (see Fig. 1.11). SCExAO is located behind AO188. After a first level of wavefront correction provided by AO188, SCExAO performs further wavefront correction and calibration before redirecting the beam to HiCIAO's near-IR camera[70], specifically designed for high contrast imaging.

The main system components of SCExAO are a 1024-actuator MEMS DM, a PIAA coronagraph[35], a Coronagraphic Low Order WFS (CLOWFS)[43], a Non-Linear Curvature WFS (NLCWFS)[37], and a Focal Plane WFS (FPWFS)[38, 42].

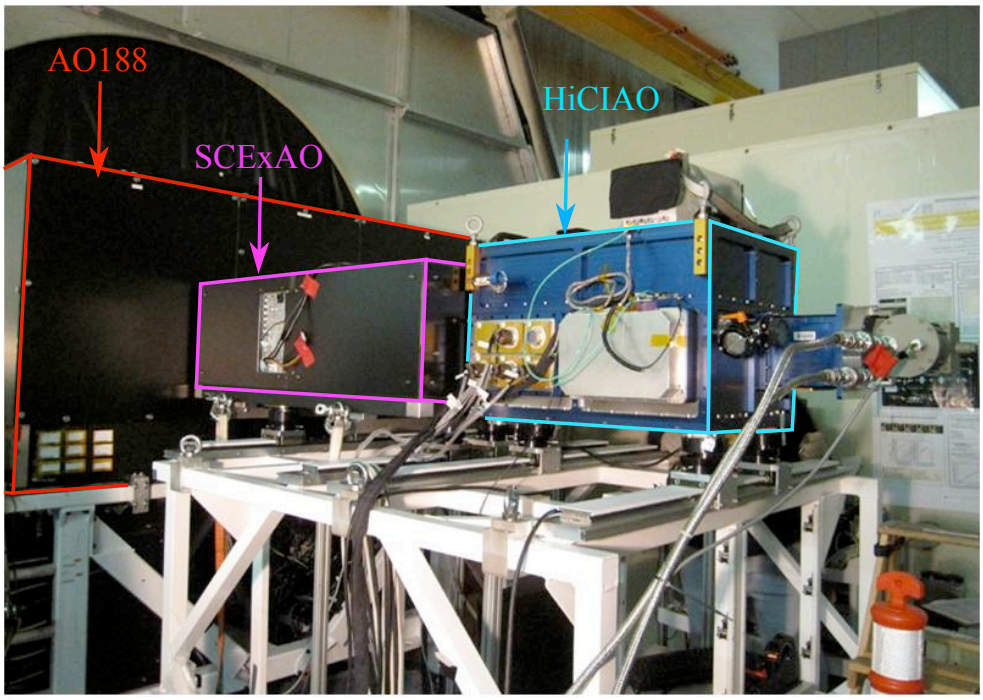

Figure 1.11: *SCExAO set on the Subaru Nasmyth platform between AO188 and HiCIAO (Courtesy of Subaru Telescope).*

Wavefront aberrations, commonly described using Zernike polynomials (see Appendix B), can be grouped into (i) "low order/high power" aberrations (tip and tilt), (ii) "high order/low power" aberrations (focus, astigmatisms, coma...), and (iii) static and slowly varying aberrations. The wavefront control architecture of SCExAO[41] provides a high level of correction to all three types. The CLOWFS is used to remove the residual low order aberrations, the NLCWFS is dedicated to the residual high-order aberrations and the FPWFS is used to perform the speckle control using phase diversity. Each wavefront sensor sends commands to the MEMS DM to optimize the wavefront quality and reach the highest possible contrast in the dark hole area. A schematic of the wavefront control interface is given in Fig. 1.12.

Accurate wavefront sensing and correction requires a highly accurate model of the MEMS DM. In that sense, I have investigated several modelling approaches to quickly and accurately compute MEMS DM shapes. An enhanced model, described in Chap. 4 provides the best performance. Following an initial laboratory demonstration at the University of Victoria (UVic) Adaptive Optics Laboratory (AO Lab)[16], this model has been integrated into SCExAO's wavefront control system in order to

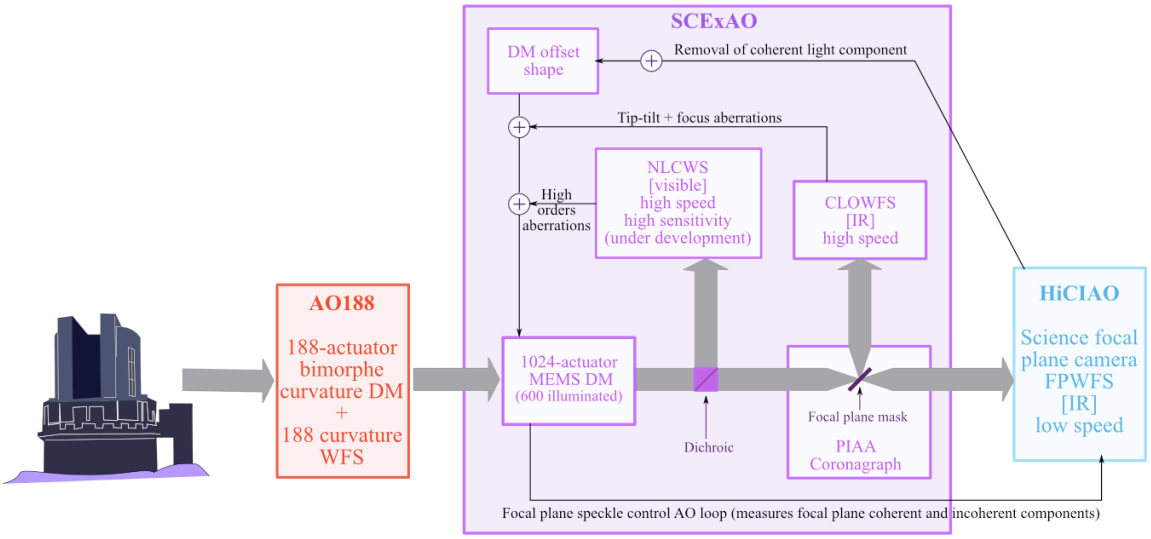

Figure 1.12: *Schematic of the wavefront control interface in SCExAO.*

perform further evaluation.

1.6 Thesis overview

This dissertation presents the development, analysis and experimental evaluation of two MEMS DM models that could be suitable for use within the wavefront control system of an extreme adaptive optics system.

The structure of the remaining dissertation is outlined below.

Chapter 2

The challenges of closed-loop control versus open-loop control methods are compared. The operation and integration of MEMS deformable mirrors within an adaptive optics system are described.

Chapter 3

An investigation into the non-additivity of MEMS DM actuator influence functions is performed. The development of a new, experimentally based modelling approach (referred to as *Mod1*) suitable for utilizing the MEMS DM in an open-loop control

architecture is reported.

Chapter 4
An alternative enhanced modelling approach is developed. This model, referred to as *Mod2* is partially based on the characterisation of some of the DM properties. *Mod2* is also partially based on the forces present during DM operation. The model is integrated into an iterative algorithm and open-loop tests are performed on a 1024-actuator MEMS DM. The results are compared with *Mod1* and recent modelling approaches developed by other research groups.

Chapter 5
The *Mod2* model and algorithm are implemented into the SCExAO wavefront control software. *Mod2* is used to create DM-generated speckles in the focal plan of SCExAO. The results regarding the speckles intensity properties are reported and suggest that *Mod2* could improve SCExAO speckle control performance.

Chapter 6
A comparison of the performance obtained with *Mod1* and *Mod2* is reported. The chapter concludes by developing on the next steps that will be taken (i) to test *Mod2* performance in a speckle nulling scheme and (ii) to improve the model/algorithm speed.

The above research has been reported in refereed journal publications[18, 16] and also presented at international instrumentation conferences[17, 13, 19, 15].

Chapter 2

Modelling deformable mirrors for adaptive optics systems

Deformable mirrors are composed of a flexible reflective membrane deposited atop an array of actuators. As a light beam is reflected by the reflective membrane, the array of actuators can be controlled to create phase delay in specific areas and perform wavefront correction (as illustrated in Fig. 1.6). The typical parameters used to describe a DM's performance are listed below.

Number of actuators:

The number of actuators, related to the size of the telescope, is a critical parameter. For a 8-meter class telescope, a few hundred actuators are sufficient to achieve diffraction limited imaging in near-infrared. For the next generation of 30-meter class telescopes, this number will need to be scaled up to a few thousand. The number of actuators required also depends on the performance to be achieved by the instrument. Providing correction for the higher order modes will require a larger number of actuators. Actuators can be arranged by rows and columns in a square array (Fig. 2.1 (a)), or radially in a circular array (Fig. 2.1 (b)). A radial organisation is preferable for curvature DMs. The actuator pitch defines the distance between two adjacent actuators.

Actuator properties:

The maximum stroke is the actuator's vertical displacement motion when the maximum rated voltage is applied. The linearity describes the change in an

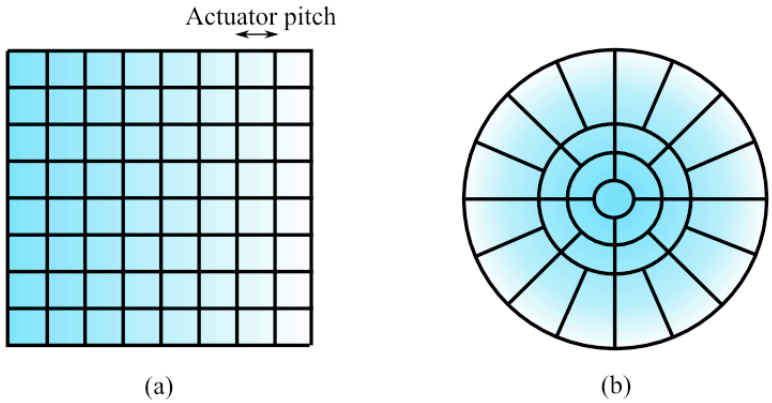

Figure 2.1: *Illustrations of (a) a square array, (b) a circular array.*

actuator's displacement as a function of a linear change in input voltage. Hysteresis defines the dependence of the actuator's current position on its past position. The repeatability is the ability to obtain an identical stroke for a given voltage. The stability is the ability to maintain a constant behaviour and performance when the environmental parameters vary on short and long term.

The actuator influence function (IF) is the characteristic shape of the DM's response to the action of a single actuator (Fig. 2.2). It can be experimentally measured by recording the overall shape of the DM when one actuator is set to a given stroke while the rest of the actuators are left at rest. Fig. 2.2 shows the images of four influence functions obtained with a 1024-actuator MEMS DM when following this measurement procedure. Four randomly selected actuators have been poked.

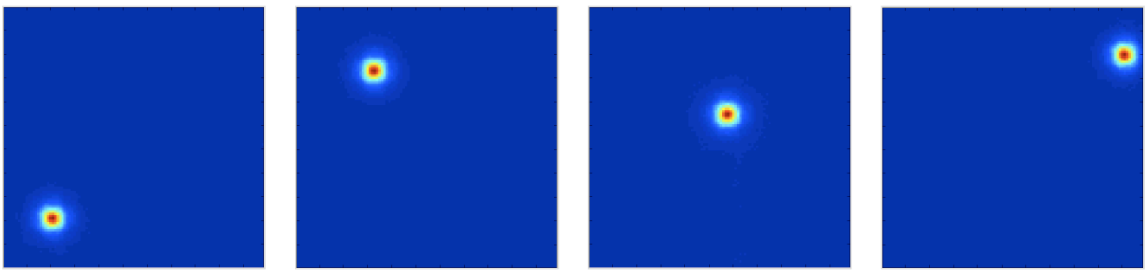

Figure 2.2: *Top view of four influence functions for a 1024-actuator MEMS DM.*

For MEMS DMs, the influence function can be modelled as a bi-dimensional Gaussian function[1], which is mathematically defined by

$$f(x,y) = \frac{1}{2\pi\sigma} exp \frac{-[(x-\mu_x)^2 + (y-\mu_y)^2]}{2\sigma^2} \tag{2.1}$$

The width of the actuator influence function is usually defined by the value of the σ. The influence function σ will vary for different DM technologies. This is an important parameter in the modelling of continuous membrane DMs. The IF takes into account the physical properties of the DM, because the function's width reflects the amount of mechanical coupling that exists between two adjacent actuators.

DM properties:

The bandwidth defines the temporal frequency, at which the DM can follow the wavefront evolution. The flattest surface obtained with a DM is called "best flat". Surface quality and operating temperature are also two important properties to be considered when selecting a DM for a given application.

The development of deformable mirrors has been a task undertaken by several research groups and private companies around the world. Several companies, such as Boston Micromachines Corporation (BMC), ALPAO, CILAS, Xinetics and IRIS AO, sell off-the-shelf deformable mirrors. Several technologies are used to generate the actuator motion and one can choose between electrostatic DMs, magnetic DMs, piezo-stack DMs, or bimorph DMs.

The DM characterization is an important step towards the optimized design of any AO system, because it provides critical information about the DM performance and how the other AO sub-systems will be affected. It is also critical for the proper modelling of DMs.

[1]Many other DM technologies cannot be modelled with a Gaussian function but instead are more like the difference between two gaussians or even a sine cardinal (sinc) function.

To gain thorough knowledge of DM characterization procedures and get familiar with DM technologies, in addition to MEMS, a preliminary step in this research work has been dedicated to the characterization of a magnetic DM (ALPAO) and a piezo-stack DM (CILAS). Both characterization results are presented in Appendix. A.

2.1 Critical DM parameters for AO system design

The DM parameters affect the overall system design, as well as the overall system performance. Having more actuators allows for a better fit to the wavefront and, therefore, the high order/high spatial frequency modes (Appendix B) will be more accurately compensated for. The benefit of increasing the number of actuators across the pupil to fit a phase shape is illustrated in Fig. 2.3.

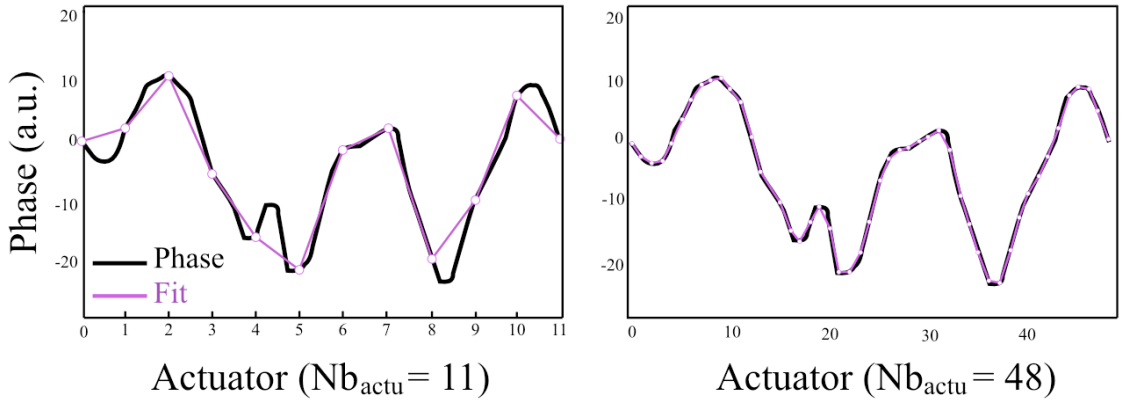

Figure 2.3: *Fitting a phase shape. Left, 11 actuators across the pupil. Right, 48 actuators across the pupil.*

A higher number of actuators implies a higher number of WFS measurements and, therefore, smaller sub-apertures, each receiving a smaller amount of photons. As a result, the increased number of WFS elements (necessary to take full advantage of a high actuator count DM) increases the measurement noise per WFS element (each receiving fewer photons). An increase in actuator density will also increase the computational cost. More actuators need to be controlled, more sub-apertures need to be processed and more demanding reconstruction algorithms are needed to retrieve the phase information. This increase in computational cost will most likely also impact

the correction frequency of the system.

Usually, the number of actuators will ultimately be defined by the turbulence characteristics of a given observing site. In general, a DM will be selected such that it provides approximately one actuator per r_0. Of course, the r_0 varies slightly over nights and years, which emphasizes the importance of the site and turbulence studies during the preliminary design of any astronomical observatory.

To properly correct the turbulence, defined by a given r_0, and provide the best fit to the wavefront, the telescope primary mirror of diameter D must be divided into sub-apertures of diameter $\simeq r_0$ (with r_0 evaluated at the observing wavelength). As a result, the necessary number of sub-apertures corresponding to the number of actuators N_{act} on the DM can be estimated as,

$$N_{act} = \left(\frac{D}{r_0}\right)^2 \tag{2.2}$$

MEMS DMs are available in a 144-actuator (12 by 12 grid) version and a 1024-actuator (32 by 32 grid) version. A 4096-actuator DM (64 by 64 grid) has also been implemented on GPI, although, GPI is actually using only a 44-actuator-diameter piece of their DM[50].

From Eq. 2.2, with a 8.2 meter telescope operating in the near-infrared ($\lambda = 2.5$ μm) with a r_0 of 138 cm, N_{act} is equal to 36 actuators. For the same telescope operating in the visible ($\lambda = 0.5$ μm) with a r_0 of 20 cm, N_{act} becomes 1681. This quick computation shows that state-of-the-art MEMS DMs equipped with up to 4000 actuators[23] exceed the requirements for future visible astronomical AO applications.

2.2 MEMS deformable mirrors

In the past decade, extensive studies have confirmed the potential of MEMS DMs for astronomical AO applications[64, 12, 49, 61, 13, 25, 62]. The astronomy community's interest in MEMS technologies has increased and resulted in the development of several advanced instruments employing MEMS DMs. For example, for direct detection and imaging of exoplanets, many of the HCI instruments under development employ MEMS DM to achieve their high contrast goals[39, 48, 10, 40] .

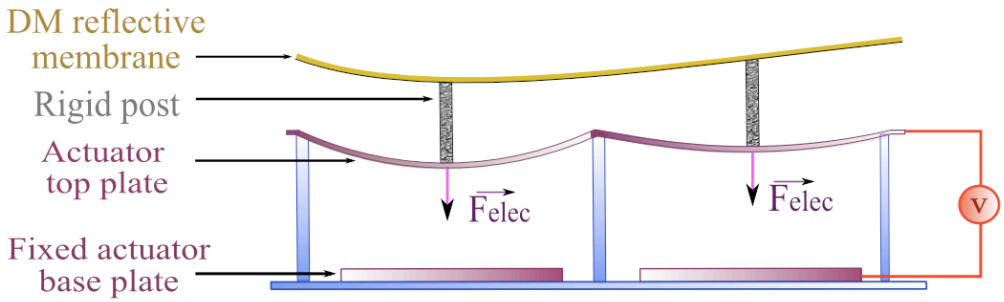

Figure 2.4: *Essential construction features of a MEMS DM.*

MEMS DMs[12] condense individual micro actuators into arrays capable of creating precise microscopic displacements. As illustrated in Fig. 2.4, MEMS DMs are composed of a thin silicon membrane with a highly reflective metallic coating, supported by an array of electrostatic micro-actuators. The vertical motion of each actuator occurs when a positive voltage is applied to the actuator top plate while the base plate stays grounded. The potential between the two plates induces an electrostatic attraction force between the two plates. While the base plate is fixed, the actuator top plate gets deflected towards the base plate by a displacement approximately proportional to the square of the applied voltage. Each actuator top plate is attached to the membrane through a rigid post, resulting in the local deformation of the membrane.

The various studies conducted with MEMS DMs have revealed many of this technology's advantages: sub-nanometre repeatability, high stability, negligible hysteresis (below 5%), low weight, compact size, high speed, and large number of actuators with a proportionately large stroke[11].

Compared with other DM technologies that exhibit bi-directional actuator motion, MEMS DM actuators can only be pulled in one direction. However, each actuator has low inertia and, therefore, it can be positioned along its total stroke with great accuracy and at high frequency (e.g in the kHz range).

The research work presented in this dissertation has been undertaken using two 1024-actuator MEMS DMs (Boston Micromachines Corporation, Fig. 2.5). The first

DM is located at the UVic AO Lab and the second DM is located at the Subaru Telescope, both have a continuous membrane. The DMs specifications may vary from one DM to another, but average values are gathered in Tab. 2.1.

Property	Notation	Value
number of actuators	Nb_{actu}	1024
actuator pitch	p	340 μm
actuator array size	–	12.4 mm
maximum voltage	V_{max}	250 V
actuator maximum stroke	S_{max}	1.5 μm
actuator influence function width	IF	
stroke-voltage relationship	–	quadratic
hysteresis	–	negligible
repeatability	–	$\leq$0.4 nm [26]
stability	–	0.13 nm rms [25]
wavefront error (unpowered)	–	50-150 nm rms [25]
wavefront error (after flattening)	–	$\leq$1 nm rms [25]
operating temperature	–	room temperature
bandwidth	–	$\sim$kHz

Table 2.1: *1024-actuator MEMS DM properties overview.*

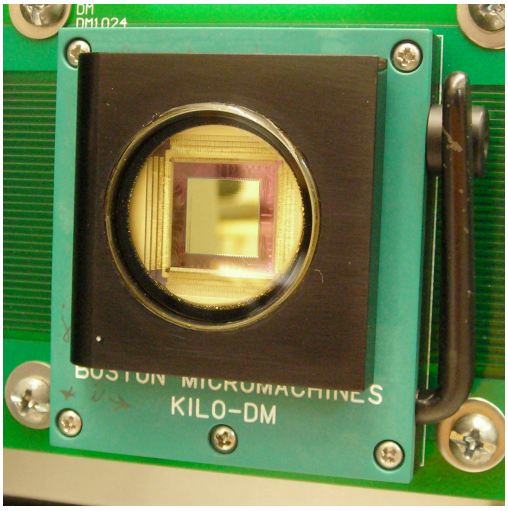

Figure 2.5: *A 1024-actuator MEMS DM on its custom electronic mount.*

Both DM membranes are coated with a thin layer of Cr-Au (chrome-gold alloy)

optimized for infrared wavelength. The UVic DM array contained defective actuators, most of which were located close to the pupil's edge, only one was located close to the centre of the array. This actuator did not respond properly to the applied voltage command. However, when the same voltage was sent to the whole array, the defective actuator followed the array's motion. This was true up to approximately 90 volts (V), after which the actuator displacement was limited.

2.3 Overview of DM modelling methodologies

The accurate open-loop control of DMs relies on the development of an accurate model, specifically designed to represent a given deformable mirror.

A DM possessing a linear relationship between actuator stroke and applied voltage, implemented on closed-loop AO systems, can be described by,

$$S(i) \; = \; a \; . \; V(i) \tag{2.3}$$

where $S(i)$ is the stroke obtained for the actuator i, a is a scaling coefficient, and $V(i)$ is the voltage applied.

Eq. 2.3 assumes there is no mechanical coupling between neighbouring actuators. The shape of the membrane is defined by the position of each actuator.

This model is appropriate for piezostack and magnetic DMs as they have a linear response.

As illustrated in Fig. 2.6, MEMS DMs have a non-linear quadratic relationship between the actuator stroke and the voltage applied,

$$S(i) \; = \; a \; . \; V(i)^2 \tag{2.4}$$

The plot shown in Fig. 2.6 was obtained with a 1024-actuator MEMS DM. The DM was mounted in front of a Zygo interferometer. A single actuator was driven from 0 volt to 200 volts in steps of 5 volts and the shape of the membrane was recorded.

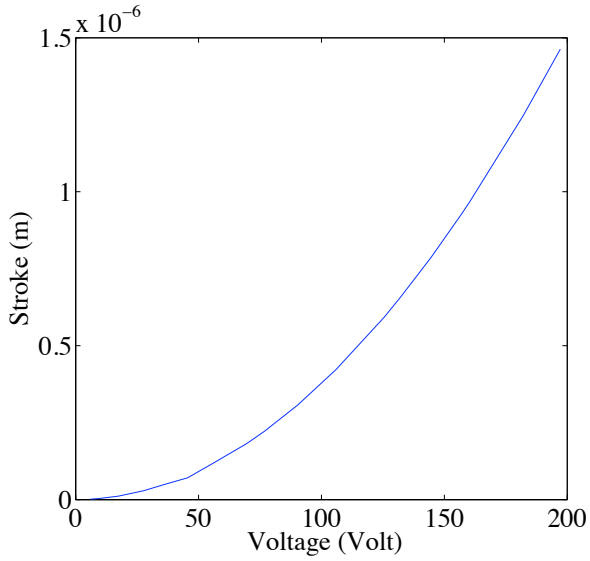

Figure 2.6: *Quadratic relationship between the voltage applied to the actuator and the resulting stroke for a 1024-actuator MEMS DM.*

The models represented by Eq. 2.3 and 2.4 are only valid to the first order, because some critical properties (physical and mechanical) of the DM are not accurately represented, for example, both assume all actuators are independent. However, with continuous membrane DMs, the membrane creates a mechanical coupling between neighbour actuators and, therefore, the vertical position of each actuators is actually impacted by the vertical position of its neighbour actuators. This dependency between neighbouring actuators is not correctly accounted for by either of the models.

Non-linear effects (for example, the actuator mechanical coupling or the actuator hysteresis, which is not negligible for piezo-stack DMs) result in poor performance of the model. For a given *desired* shape, the voltages provided by the model to drive the DM will result in a DM shape that differs from the desired shape. As a result, these simple models can only be used with the systematic adjustment provided by the feedback of a closed-loop architecture; open-loop architectures necessitate the development of more advanced models.

Typically, the DM performance is measured using an interferometer that provides membrane height (commonly measured in μm or nm) at each sample location. A common metric used to quantify the performance is the root-mean-square error (SE_{rms}) between the *desired* shape, D_i, and the *measured* membrane shape, M_i,

$$SE_{rms} = \sqrt{\frac{\sum_{i=1}^{N_{px}} (M_i - D_i)^2}{N_{px}}} \tag{2.5}$$

where N_{px} is the total number of interferometer samples, M_i is the measured membrane height at each sample location and D_i is the desired membrane height at each sample location.

2.4 Overview of advanced DM modelling methodologies

The development of advanced deformable mirror models (especially for open-loop control architectures) has been an on-going research topic for more than a decade.

Hom et al [47] (1999) presented a non-linear model for an electrostatic DM and obtained approximately 40 nm rms error when correcting for a given wavefront.

Vogel et al [74](2006) developed a MEMS DM model relying on a coupled system of (i) non-linear partial differential equations (to model the membrane flexure) and (ii) algebraic equations (dedicated to model the array of actuators underlying the membrane).

Morzinski [62] and Stewart [69](2007) reported less than 15 nm rms error on MEMS DMs for initial phase screens of 500 nm PV and 1500 nm PV, respectively. In [62], a 1024-actuator MEMS DM was used and the shapes applied correspond to (i) sinusoid functions, (ii) Gaussian functions (similar to an actuator influence function), and (iii) Kolmogorov functions. In [69], the performance evaluation was done by applying (i) influence functions and (ii) focus term (Zernike polynomial, Appendix B) to a 140-actuator MEMS DM.

Both Andersen [5] and Laag [3](2008) reported 10 to 20 nm rms error on an ALPAO DM.

Vogel et al [73](2010) proposed a refined variant of the 2006 method and applied it to both a 140-actuator MEMS DM and a 57-actuator piezo-stack CILAS DM. In this work, several array configurations were studied: (i) similar bias applied to all actuators, (ii) central actuator set to various voltage while the rest of the actuators are maintained at a mid-bias voltage, and (iii) central array of three by three actuators set to various voltages while the rest of the actuators are maintained at a mid-bias voltage, which resulted in less than 10 nm error for a Peak-to-Valley (PV) difference in deflection across the DM for a total deflection of approximately 500 nm.

The works presented in [73, 62, 69] used different variations of the thin plate equation. A detailed comparison of the three methods is given in the "Introduction" section of Vogel et al, 2010.

Guzmán [46](2010) reported 12.7% rms residual error (relating the residual error rms to the rms value of the desired wavefront) and 3.1% (relating the residual error rms to PV excursion of the desired wavefront correction) over several thousand phase screens of random shapes for a 14 by 9 active array of a 1024-actuator MEMS DM [46]. Guzmán's model is based on non-parametric estimation techniques [45]. The model, purely mathematical, needs a preliminary training step using a large (a few thousand) data set of interferometric phase maps and presents the benefit of a similar model strategy, regardless of the type of mirror in operation.

In the context of SCExAO, the above DM models are not suitable, because they suffer from computational complexity (they would not meet the instrument bandwidth requirement) and high wavefront error (SCExAO requires less than 10 nm rms). In order to overcome these limitations, two new modelling approaches were investigated. The first model, *Mod1* is an experimentally based approach and is described in Chap. 3. The second model, *Mod2* is a semi-physics/semi-empiric approach, and is described in Chap. 4. The intent of each model was to develop a method with reduced computational complexity and based on characterizing the physical properties of MEMS DMs.

2.5 Integration of a MEMS DM with an open-loop AO system

All classical SCAO systems currently implemented on astronomical instruments employ a closed-loop architecture, as illustrated in Fig. 2.7(a). However, recently proposed specialized AO systems require an open-loop architecture (Fig. 2.7(b)).

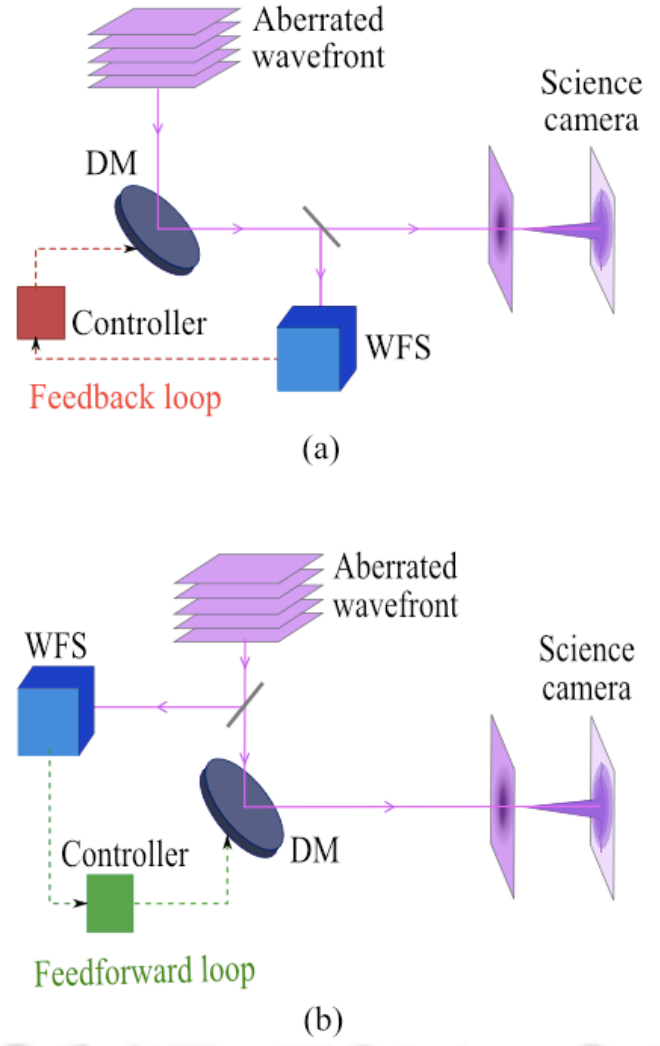

Figure 2.7: *Comparative schematics of (a) a closed-loop architecture and (b) an open-loop architecture.*

2.5.1 Closed-loop architecture

In a closed-loop system, the incoming aberrated wavefront first hits the deformable mirror. The beam is then sent toward a beam splitter that directs one portion of the beam toward the wavefront sensor and one portion of the beam toward the science camera. The wavefront sensor analyses the wavefront aberration and sends this information to the control system which computes the voltages to send to the DM to compensate for the aberrations.

With the wavefront sensor located downstream of the DM, the control system is able to take into account the feedback information regarding the DM shape in order to adjust the voltage commands sent to the DM.

The feedback in the control system presents many advantages:

- The residual wavefront error is significantly reduced
- The system is constantly updating the control commands in order to minimize the error. As a result, closed-loop control is less sensitive to non-linearities such as DM hysteresis
- Because the light first hits the DM, the turbulent signal seen by the WFS is a highly tamed version of the full turbulence. Indeed, after the first iteration, most of the high dynamic/low spatial frequencies (Appendix B) of the incoming phase have been compensated for. When the system performs well, the residual phase is left with only small errors of small dynamic range and high spacial frequencies. As a result, the dynamical range for the WFS can be relaxed. This is an important fact, because designing large dynamical range WFSs remains a challenging task.

2.5.2 Open-loop architecture

In an open-loop system, the WFS is located ahead of the DM and, therefore, operates without the knowledge of the current DM state. Without this feedback information, the WFS can not see the impact of the control system action on the DM shape.

The challenges inherent in implementing an open-loop system are:

- The WFS dynamic range must be much higher

- The static NCPAs must be measured and integrated to the controller so they can be subtracted from the dynamical aberrations each time a set of commands is sent to the DM

- The DM becomes a problematic element, because the DM is now controlled independently from the wavefront sensor measurements. As a result, the control system (i) has no knowledge of the DM shape at any time and (ii) has no way to verify the system is not diverging. The first order model (Eq. 2.4) cannot be used and an alternative advanced model (usually dependent on a preliminary careful DM calibration) must be established to drive the DM accurately and ensure an optimum match between the desired shape and the measured shape.

2.6 AO systems employing open-loop architectures

New science goals and advanced AO technological requirements have driven the development of more complex AO architectures. Two examples are (i) the direct detection of exoplanets utilizing HCI instruments based on advanced ExAO and coronagraphic technologies and (ii) the efficient pursuit of science on ELTs utilizing Multi-Object Adaptive Optics (MOAO).

ExAO and MOAO[4, 24] are transformative AO technologies that are currently the focus of much research. In both cases, pathfinder instruments are under development.

For ExAO, SCExAO, GPI, and SPHERE will soon be implemented on three 10-meter class telescopes (Subaru, Gemini and VLT, respectively).

RAVEN[22, 6], a MOAO demonstrator developed for the Subaru Telescope, is being assembled at the University of Victoria. CANARY, a demonstrator for EAGLE[67], has already gone through several successful on-sky runs at the 4.2-meter William Herschel Telescope. Classical SCAO systems are inefficient for the observation and spectroscopic analysis of faint galaxies, because (i) the small number of photons received necessitate very long exposure time (several hours) for each target and (ii) the distribution of galaxies in space is sparse. Performing large statistical surveys of galaxies is the next logical step toward learning more about galaxy formation and

evolution, but such surveys cannot be achieved using SCAO, because the required number of observing nights would largely exceed the amount of observing time that a Time Allocation Committee (TAC) can provide to a given science project (telescope time is in high demand and an observing proposal must request a reasonable amount of nights to have a chance to be selected). MOAO coupled to Multi-Object Spectroscopy (MOS) techniques will allow the simultaneous spectroscopic analysis of up to 25 science fields of view (FoV) spread over a large field of regard (FoR) of several arcmins. Each science FoV is only a few arcsecs wide and contains one galaxy.

In MOAO systems, open-loop control of the DM is required, because the WFS data (gathered from a few guide stars, sparsely distributed within the wide FoR) is processed by a central tomographic reconstructor, which enables the narrow field correction around the different science targets. Such a tomographic approach requires the WFSs to be located upstream of the science path and, therefore, upstream of the DMs. This open-loop architecture necessitates the implementation of advanced DM modelling methodologies.

Note that adding an additional WFS in each science path downstream of the DM (thus providing a closed-loop configuration within each science path) would be a costly solution for systems designed with twenty or more science paths and would, in most cases, be useless because the FoV seen by each of these additional WFSs would not contain a suitable guide star to perform the wavefront sensing.

Chapter 3

MEMS DM modelling for open-loop control - An experimental-based approach

In order to evaluate the potential of MEMS deformable mirrors for open-loop applications, the actuator's stroke-voltage relationship and the effect of the non-additivity of the influence functions are studied and integrated in an open-loop control process. The characterization process was performed on a 1024-actuator MEMS DM. Such preliminary DM characterization is essential to obtain deterministic membrane deflection. This experiment is aimed at minimizing the residual error obtained in open-loop control.

3.1 Part I: Deformable mirror characterization

In addition to the immediate need for controlling SCExAO MEMS DM, open-loop control of MEMS DMs is becoming more critical in the prospective of new Extremely Large Telescopes (ELTs) and their respective science instruments.

With a continuous membrane creating a mechanical coupling between neighbouring actuators, the motion of a given actuator, originated by the voltage received, is also influenced by the indirect effect of the vertical position of the adjacent actuators.

Most of the research in this area focuses on the development of an accurate model[31, 62, 69, 74, 8]. In order to build such a model, one needs to quantify both (i) the non-linear relationship between the input voltage and the resulting actuator motion and (ii) the effect of the mechanical coupling between neighbouring actuators.

In the following sections, the result of a thorough DM characterization is presented. Sec. 3.1.1 describes the experimental setup used to perform the characterization, Sec. 3.1.2 is focused on the stroke-voltage relationship, and Sec. 3.1.3 describes the influence function's (IF) non-additivity. Finally, Sec. 3.1.4 presents the performance obtained when a DM characterization-based open-loop control approach is chosen to drive the MEMS DM.

3.1.1 Experimental setup

The experimental setup (Fig. 3.1) used to conduct this first series of DM characterization consists of a 1024-actuator MEMS DM positioned in front of a Zygo PTI 250 interferometer.

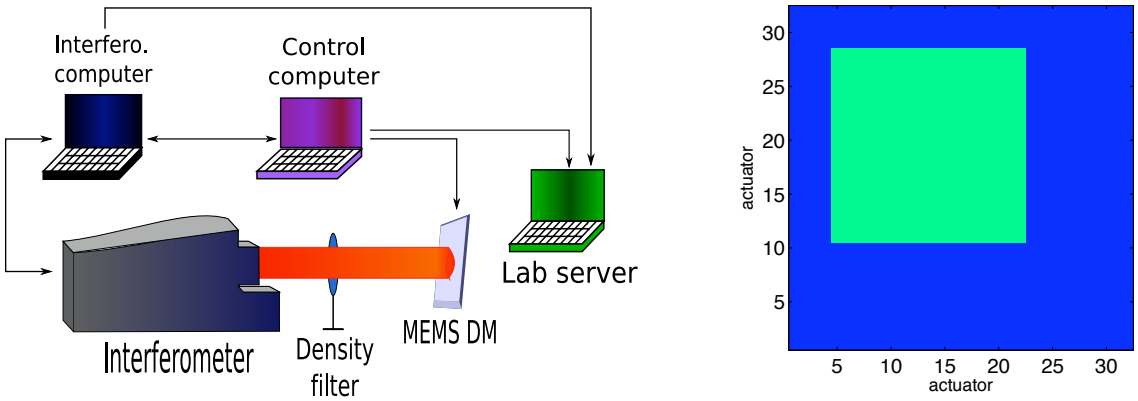

Figure 3.1: *Left, diagram of the experimental setup. Right, DM's active area (light green square). The interferometer mask is set to cover only the active area.*

The DM is driven by custom electronics with a maximum capacity of 150 volts (with 14 bit resolution). The interferometer beam passes through a density filter to improve the interference fringe contrast. A mask can be set on top of the interferometer beam using the software provided with the interferometer.

One computer is dedicated to the interferometer control software (metrology and control interface), while a second computer uses a combination of Matlab and C codes

to (i) control the DM electronics, (ii) remotely initiate the interferometer measurements, and (iii) transfer the recorded data to a data server.

Both the DM and the interferometer are set on an optical table isolated from the ground to minimise vibrations.

3.1.2 Calibration of the actuator stroke-voltage relationship

The actuator stroke-voltage relationship (SVR) is the relationship between the membrane deflection and the corresponding applied voltage. For MEMS DMs, the quadratic SVR for a given actuator i can be described as,

$$Stroke(i) = gain(i).\,V(i)^2 \;+\; offset(i) \tag{3.1}$$

where $V(i)$ is the voltage sent to the actuator i, $offset(i)$ is the actuator offset and $gain(i)$ is the actuator gain.

The precise calibration of each actuator's SVR is a critical step toward accurate open-loop control of the deformable mirror. For this experiment, due to a large number of malfunctioning actuators located on the right side of the actuator array, a reduced active area of 18 by 18 actuators (a total of 324 actuators) is selected. The position of this array with respect to the DM membrane is presented in Fig. 3.1, right image. The actuator situated at the bottom left corner of the active area is coupled with an actuator located outside the active area and has a reduced maximum stroke. This actuator can be seen in Fig. 3.2 (blue curve). With a maximum voltage output of 150 volts, the resulting maximum stroke obtained for each actuator is approximately 0.5 micron.

3.1.3 Characterization of influence function non-additivity

The actuator influence function is the characteristic shape of the mirror response to the action of a single actuator. To study the influence function non-additivity, several random pairs of neighbouring actuators within the active area are selected. This

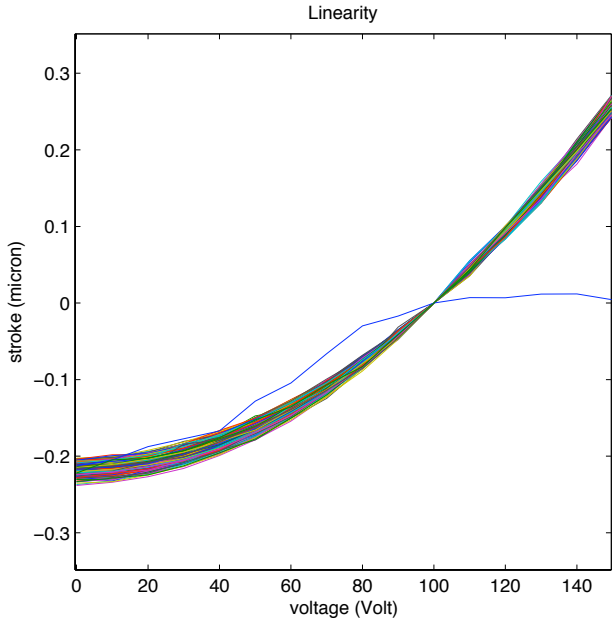

Figure 3.2: *Stroke-voltage relationship for the 324 actuators. All actuators present a maximum stroke of approximately 0.5 micron. The blue line corresponds to a defective actuator, which is coupled with an actuator located outside the active area.*

section presents the results obtained for the pair of actuators indexed 169 and 170, which are representative of the other actuators tested. Three tests were conducted to characterize non-additivity.

First, for each pair of actuators, the membrane was set to a bias voltage of 0 volt. The two actuators under test were first pushed sequentially to 50 volts, 100 volts, and 150 volts. Then, the two actuators were pushed simultaneously to these three voltages. This test was then repeated with a bias voltage of 150 volts, while the actuators are released sequentially, then simultaneously to 0 volt, 50 volts, and 100 volts. Similar tests were then repeated on several arrays of 3 by 3 actuators.

Finally, the last test focuses on the non-additivity effects when the pair of actuators are on a push-pull configuration (one pushed up, the other pulled down).

Fig. 3.3 shows the cross-sectional view of the influence function when each actuator is pushed sequentially (green and red plots) and simultaneously (light blue plot labelled *poke2*) to 100 volts with a bias voltage of 0 volt. The linear sum (obtained

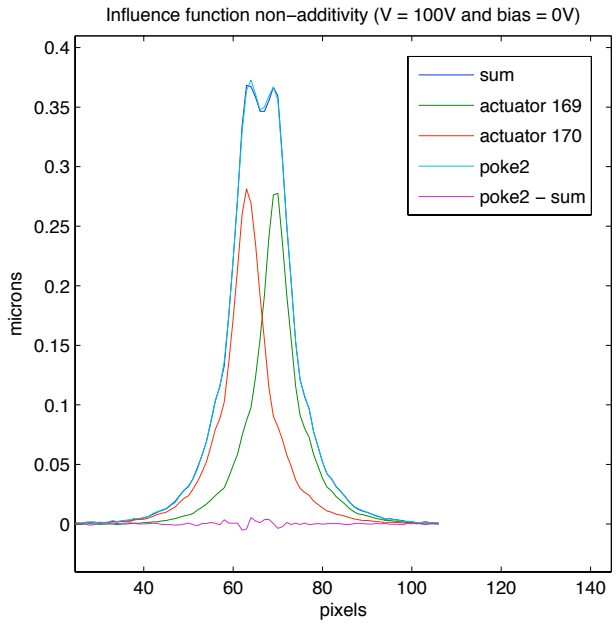

Figure 3.3: *Influence function non-additivity measurement for a pair of actuators (one actuator has 6 pixels across).*

numerically post-measurement) is also presented (dark blue plot, labelled *sum*), as well as the difference between the *poke2* and the linear *sum* (purple plot, labelled *poke2 - sum*). Note that there is no current satisfying explanation for the dip observed between the two adjacent actuators.

3.1.3.1 Pair of neighbouring actuators

The results obtained from the pair of neighbouring actuators indexed 169 and 170 are presented in Fig. 3.4 where the top plots correspond to a bias of 0 volt and the bottom plots correspond to a bias of 150 volts. For clarity, the plots showing the cross-sectional views of the influence function when the actuators are pushed sequentially are not displayed.

From here forward, the *relative voltage* will be defined as the difference between the bias voltage (applied to the whole DM) and the input voltage (only applied to the pair of neighbouring actuators under test). For example, for a bias voltage of 150 volts and an input voltage of 100 volts, the relative voltage is 50 volts. For a bias

voltage of 0 volt and an input voltage of 50 volts, the relative voltage is also 50 volts.

Fig. 3.4 reveals four remarkable non-linear behaviours.

- The strokes obtained with a 0 volt bias are much larger than the strokes obtained with a 150 volts bias for the entire range of input voltage values.

- The linear sum (labelled *sum*) always provides a smaller stroke than the pair of actuators poked simultaneously (labelled *poke2*), except for one particular case, when the bias voltage is 0 volt and the input voltage is 150 volts (purple and yellow plots on Fig. 3.4, top image).

- The difference in stroke between a relative voltage of 100 volts and a relative voltage of 150 volts varies from approximately 0.5 micron with a bias of 0 volt to less than 0.1 micron with a bias of 150 volts.

- Unlike previous models[74], where two actuators poked simultaneously present a resulting influence function peak shaped with a flat top, this experiment reveals the presence of a dip at the top of the peak.

To explain such behaviours, several factors need to be taken into account. First, at 0 volt bias (corresponding to the default membrane position), the membrane is relatively flat and undergoes no stretch. However, with a 150 volts bias, the membrane becomes slightly dome shaped and stretched, due to the fact that the membrane is clamped and the edge actuators have less available stroke than the actuators located closer to the centre. This additional stretch decreases the elasticity available for the pair of actuators under test, resulting in a smaller stroke. This elasticity saturation can also explain the difference in stroke between similar relative voltages (100 V and 150 V) for the 2 different biases (0 V and 150 V).

Another factor that contributes to this difference relies on the stroke-voltage relationship of each actuator. Fig. 3.2 presents the typical quadratic relationship between stroke and voltage. At the beginning, the stroke increase is much slower than the voltage increase. After a midpoint, located around 100 volts for this apparatus, the stroke increase is much faster and follows the voltage increase in a near linear fashion.

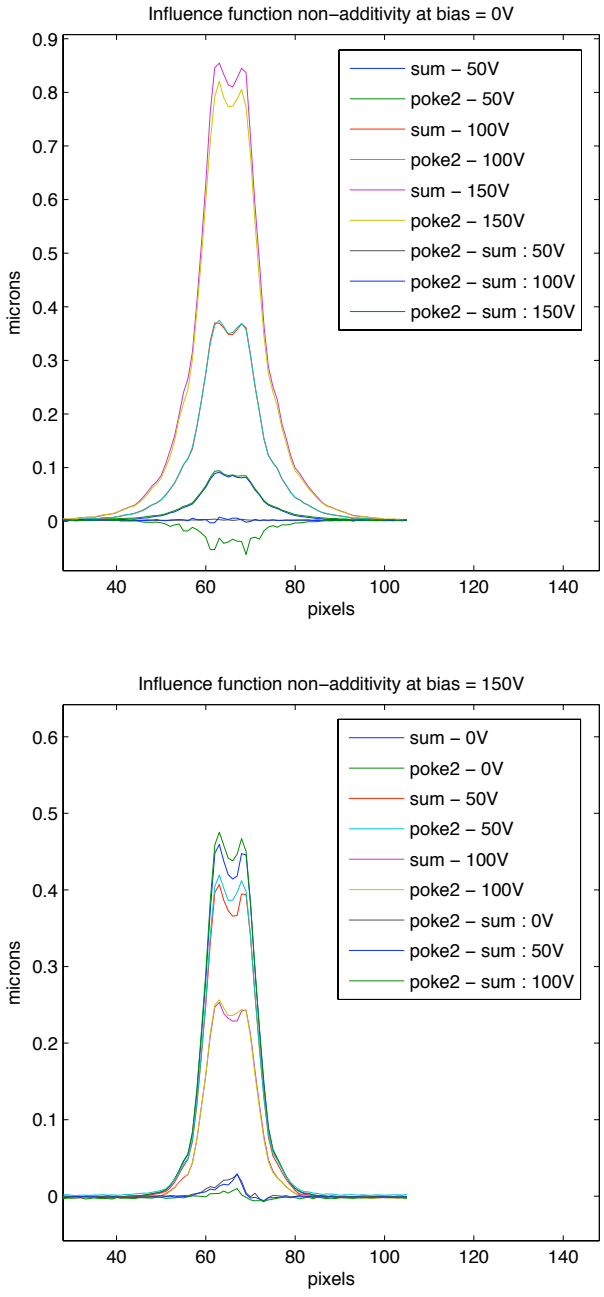

Figure 3.4: *Non-additivity of influence function measurement for a pair of actuators with a bias of 0 volt (top plots) and a bias of 150 volts (bottom plots).*

A relative voltage of 50 volts in the 0 volt bias configuration corresponds to a slow stroke increase, thus providing a small stroke. This same relative voltage in the 150 volts bias configuration corresponds to a point further up the curve, providing a larger stroke.

3.1.3.2 Array of 3 by 3

The tests performed on a pair of adjacent actuators were repeated with several arrays of 3 by 3 actuators. A representative array is selected to illustrate the results. Fig. 3.5 (top), presents the comparison between the 3 by 3 actuators, which are first pushed together (labelled *poke3*), then pushed sequentially and added numerically (labelled *sum*) at relative voltages of 50 volts, 100 volts and 150 volts. Fig. 3.5 (bottom), presents these results when the bias is 150 volts.

At 0 volt bias, the linear sum always provides a larger stroke than pushing the actuators simultaneously. However, at 150 volts bias, the opposite effect occurs and the *poke3* is always larger than the linear *sum*. Indeed, an array of 3 by 3 actuators pushed together has a much larger strength than each actuator pushed independently. Thus, when the membrane elasticity is reduced due to stretching, the *poke3* gives larger stroke than the linear sum.

The stretching effect is also responsible for the large variation between the stroke obtained for a *relative voltage* of 150 volts at 0 volt bias (approximately 1.4 microns) and at 150 volts bias (approximately 0.9 micron).

Finally, at 0 volt bias, the influence function presents a much larger profile than the one obtained at 150 volts bias.

3.1.3.3 Push-pull

In a push-pull configuration, the pair of actuators are pushed in opposite directions. As opposed to other DM technologies, where the actuation is bi-dimensional, up or down (such as piezo-stack DM), the MEMS DM presents a characteristic pull-in behaviour. In order to set the actuators in a push-pull configuration, we added a bias

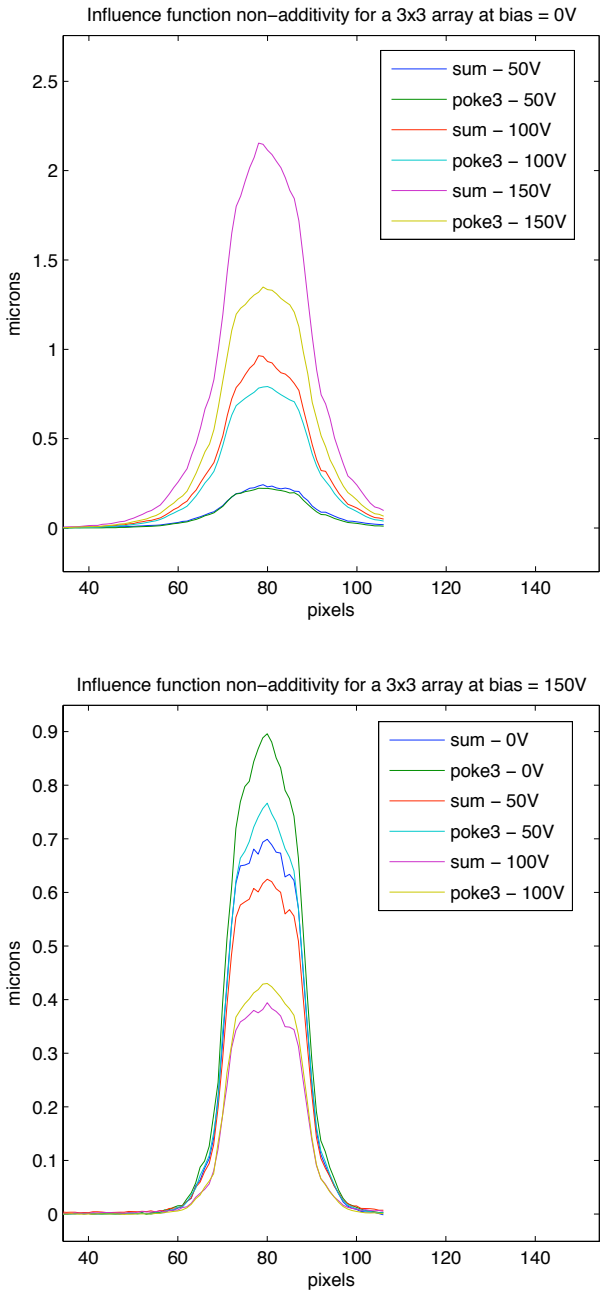

Figure 3.5: *Non-additivity of influence function measurement for an array of 3 by 3 actuators with, top, a bias of 0 volt and bottom, a bias of 150 volts.*

of 100 volts, then set the actuator indexed 169 to 77 volts and the actuator indexed 170 to 118 volts. This provides a peak to valley stroke of 0.2 micron. This stroke is kept relatively small to limit the stress undergone by the membrane and to avoid damage.

Fig. 3.6 shows that the non-additivity of influence functions is compensated when the actuators are in the push-pull configuration (plots *sum* and *poke2* are on top of each other). This is an encouraging result, since the actuators' configuration when the DM is set to compensate for atmosphere turbulence is close to a push-pull.

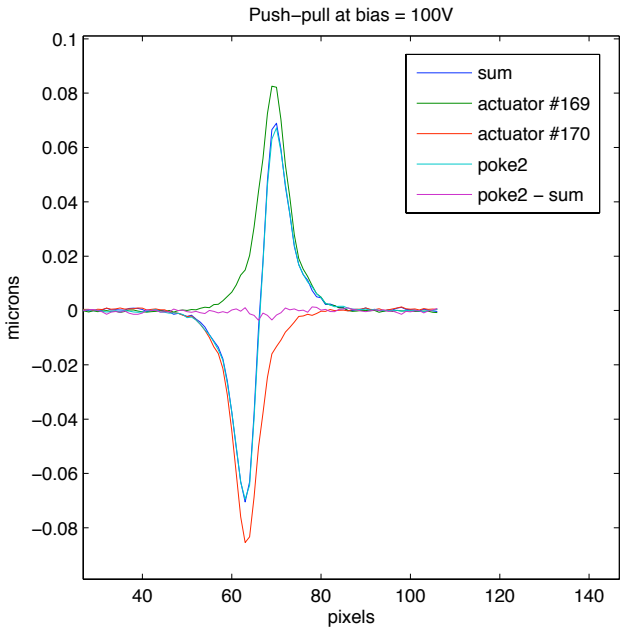

Figure 3.6: *Push-pull measurements.*

3.1.4 Open-loop control performance

From the results presented in the previous sections emerged a new research path: what accuracy can be reached (best residual rms) using an experimentally based open-loop control strategy? Indeed, with a thorough characterization process, the control commands (volt maps) can be computed by using the information obtained from both the actuator stroke-voltage relationship and the actuator influence function.

The performance for open-loop control of the MEMS DM is investigated for a simplistic approach (described in detail in Sec. 3.2), using only the calibration of the actuator's stroke-voltage relationship (Eq. 3.1) and the calibration of the actuator's influence function.

The main difference between this approach and the traditional matrix-based control approach is that the matrix-based control is done by measuring a poke matrix. Once this matrix is inverted, it becomes the command matrix, which provides the link between the wavefront sensor slopes measurements and the voltages to be send to the DM. In the approach proposed below, the voltage commands to apply to the DM are obtained without using the wavefront sensor slope measurements or a command matrix. Instead, the voltage commands are deduced from the characterisation of the actuators influence function and the characterisation of the actuators stroke-voltage relationship.

One hundred computer-generated phase screens are simulated. The phase screen properties are representative of atmospheric turbulence as seen by a 30-meter telescope (with $r_0 = 15$ cm, $L_0 = 60$ m) and must be scaled down to match the DM's maximum stroke (approximately 0.5 μm).

The open-loop control process is as follows:

- The least squared fit of the phase screens projected onto the normalised influence functions provides the actuator stroke maps. This least squared fit is similar to the one perform in the matrix-based control approach, a detailed description will be given in Sec. 3.2.2.2.

- The *gain* and *offset* coefficients introduced in Eq. 3.1 can be extracted from the stroke-voltage characterization. Fig. 3.7 illustrates the linear relationship between the stroke and the *squared* voltage.

- The volt maps to be sent to the DM are deduced from the stroke maps by reversing Eq. 3.1.

The multiplication of the stroke maps by the normalised influence functions provides the fitted phase screens. The fitting error is the result of the difference between

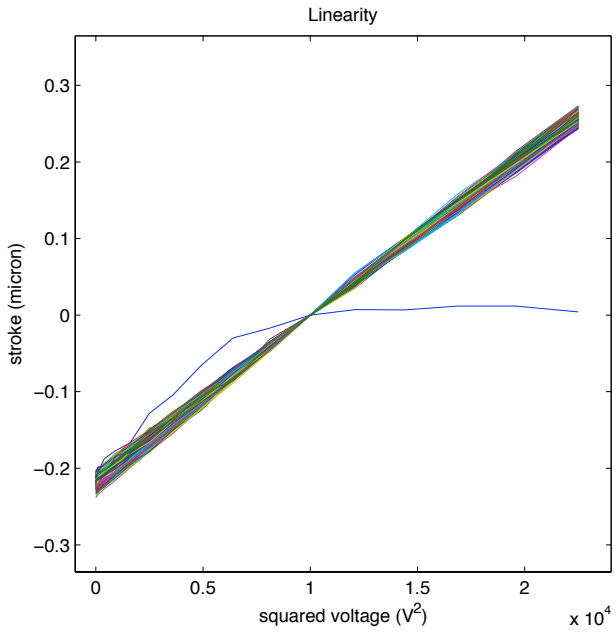

Figure 3.7: *Stroke-voltage relationship for 324 actuators of the array. The stroke is represented as a function of the squared voltage.*

the original phase screens and the fitted phase screens. The fitting error corresponds to the DM sampling error, due to the limited number of actuators.

One set of data is shown in Fig. 3.8, to illustrate the results obtained with this basic open-loop control process. Fig. 3.9 presents the rms of the fitting error and the rms of the measurement error (or open-loop error) as a function of the rms of the generated phase screen for the 100 phase screens used to perform the open-loop control tests.

The mean open-loop rms for the measured membrane deflection is 11 nm. This result suggests:

- a preliminary characterization of the stroke/voltage relationship is sufficient to achieve good control

- the non-additivity of actuators' influence functions can be assumed to be negligible for a MEMS DM provided (i) the DM is used in an open-loop scheme to compensate for Kolmogorov type phase screens and (ii) the maximum actuator strokes are kept relatively small.

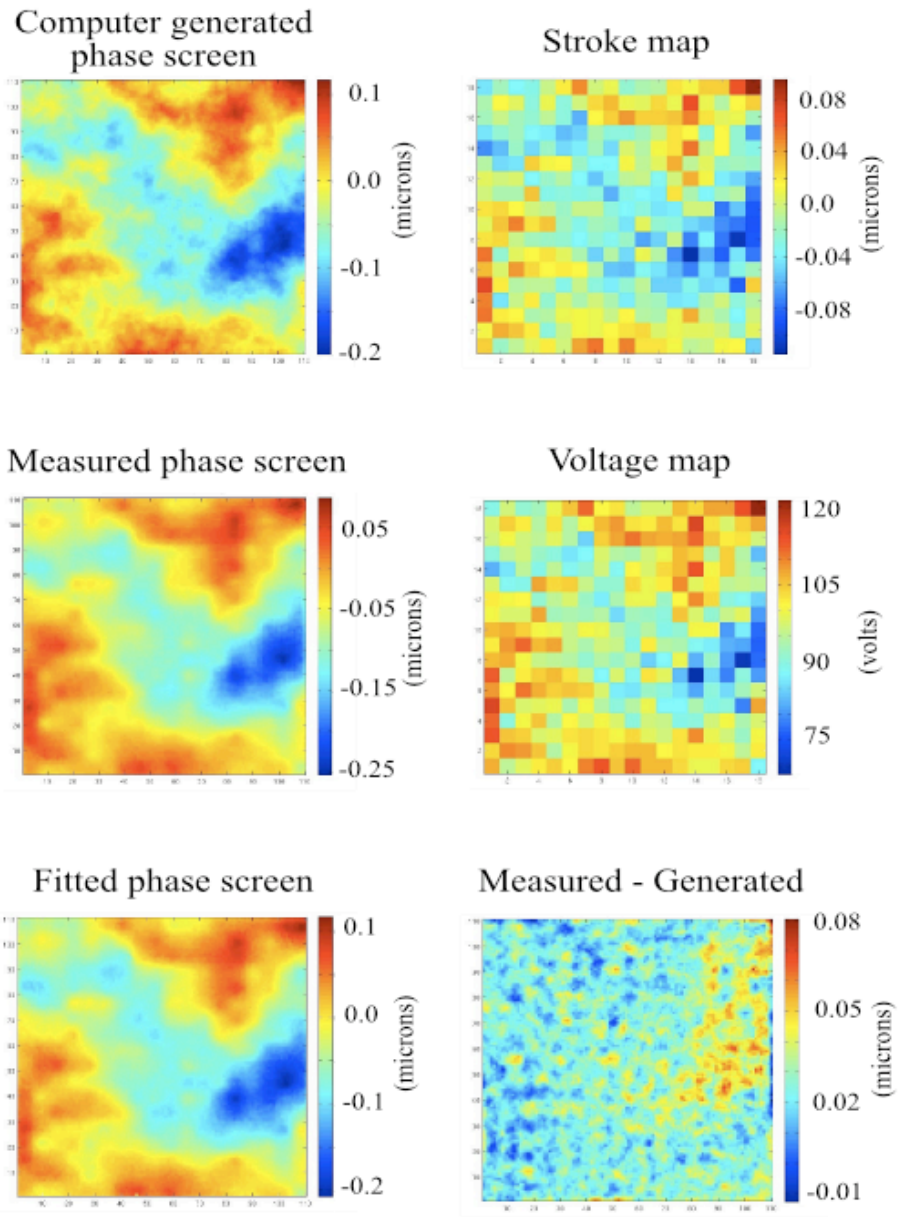

Figure 3.8: *Illustration of open-loop control results for a set of data from the 100 samples.*

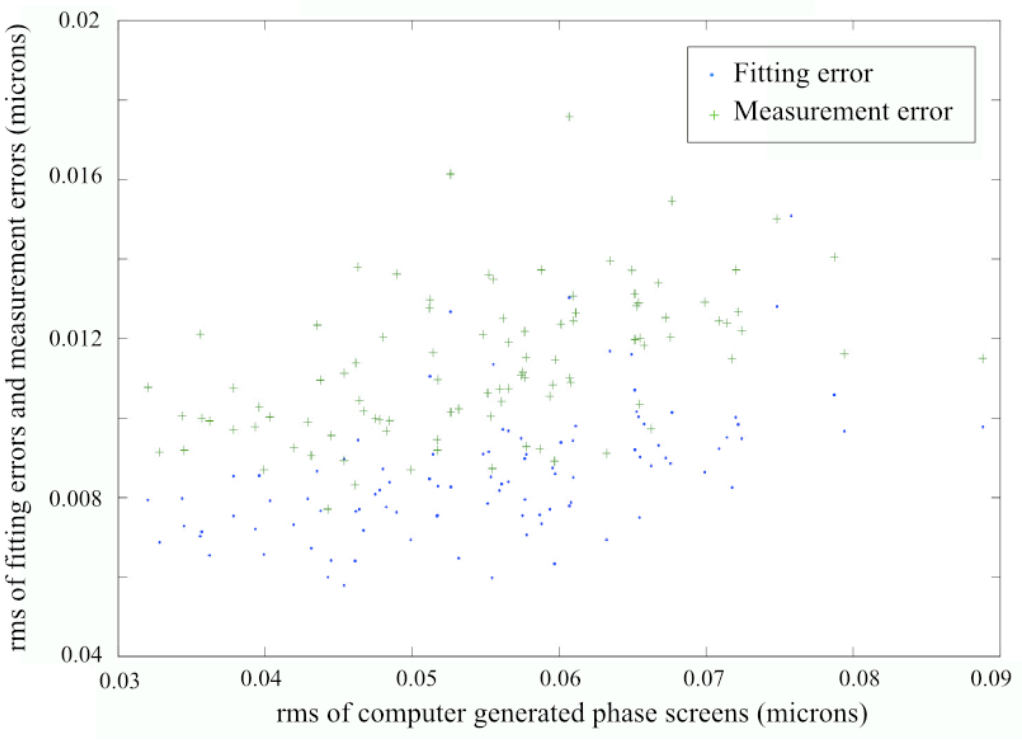

Figure 3.9: *Open-loop (measurement) error rms and fitting error rms versus the generated phase screen rms for the 100 test phase screens.*

3.1.5 Conclusion for Part I

The influence functions non-additivity has been linked to the combination of elasticity loss (due to membrane stretching) and to the actuator's quadratic stroke-voltage relationship. It has been shown that these IF non-additive effects are negligible in a push-pull configuration. As a result, the IF non-additivity can be neglected when a random shape (such as a Kolmogorov turbulent phase screen) at relatively low voltage is applied to the DM. With this assumption, a simple open-loop approach based on the actuators' properties characterization has been tested and showed encouraging results.

3.2 Part II: Model (*Mod1*)

The work presented in the following sections is based on the following assumptions:
• for a typical turbulent phase screen, there is more power at low spatial frequencies than at high spatial frequencies
• the statistical distribution of actuators compensating for a phase screen type Kolmogorov is such that the number of actuators on the "up" position is roughly equal to the number of actuators on the "down" position. Thus, under such conditions, the non-additivity of the influence functions can be considered negligible.

The experimental setup is identical to the setup described in Sec. 3.1.1 (Fig. 3.1), except for the electronics driving the DM that have been updated in order to increase the maximum stroke available. The highest voltage that can be sent to the DM is determined by (i) the DM physical limit (i.e., the size of the actuator gap) and (ii) the electronics. The DM physical limit is 250 volts. If an actuator is exposed to a higher voltage, the electrostatic force generated between the actuator plate and the actuator base will bring the actuator plate all the way down to the actuator base. The upgraded electronics used for this experiment can provide a maximum voltage of 200 volts, which according to the manufacturer, should provide a maximum stroke of 2.5 μm.

The active area on the DM is still a square of 18 by 18 actuators. However, aligning the pupil edges (i.e., the edges of the interferometer mask) to half of the edge actuators reduces the fitting error (this result will be detailed in Sec. 3.2.2.3). In this optimized configuration, the effective area of the DM becomes a square of 17 by 17 actuators. For an optimized pupil size of 106 by 106 pixels, the spatial resolution of the interferometer is 6.2 pixels per actuator for a 17 by 17 actuator array. All results presented in the following sections are given in nm or μm *wavefront*, with 2 nm *wavefront* equals to 1 nm *surface*.

There are only two DM properties which need to be evaluated to complete the characterization process necessary for the control strategy: the actuator SVR and the actuator influence function.

Note, to ensure the reliability of the characterization data, a new set of data should

be taken, if the experimental setup is modified (optical re-alignement, temperature variation). This will guarantee up-to-date DM properties necessary to achieve an accurate control of the DM.

3.2.1 Deformable mirror characterization

3.2.1.1 Measurement of the actuator stroke-voltage relationship

The SVR plots for each actuator of the 18 by 18 array are generated by driving the actuator from 0 volt to 200 volts in steps of 20 volts, while the rest of the actuators are set to a voltage bias of 140 volts (this bias voltage corresponds to the mid-stroke, directly measured from an actuator's stroke-voltage plot).

The maximum stroke observed is approximately 800 nm. However, the coupled actuator in the bottom left corner (described in Sec. 3.1.2) has a limited maximum stroke of only 400 nm. The SVR plots obtained for the 324 actuators are presented on Fig. 3.10. The x-axis represents the squared voltage sent to the actuator and the y-axis the corresponding actuator stroke (in nm). The standard deviation of the measurements is 23.4 nm rms.

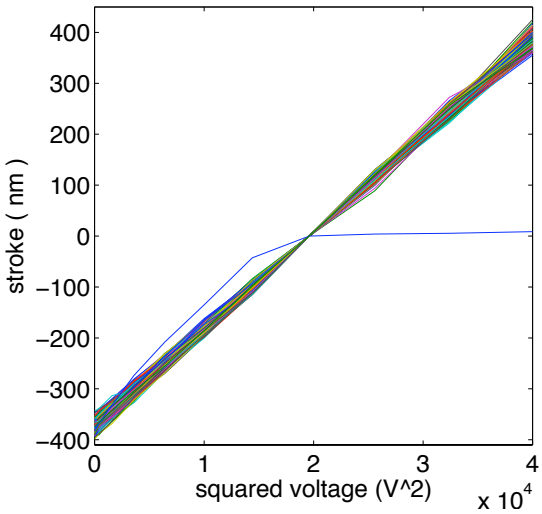

Figure 3.10: *Stroke-voltage relationship plots for the 324 actuators. The x-axis represents the squared voltages and the y-axis represents the stroke (in nm).*

3.2.1.2 Measurement of the actuator influence function

The influence functions are measured by releasing, one at a time, the actuators at 0 volt, while the rest of the membrane is pushed at the bias voltage of 140 volts. For each actuator, the phase is measured by the interferometer and normalised.

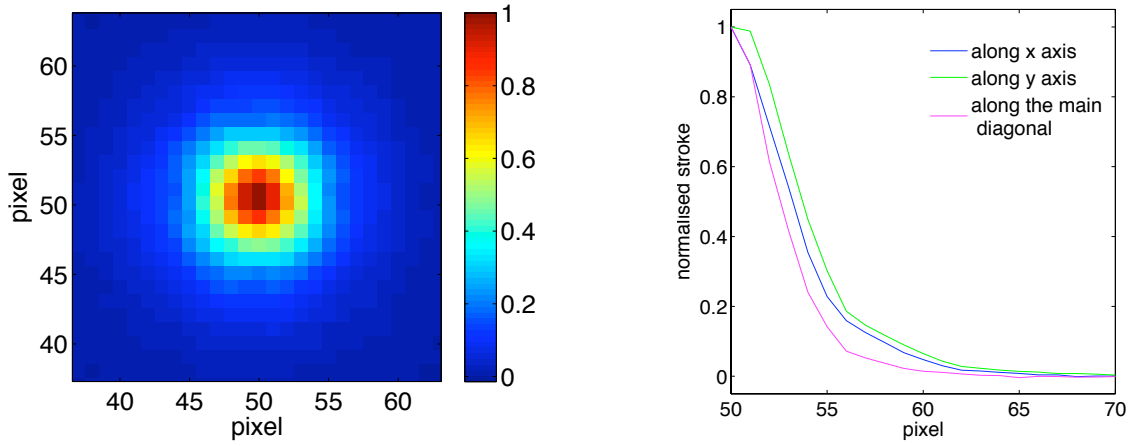

Figure 3.11: *Left, top view (zoomed) of the normalised influence function for actuator # 171. Right, cross-sectional views along the x- and y-axis, and along the diagonal (the actuator pitch is ∼6 pixels).*

To normalise the influence function, each measured phase map is divided by the absolute value of the maximum phase point in the phase map. The normalised influence functions are unitless phase maps with the scale ranging from zero to one.

The top-view of the normalised influence function for actuator # 171 is presented in Fig. 3.11, along with the cross-sectional view along the x-, y-, and diagonal axes. The slight asymmetry observed along the different axes is due to a pixelization effect.

Note, in view of the actuators being released one at a time, the influence function measurements do not include any non-linear information related to the mechanical coupling between neighbouring actuators.

3.2.2 Performance evaluation in open-loop control

This section describes the experimental protocol that was followed, starting from the generation of the 100 test phase screens to their final projection onto the DM. The 100 computer-generated phase screens previously used in the open-loop experiment described in Sec 3.1.4 are used again. However, because the DM electronics have been upgraded to provide up to 200 volts, the sample phase screens have been scaled down in a new way that match the new maximum stroke available on the DM.

The phase screen selected to illustrate the results in this section is similar to the one selected to illustrate the results in Sec 3.1.4. The images corresponding to the scaled-down phase screen, the projection onto the influence functions and the DM, as well as the matching volt map, are gathered in Fig. 3.12.

Fig. 3.13 illustrates the open-loop control process and Fig. 3.14 the various errors introduced in the following sections.

3.2.2.1 Generation of phase screens

One hundred phase screens φ are generated using Matlab. To create phase screens that match the dynamical range of the MEMS DM, the generated phase screens are first numerically rescaled. They are generated using turbulence parameters, which follow a Von Karman statistic. The Fried parameter, r_0, is set to 15 cm. The outer scale, L_0, is set to 60 m and corresponds to the size of the largest turbulence cell. Finally, the pupil diameter, D, is set to 30 m. The characterization of the actuator SVR presented in Sec. 3.2.1.1 shows the DM being tested has a maximum stroke of approximately 800 nm. With a bias voltage of 140 volts, the DM stroke varies from -400 nm to +400 nm. However, the scale of the raw phase screens generated through Matlab is around 15,000 nm. In order to avoid DM stroke saturation, the phase screens are scaled to 88% of the DM maximum stroke. The piston is also removed in order to match the phase screen dynamic range to the actuator dynamic range ($\pm 400nm$) with no bias voltage.

For the representative phase screen φ (Fig. 3.12), the phase varies approximately from 250 nm to -300 nm.

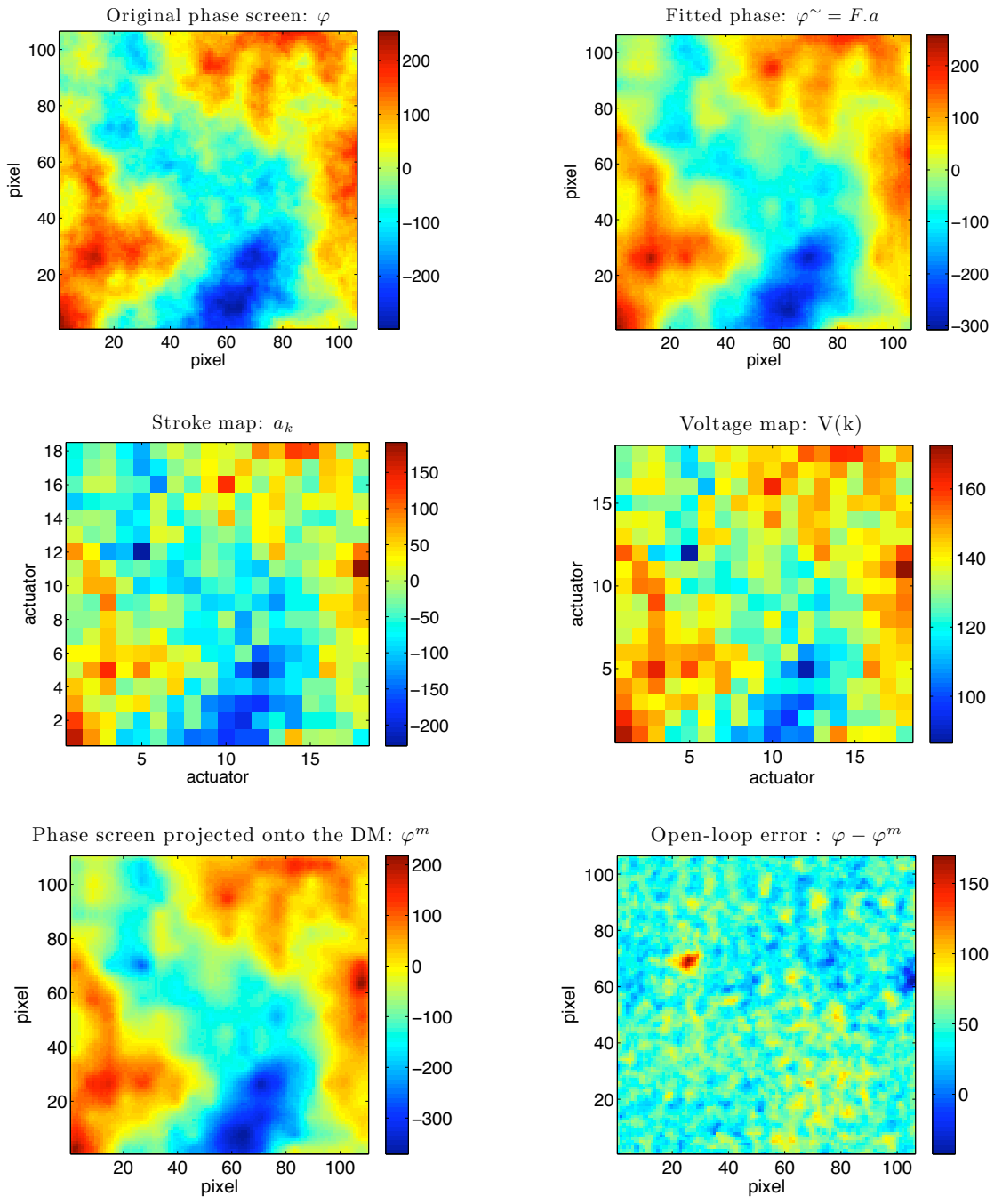

Figure 3.12: *Computer-generated, scaled-down phase screen φ, fitted phase $\tilde{\varphi}$, stroke map, volt map, projection of the original phase screen φ onto the DM and "open-loop" error. The error map incorporates both the fitting error and the DM error. All vertical scales are in nm, except for the volt map given in volts.*

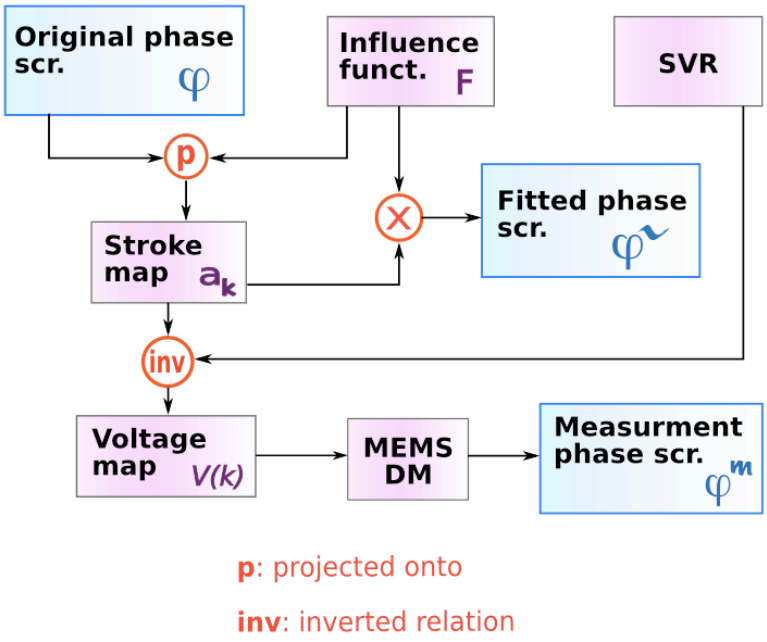

Figure 3.13: *Open-loop control process.*

3.2.2.2 Projection on influence function: stroke map computation

For a pixel of coordinates $(x,\ y)$, the phase for the MEMS DM at this pixel is given by:

$$\varphi(x,y) = \sum_{k=1}^{324} a_k \cdot F_k(x,y) \tag{3.2}$$

where a_k represents the unknown stroke coefficients and F_k represents the normalised influence functions, measured and described in Sec. 3.2.1.2 (one a_k coefficient per influence function and one influence function per actuator).

Using matrix representation, this relation can be re-written as,

$$\varphi = F \cdot\ a \tag{3.3}$$

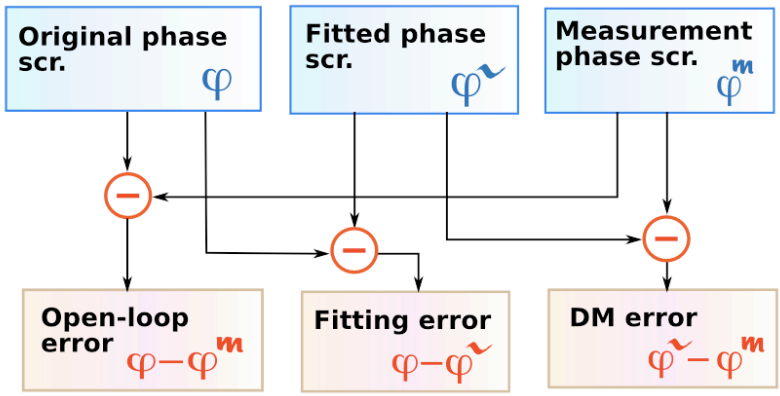

Figure 3.14: *Estimation of errors.*

The evaluation of the a_k coefficients is done by performing a least square fit (LSF) projection of the phase screen onto the influence functions, which corresponds to the minimisation of the Frobenius norm of $\varphi - F\cdot\, a$ with respect to a.

The minimisation of the norm corresponds to the following matrix operation:

$$a = F^{\dagger}\cdot\, \varphi \quad with \quad F^{\dagger} = (F^T F)^{-1} F^T \tag{3.4}$$

In the following, the a_k coefficients related to a particular phase screen are called the stroke map. Once the stroke maps are obtained, the fitted phase $\tilde{\varphi}$ can be reconstructed through the following matrix multiplication,

$$F\cdot\, a \;=\; \tilde{\varphi} \tag{3.5}$$

The process described through Eq. 3.3 to Eq. 3.5 is commonly called the projection of the phase screen onto the influence functions. Fig. 3.12 presents the fitted phase $\tilde{\varphi}$ obtained by the multiplication of the stroke maps and the influence functions F, and shows the corresponding stroke map, results of the projection of the phase screen onto the influence functions.

The phase screens φ have been scaled to fit the DM's maximum stroke capability. As a result, the stroke coefficients a_k also match the DM's stroke capability. Phase

screens φ and influence function phase maps are 106 by 106 pixels. To ensure the piston was removed properly, the mean value of both the generated phase screens φ and the stroke maps were checked to be equal to zero. In Sec. 3.2.2.4, the stroke coefficients will be utilized to generate the volt maps.

3.2.2.3 Fitting error minimisation

The multiplication of the stroke maps by the normalised influence functions provides the fitted phase screens $\tilde{\varphi}$. The fitting error is the result of the difference between the original phase screens φ and the fitted phase screens $\tilde{\varphi}$ (see Fig. 3.14). The fitting error gives an estimation of the limits of the DM's performance, due to the limited DM spatial resolution (limited number of actuators available to reproduce a given phase screen). This is the DM's sampling error. This shows how well the mirror can reproduce a specific phase screen when the only limiting factor is the number of actuators. The fitting error decreases as the number of actuators increases. Non-linear effects (such as the mechanical coupling between neighbouring actuators) are not taken into account in the estimation of the fitting error. This is due to the influence functions being obtained by releasing one actuator at a time, thus, the effects due to coupling between neighbouring actuators are not present.

The fitting error can be minimised by carefully choosing the size and position of the pupil projected onto the DM. In this experiment, the pupil is the interferometer mask. Fig. 3.15 (top) shows the variation of the fitting error for various interferometer mask sizes. The initial size is 110 by 110 pixels, which corresponds to the whole 18 by 18 array of actuators (see also Fig. 3.15 (bottom) for an illustration of the size and position of the mask onto the DM's active area). The mask size is decreased two pixels at a time with the phase screen being rescaled to maintain the initial phase property. The phase screen is not truncated, but rescaled over a smaller number of pixels through an interpolation process. The D and r_0 are identical, as well as the variance of the phase screen before and after rescaling, only the resolution varies. When the mask size decreases, the number of actuators available to reproduce the phase screen also decreases and the fitting error increases as a result.

The smallest fitting error is reached when the edges of the mask are positioned at

the centre of the actuators located at the edge of the 18 by 18 array (called the first outer actuator corona in Fig. 3.15 (top)). In this experiment, this corresponds to a mask of 106 by 106 pixels, represented by the red dashed line in Fig. 3.15 (bottom). Half of the actuators located on the first outer actuator corona are outside the pupil, thus, the DM area used to correct the turbulent phase screen is now only 17 by 17 actuators.

The minimisation of the fitting error occurs by optimizing the size of the projection of the entrance pupil on the DM's active area and is critical for the design of all optical elements located upstream (between the entrance pupil and the DM).

Note, in Fig. 3.15 (top), it appears that aligning the pupil to have approximately three quarters of the edge actuators in the pupil would generate the smaller fitting error while maximising the size of the pupil (which is desired in order to maximise the DM's spatial resolution).

3.2.2.4 Generation of the voltage command maps to be sent to the DM

Each actuator stroke-voltage plot can be fitted to a second order polynomial. Each polynomial fit provides two coefficients corresponding to the *offset* and the *gain* introduced in Eq. 3.2. To generate the volt maps, we inserted these coefficients into Eq. 3.1.

This equation is then inverted and, for an actuator k, becomes:

$$V(k) \; = \; \sqrt{\frac{a_k - offset(k)}{gain(k)}} \tag{3.6}$$

where the stroke maps (thus, the coefficients a_k) are estimated from the phase screens projection onto the normalised influence functions.

From this point forward, the volt maps can be obtained following two slightly different paths. With option A, the mean polynomial coefficients (for the offset and gain) from Eq. 3.1 are inserted into Eq. 3.6. With option B, each actuator's individual

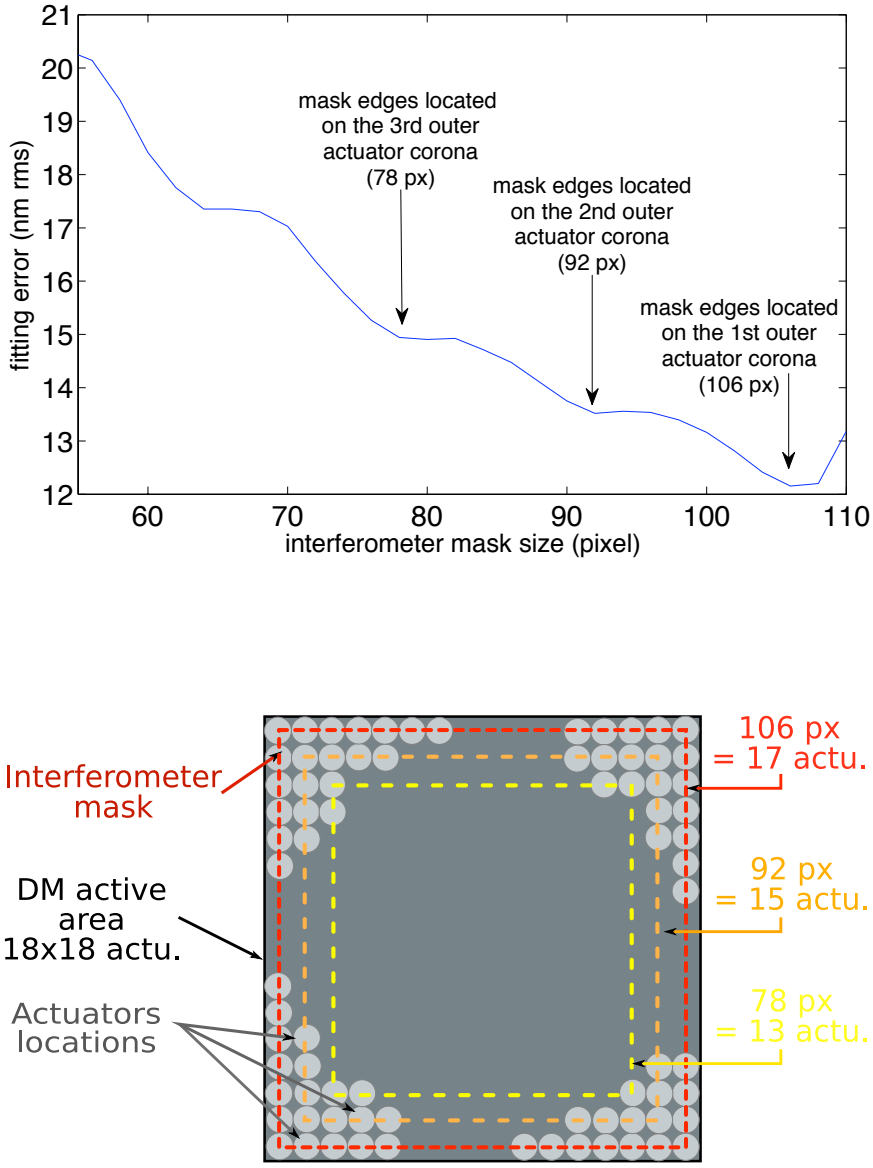

Figure 3.15: *Top, fitting error versus the size of the interferometer mask. Bottom, diagram of the interferometer mask size relative to the first three outer actuator coronas.*

polynomial coefficient is inserted into Eq. 3.6.

The comparison of rms performance obtained with these two options will be presented in the following sections. Note, for a given phase screen, the variations between the volt maps obtained with option A and option B are in the mV range. In Fig. 3.12, the volt map presented has been obtained with option A.

3.2.2.5 Statistical analysis of DM errors

Once the volt maps are computed, the voltage commands are sent to the DM. The measured membrane deflections corresponding to the projection of the phase screens onto the mirror are denoted by φ^m. Two sets of data are taken, one with option A and one with option B. Fig. 3.12 shows φ^m obtained with option A and the corresponding measurement or open-loop error. The open-loop error corresponds to the difference between the original phase screen φ and the measurement phase screen φ^m, which is the projection of the original phase screen onto the DM.

The DM error, corresponding to the difference between the fitted phase $\tilde{\varphi}$ and the measurement phase screen φ^m, provides an estimate of the error due to the DM non-linear effects (inter-actuator mechanical coupling).

For an initial mean rms phase screen of approximately 97 nm, the mean open-loop error is 16.5 nm rms, the mean fitting error is 13.3 nm rms and the mean DM error is 10.8 nm rms. The DM error is a critical value, because it reflects the ability of the modelling approach to predict the shape of the DM. Note, for the 100 phase screens tested, option A and option B give approximately the same performance. Option A is computationally less expensive than option B, and, thus, appears to be a more effective approach.

Fig. 3.16 shows a histogram representation of the rms distribution over the 100 phases tested for (i) the original phase screens, (ii) the stroke maps, (iii) the DM errors, and (iv) the open-loop errors for options A and B. The x-axis represents the rms wavefront error (nm wavefront) and the y-axis represents the number of corresponding phase screens. The lack of significant improvement between option A and

B is clearly visible.

An overview of this study is presented in Tab. 3.1 and Tab. 3.2. The values tabulated correspond to the mean value over the 100 phase screens generated and are given in nm rms.

phase scr.	stroke map	fitting error
96.7325 ± 20.4583	95.7828 ± 20.3680	13.3022 ± 3.2357

Table 3.1: *Mean and standard deviation rms of the fitting errors. All values are given in nm.*

option	open-loop	DM	$\frac{open\,loop}{phase\,scr.}$	$\frac{DM}{phase\,scr.}$
A	16.5272 ± 3.8791	10.7845 ± 2.6632	17.07%	11.14%
B	16.5427 ± 3.8896	10.8154 ± 2.6685	17.09%	11.17%

Table 3.2: *Mean and standard deviation rms of the measurement errors. All numbers are given in nm except for the ratio values given in %.*

Note that the results shown in Tab. 3.1 and Tab. 3.2 seems to indicate that the DM error and fitting error are correlated. Indeed, correlated entities do not add in quadrature while uncorrelated entities do add in quadrature. The DM error and fitting error do no add in quadrature, indicating that they should be correlated. This is a surprising result because the DM error and fitting error are expected to be uncorrelated.

3.2.3 Chapter conclusion

In this chapter, a low computational cost approach, referred to as *Mod1*, is used to control a MEMS DM in open-loop. This control strategy assumes the non-additivities of influence functions are negligible in the case of a DM shape that matches a random

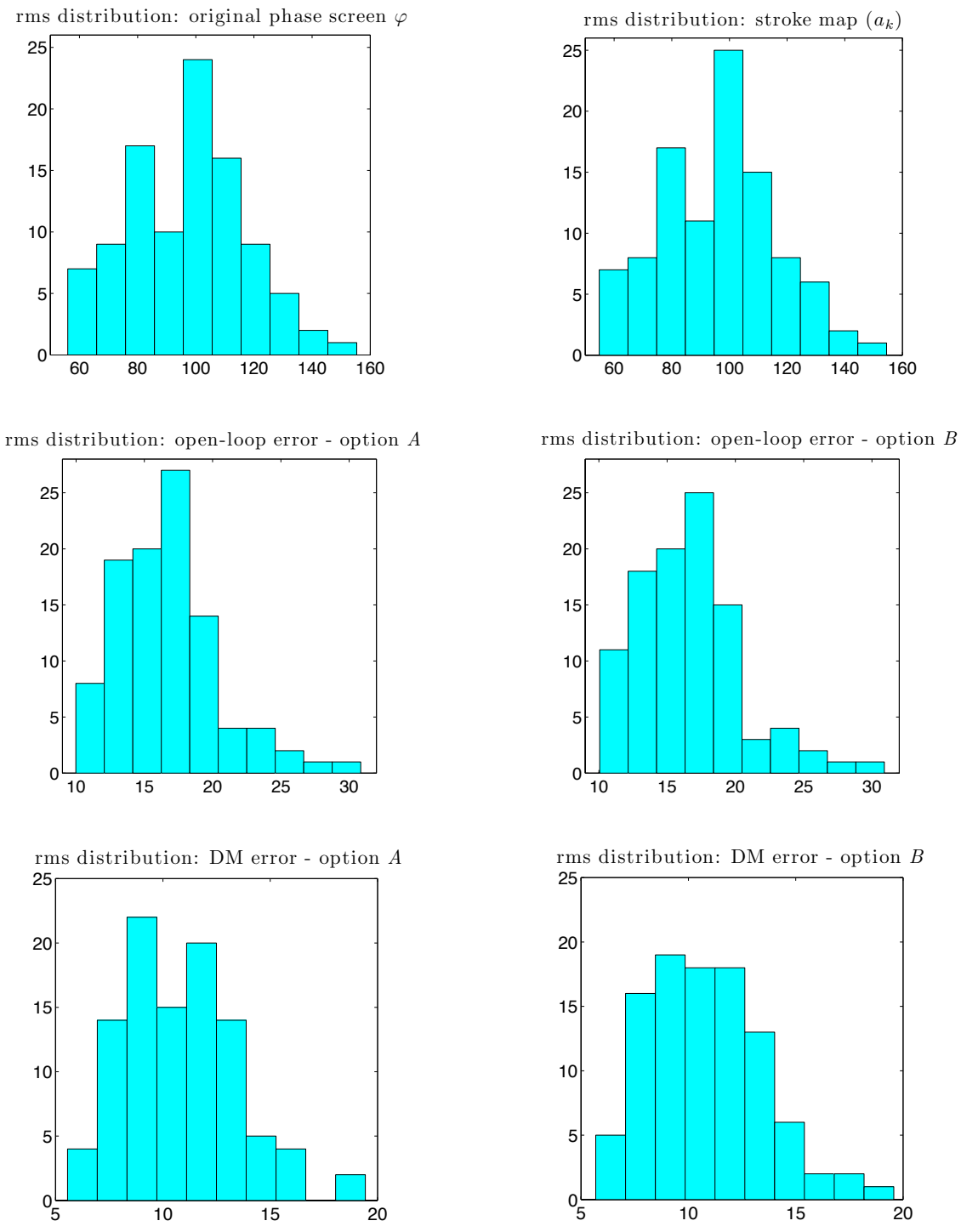

Figure 3.16: *Histogram representation of the statistical study over the 100 generated phase screens.*

Kolmogorov turbulence phase screen and has relatively low stroke. This approach appears to be a possible solution for imminent R&D in ExAO or MOAO system design, because of its promising results, its simplicity, and its low computational cost.

The DM is driven in stroke command, instead of voltage command. The relationship between the membrane deflection and the applied voltage is the carefully calibrated quadratic relationship.

Promising open-loop results with low residual rms error, obtained with a 1024-actuator MEMS deformable mirror, are shown. The characterization process relies on both the thorough stroke-voltage relationship calibration and the actuator influence function measurements.

A statistical study of 100 phase screens is performed. With an optimized characterization process, the residual open-loop error obtained is 17% and the residual DM error obtained is 11% (of the original phase screen rms). The test phase screens have a mean rms of approximately 97 nm, the mean open-loop error is 16.5 nm rms. With a mean fitting error of 13.3 nm rms, this brings the DM error to 10.8 nm rms. The DM error shows that *Mod1* is good to 10.8 nm within the spatial frequency accessible to the DM.

The fitting error is also highlighted as an important parameter for reducing the residual open-loop rms error. The projection of the entrance pupil onto the DM's active area will impact the optical design upstream and will need to be taken into account in the very early phase of the design. Sec. 3.2.2.3 shows that a minimised fitting error is obtained when the pupil edges are aligned with the centre of the actuators located at the edges of the DM's active area.

Chapter 4

Enhanced MEMS DM model for open-loop control on SCExAO

4.1 Chapter Introduction

This chapter introduces a high accuracy model, referred to as *Mod2*, allowing control of MEMS DMs for open-loop adaptive optics applications. The model relies on the forces applied on the DM actuators and the membrane. *Mod2* is also defined by a small number of parameters that are measured experimentally. The model is integrated into an iterative algorithm that applies forces and updates actuator displacements, allowing real-time utilization in an Extreme-AO system (control rate$\geqslant$1Khz). This work is the continuation of an initial approach [17] and also experimentally evaluates the improved model on a test bench developed at the UVic AO Lab.

The measurements show that *Mod2* reproduces Kolmogorov type phase screens with an error equal to **7.3**% of the rms of the desired phase (**1.6**% of the peak-to-valley desired phase). This performance corresponds to an improvement of a factor three compared with the standard quadratic model (common relationship between voltage and actuator displacement). Originally developed for the DM control of the Subaru Coronagraphic Extreme-AO (SCExAO) project, the model and algorithm are also suitable for Multi-Object AO systems.

4.2 Modelling MEMS DMs with *Mod2* and the iterative algorithm

4.2.1 General description of the method

The DM model and the iterative algorithm, used to transform command voltages into displacements (using the DM model), are illustrated in Fig. 4.1. They provide an accurate estimate of the DM shape without employing computationally intensive techniques, such as those derived from the thin plate theory [74, 62, 8].

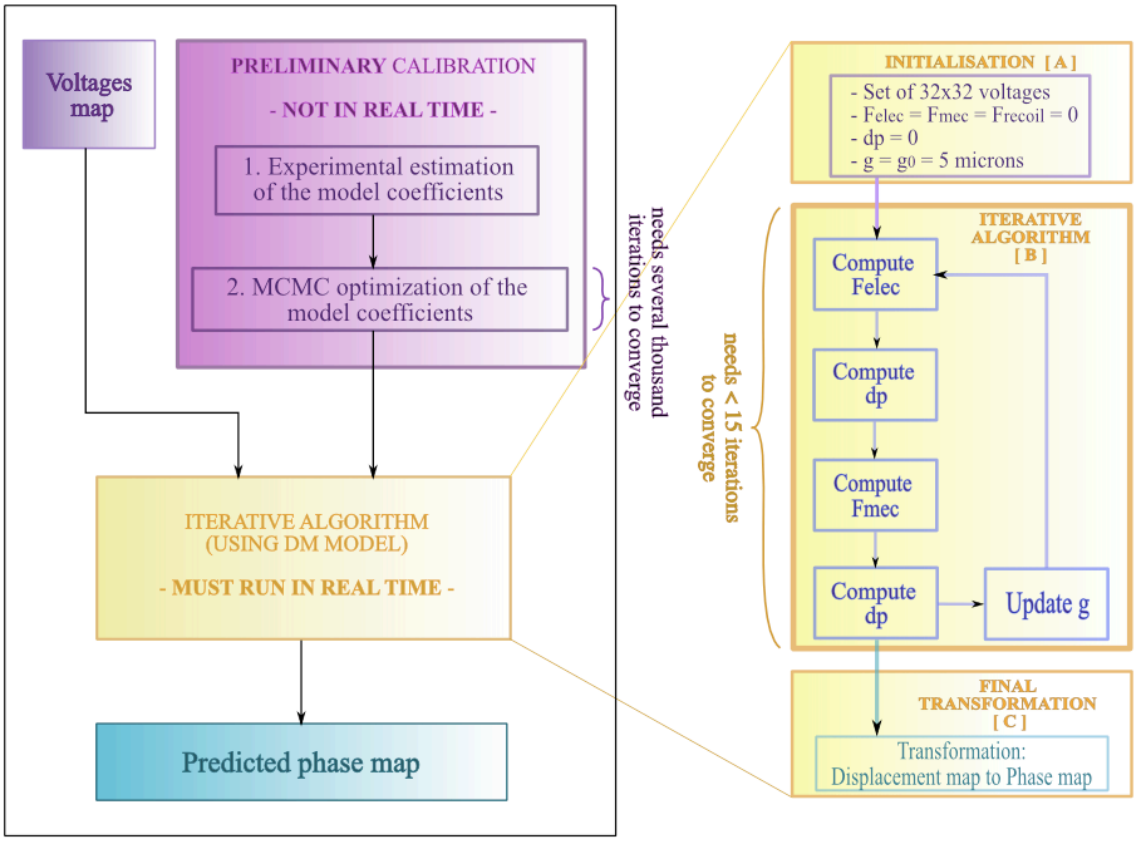

Figure 4.1: *Overview of the model and algorithm organization.*

Mod2 uses three force equations that represent the active forces during operation of the DM. As shown in Fig. 4.2, the forces are:

- The electrostatic force, F_{elec}, between the top actuator plate and the fixed actuator base,
- The mechanical coupling force, F_{mec}, between neighbouring actuators,

- The restoring force, $F_{restoring}$, of the actuator top plate.

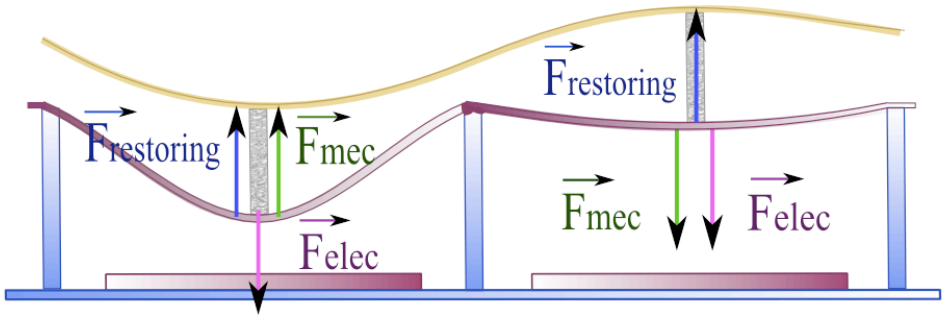

Figure 4.2: *Schematic of the forces acting on two neighbouring actuators. Due to the mechanical coupling, the left actuator is being pulled up (by the right actuator) and the right actuator is being pulled down (by the left actuator).*

The sum of all forces must equal zero for the system to reach a state of equilibrium. The simultaneity of the force action cannot be reproduced directly with numerical simulation, therefore, the model must be integrated into an iterative algorithm. The displacement of a specific actuator is adjusted in an iterative fashion until all forces applied to the actuator converge to the state of equilibrium.

The algorithm starts with an input volt map, and using *Mod2* (Block [B], Fig. 4.1) converges toward an output phase map (Block [C], Fig. 4.1).

To match the model to a given DM and a given experimental setup, a set of *model parameters* must be optimized during a preliminary calibration procedure, which consists of two main steps. First, a set of volt maps are applied to the DM. The interferometer is used to measure the DM shapes obtained in response to these voltages. Secondly, the same set of volt maps is used to generate modelled phase maps with the iterative algorithm. An optimization algorithm is then used to identify the values of the model parameters that result in the best match between the measured DM shapes and modelled phase maps. The optimization of the model parameters is critical in obtaining accurate results.

4.2.2 Definition of the model forces

4.2.2.1 Electrostatic force (F_{elec})

Each actuator is modelled as a capacitor with a fixed grounded plate electrode coupled with a movable top plate electrode. The capacity can be written as

$$C = \frac{\epsilon_0 \epsilon_r L w}{g} \tag{4.1}$$

with ϵ_0 as the permittivity of free space, ϵ_r the medium dielectric constant, L and w the actuator plate length and width (here $L = w$) and g the gap between the two plates.

The difference of potential, or voltage, between the two plates is denoted V and the potential energy can be written as

$$E_{pot} = \frac{1}{2} C V^2 \tag{4.2}$$

The electrostatic force F_{elec} can be written as

$$F_{elec} = -\frac{dE_{pot}}{dg} = -\frac{d}{dg}\left(\frac{\epsilon_0 \epsilon_r L w V^2}{2g}\right) \tag{4.3}$$

Finally, for a given actuator, indexed *(i, j)*, F_{elec} is given by the following relationship,

$$F_{elec}(i,j) = \frac{\epsilon_0 \epsilon_r L w}{2} \frac{V(i,j)^2}{g(i,j)^2} \tag{4.4}$$

with k_e as

$$k_e = \frac{\epsilon_0 \epsilon_r L w}{2} \tag{4.5}$$

The variables of Eq. 4.5 have the following physical values:

- $\varepsilon_0 = 8{,}854187.10^{-12}$ F.m^{-1}
- $\varepsilon_r = 1$ (air relative permittivity)
- L = w = 340 microns

As a result, k_e is estimated to be $k_e = 5.1153.10^{-19}$ F.m.

When the DM is at rest (no applied voltages), the initial distance between the two actuator plates, g_0, is specified by the manufacturer as 5 microns [2]. However, during the model iterations, the value of g varies with the estimation of the actuator vertical displacement, dp, as

$$g(i,j) = g_0 - dp(i,j) \tag{4.6}$$

4.2.2.2 Actuator plate restoring force ($F_{restoring}$)

Each square actuator plate is rigidly connected to the substrate along two of its edges and suspended above an addressable electrode [11]. When a voltage is applied, the top actuator plate is deflected toward the fixed bottom plate and is subjected to a bending load. The material naturally tends to return to a state of equilibrium, creating a restoring force $F_{restoring}$.

MEMS actuators can only be pulled in one direction (toward the fixed actuator base), so $F_{restoring}$ will always be in opposition to F_{elec}.

$F_{restoring}$ is modelled using the classical spring model and can be written as

$$F_{restoring}(i,j) = k_r.dp(i,j) \tag{4.7}$$

with dp(i,j), the vertical displacement of the actuator top plate toward the actuator base plate, and k_r, the spring constant of the actuator top plate.

4.2.2.3 Inter-actuator mechanical coupling force (F_{mec})

When a voltage is applied to an actuator, F_{elec} and $F_{restoring}$ balance and define the extent of the vertical displacement for this actuator. As illustrated in Fig. 4.2, a rigid post (represented in grey) connects the actuator top plate to the membrane. The membrane acts as a strong connection mechanism between neighbouring actuators. Thus, in addition to F_{elec} and $F_{restoring}$, the vertical displacement of the adjacent actuators needs to be estimated to accurately predict the vertical displacement of a given actuator in the array.

The mechanical coupling between neighbouring actuators, F_{mec}, can reach up to 30% (of the actuator displacement) for some DM technologies, but is usually only a low percentage for MEMS DMs. The following hypothesis was formed: the effect of one actuator is mainly localized to its first eight direct neighbours. The results presented in Fig. 2 of [45] confirm this is a reasonable assumption.

The vertical motion of a given actuator will be minimized, if the neighbouring actuators have lower displacements, and amplified, if the neighbouring actuators have larger displacements. Any configuration in between is possible. Therefore, F_{mec} can either be opposite to F_{elec} or in the direction of F_{elec}.

The classical spring model is chosen to represent the interaction between neighbouring actuators and takes the form shown in Eq. 4.8,

$$F_{mec}(i,j) = \sum_{p=1}^{4} k_m.(dp(i,j) - dp(perp_p) + \sum_{d=1}^{4} k_m.k_l.(dp(i,j) - dp(diag_d) \qquad (4.8)$$

$dp(i,j)$ represents the vertical displacement of the actuator of index (i,j). $dp(perp_p)$ corresponds to the vertical displacements of the four direct *perpendicular* neighbour actuators. As a result, $perp_p$ $(perp_1, perp_2, perp_3, prep_4)$ represents the actuators indexed (i+1, j), (i-1, j), (i, j+1), (i, j-1). $dp(diag_d)$ corresponds to the vertical displacements of the four direct *diagonal* neighbour actuators. As a result, $diag_d$ $(diag_1, diag_2, diag_3, diag_4)$ represents the actuators indexed (i+1, j+1), (i-1, j-1), (i+1, j-1), (i-1, j+1).

To simplify the notation, $dp(i,j) - dp(perp_p)$ and $dp(i,j) - dp(diag_d)$ will be named Δdp_p (for perpendicular) and Δdp_d (for diagonal) in the following. k_m is the spring constant. k_l is another model parameter dedicated to take into account the difference in the **lateral** distance between diagonal/perpendicular neighbouring actuators to the *central* actuator (see Sec. 4.2.3).

4.2.2.4 State of equilibrium

When the system is in a state of equilibrium, the sum of all active forces must be equal to zero:

$$F_{elec}(i,j) + F_{restoring}(i,j) + F_{mec}(i,j) = 0 \tag{4.9}$$

Using Eq. 4.7 and Eq. 4.9, dp can be written as

$$dp(i,j) = \frac{-(F_{elec}(i,j) + F_{mec}(i,j))}{k_r} \tag{4.10}$$

4.2.3 Description of the model parameters: DM parameters and geometrical parameters

It is important to match the model to a specific DM and its associated optical arrangement. Therefore, the model parameters are separated into two groups named *DM parameters* and *geometrical parameters*. Both set of parameters presented in Tab. 4.1 must be optimized during the calibration. The Markov Chain Monte Carlo (MCMC) algorithm is chosen to perform the optimization.

The use of "global" model parameters accompanies the assumption that the DM behaviour is isotropic. Exploring anisotropy is outside the scope of this work and could become a refinement of the work presented here. The residual fit numbers given in Sec. 4.4.2 are for an isotropic model and could be improved with a non-isotropic model (which would require additional calibration).

DM parameters

A first set of eight parameters describes the DM intrinsic physical characteristics. One DM parameter, k_e, is introduced in Eq. 4.5. The parameter k_r is part of Eq. 4.7. The restoring force is modelled using the spring equation. It is important to note that, as will be shown experimentally in Sec. 4.3.2, k_r, the spring constant, varies with the displacement of the actuator plate in a quadratic fashion,

$$k_r = k_{r_a} + k_{r_b}.dp + k_{r_c}.dp^2 \tag{4.11}$$

DM parameters	Description	Located in
k_e [F.m]	Param. for F_{elec}	Eq. 4.4 / Eq. 4.5
k_{r_a} [N.m^{-1}]	Param. for $F_{restoring}$ - 0 order	Eq. 4.7
k_{r_b} [N.m^{-2}]	Param. for $F_{restoring}$ - 1^{st} order	Eq. 4.7
k_{r_c} [N.m^{-3}]	Param. for $F_{restoring}$ - 2^{nd} order	Eq. 4.7
k_{m_a} [N.m^{-1}]	Param. for F_{mec} - 0 order	Eq. 4.8
k_{m_b} [N.m^{-2}]	Param. for F_{mec} - 1^{st} order	Eq. 4.8
k_{m_c} [N.m^{-3}]	Param. for F_{mec} - 2^{nd} order	Eq. 4.8
k_l [-]	Param. for F_{mec} - geometrical factor	Eq. 4.8
Geometrical parameters	Description	–
X shift [m]	Shift along the x-axis	–
Y shift [m]	Shift along the y-axis	–
DMangle [rad]	DM rotation with respect to the beam	–
DMprojAngle [ratio]	Projection angle of the beam onto the DM	–
DMactusize [m]	DM actuator size	–
DMpixscale [m.px^{-1}]	Pixel scale	–
Size [px]	Size of the phase map on the detector	–
IF_{width} [m]	Gaussian FWHM for the influence function	–

Table 4.1: *List of DM parameters and geometrical parameters.*

To simplify the notations, $dp(i,j)$ is simply named dp and represents the vertical displacement of the actuator under evaluation. As a result, k_{r_a}, k_{r_b} and k_{r_c} are three additional DM parameters to be optimized (with powers arranged in ascending order of the second order polynomial k_r).

Similarly, it will be shown in Sec. 4.3.2 that, k_m, the spring constant dedicated to the expression of F_{mec}, actually varies with the degree of stretching of the membrane. k_m also follows a quadratic law (Eq. 4.12). Three additional parameters are thus dedicated to the inter-actuator mechanical coupling F_{mec}. The parameter k_m is estimated by examining the relative difference in displacement between an actuator and its eight direct neighbours, or Δdp.

$$k_m = k_{m_a} + k_{m_b}.\Delta dp + k_{m_c}.\Delta dp^2 \tag{4.12}$$

To simplify the notation, both Δdp_p and Δdp_d have been encompassed inside Δdp.

Finally, k_l is used to take into account the geometrical difference in the **lateral** distance between the perpendicular neighbouring actuators and the diagonal neighbouring actuators to the central actuator.

Geometrical parameters

To match the model with a specific experimental setup, a set of geometrical parameters must also be estimated. One parameter is dedicated to the transformation from the displacement map to the phase map. The FWHM of the Gaussian function (used to represent the influence function of the actuator) is set as a free parameter.

The remaining parameters take into account any misalignment existing in the system (possible translation along the x- and y-axis, possible rotation of the image on the detector). They also take into account the projection angle of the beam onto the DM, the pixel scale, the size of the image on the detector, and the size of the actuators.

The vertical displacement of a given actuator is affected by the vertical position of the surrounding actuators. This is due to two coupled phenomena. First, the FWHM of the Gaussian function defines the extent of the impact of an actuator motion over

its neighbours. Second, the mechanical coupling between adjacent actuators defines how the vertical position of a given actuator is biased by the vertical position of its neighbours.

The model provides an optimal balance between these two phenomena, due to the optimization of both (i) the parameter related to the Gaussian FWHM (IF_{width}) and (ii) the parameters related to F_{mec} (k_{m_a}, k_{m_b} and k_{m_c}).

It is important to note that, although F_{mec} and IF_{width} are coupled, both parameters are necessary to the model because they intervene at different levels. F_{mec} allows to compute dp, while, IF_{width} allows to convert the displacement map to a "continuous" phase map.

4.2.4 Description of the iterative algorithm used for DM shape computation

4.2.4.1 Algorithm input-output

The iterative algorithm is illustrated in Fig. 4.3. The algorithm input is (i) a set of actuator voltages to be applied to the array of actuators and (ii) the model parameters (Tab. 4.1). Using the model equations presented in Sec. 4.2.2 and the DM parameters (Sec. 4.2.3), the iterative algorithm generates an output vertical displacement map (having the same dimension as the input volt map) named hereafter the *displacement map*. The displacement map is then transformed into a phase map of size defined by the user (for example, 256 by 256 pixels or 1024 by 1024 pixels).

The actuator influence function (see Chap. 2) is the characteristic shape of the mirror response to the action of a single actuator. Influence functions can be represented using Gaussian functions. To go from the displacement map to the phase map, the algorithm performs a proper normalization of the influence function to ensure that the volume under the influence function is equal to the area corresponding to an actuator pushed to the nominal displacement. This is critical to ensure that if all actuators are pushed to 1 micron, the mean value of the membrane shape obtained is actually 1 micron.

The final phase map (constituting the output of the iterative algorithm) is then

constructed by the cumulative sum of the multiplication, point by point, of the displacement map by the normalized influence function. The geometrical parameters (Sec. 4.2.3) are integrated in this step, to provide the capability of adding geometrical transformations in the final image.

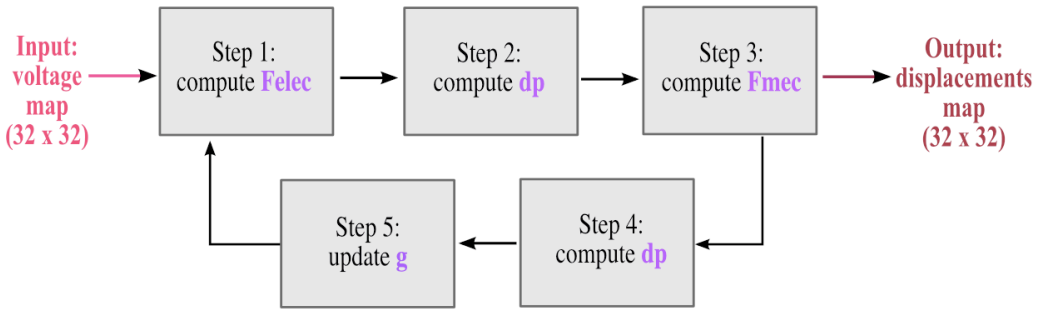

Figure 4.3: *Detail of the iterative algorithm. The input is a volt map and after a few iterations of Step 1 to Step 5, the algorithm converges to a displacement map.*

After the algorithm initialization (Block [A], Fig. 4.1), the algorithm iterations begin and can be subdivided into four sub-steps, which are described below:

Step 1: For each actuator of the array, the electrostatic force $F_{elec}(i,j)$ is computed using Eq. 4.4.

Step 2: A first estimation of the displacement *dp(i,j)* of each actuator is computed using Eq. 4.10. During the first iteration only, $F_{mec}(i,j)$ is set equal to zero and the DM is modelled as if it had a segmented membrane. For all the following iterations, the value of $F_{mec}(i,j)$ will be the outcome of Step 3 from the *previous* iteration.

Step 3: For each actuator of the array, $F_{mec}(i,j)$ is computed using Eq. 4.8.

Step 4: An updated estimation of *dp(i,j)* is computed using Eq. 4.10. At this point, $F_{mec}(i,j)$ is always the outcome of Step 3 from the *current* iteration.

Step 5: The size of the gap, $g(i,j)$, is also adjusted using Eq. 4.6.

When Step 5 is completed, the output value for $F_{mec}(i,j)$ is set as the new $F_{mec}(i,j)$ input value for the next iteration and the algorithm starts back at Step 1.

When the iterations are complete, the output is the 32 by 32 displacement map, which will be transformed into a phase map during the "Final Transformation" (Block [C], Fig. 4.1).

4.2.4.2 Initial conditions for the iterative algorithm

The initial conditions are given below:

- The initial gap between the actuator top plate and the fixed actuator base plate, g_0, is equal to 5 μm [2]
- All forces are equal to zero ($F_{elec}(i,j) = F_{restoring}(i,j) = F_{mec}(i,j) = 0$)
- The displacement of each actuator is equal to zero ($dp(i,j) = 0$)
- Each model parameter is set to its optimized value determined during the initial calibration.

4.2.4.3 Constraining the maximum actuator displacements

The reflective membrane, laid on top of the actuator array, is clamped to the edge of the DM structure. Although clamping is located outside the area of interest, it still affects the edge actuators by minimizing their maximum vertical displacement in comparison to the maximum displacement achievable by the rest of the actuator array. To take into account this limitation, a constraint is added to the model: the maximum displacement of the edge actuators is set to a smaller value than the maximum displacement set for the rest of the actuators.

A systematic verification of the computed value of dp for each actuator is performed in Step 2 and Step 5. Any actuator (central or edge) with a computed displacement exceeding the authorized measured value (dp_{max} or dp_{edge} respectively) is reset to the maximum value allowed.

4.3 Preliminary calibration of the model parameters

4.3.1 Description of the Markov Chain Monte Carlo algorithm

In order to accurately estimate the optimum value for each parameter, a MCMC algorithm is implemented. However, for the MCMC to perform efficiently, it is critical to start with initial values that are close to the real values. Thus, an experimental estimate of the model parameters is first performed (described in Sec. 4.3.2).

The MCMC algorithm is a variation of the classical Monte Carlo algorithm and has the advantage of only performing computations in the regions where the data optimization is improving.

The goal of the model is to reproduce, with the highest accuracy, the phase map produced by the DM for a given set of voltages. The model inputs are:

- The same set of voltages (volt map) sent to the DM
- The set of model parameters.

To optimize the value of model parameters, the MCMC minimizes the difference (residual error rms) between the "modelled" phase map and the original (measured) phase map.

During each iteration, two series of parameters are randomly selected, named hereafter "Set I" and "Set II", and the model performance are evaluated for each set. The difference between the modelled and original maps (in the rms value) is estimated for Set I and Set II. The set which provides the smallest difference corresponds to the best match between the model parameters and the real DM.

Each iteration of the optimization procedure is organized as follows:

(i) The MCMC starts with a set of user-defined initial parameters, corresponding to Set I. The values of these initial parameters are defined experimentally

(ii) Using Set I, the residual rms error, Φ_1, between the modelled phase map and the measured phase map is estimated

(iii) A second set of parameters is randomly picked and the residual rms error obtained with Set II, Φ_2, is estimated. To generate a new value for each parameter of Set II, a random number (positive or negative) is added to each parameter of Set I (each parameter has a specific number added or subtracted). The range of values accessible to each parameter is user-defined at the beginning of the algorithm and based on results found during the initial experimental evaluation of the model parameters. This range can be adjusted during the optimization

(iv) The ratio of the residual rms error, R, between Set I and Set II is then computed as

$$R = \frac{\Phi_1}{\Phi_2} \tag{4.13}$$

(v) If R $\geqslant$ 1, Set II gives the best fit between the DM and the model. The algorithm moves toward the region of lower residual rms. Set II is saved as the new Set I for the next iteration

(vi) If R $<$ 1, Set II is not better than Set I. A random number U taken between 0 and 1 is picked (using a uniform distribution)

- If U $\leqslant$ R, Set II is selected to be the starting set for the next MCMC iteration, which gives a chance to explore some regions where the residual rms is larger
- If U $>$ R, Set I is selected to be the starting set for the next MCMC iteration

(vii) The parameters of the selected set are saved as the new Set I for the next iteration and the loop starts back to step (ii).

4.3.2 Experimental estimate of the model parameters

The MCMC algorithm requires a reasonably accurate initial estimate of the parameter set in order to converge. This is achieved by an experimental characterization that also produces values for dp_{max} and dp_{edge}.

The experimental data presented below and in Sec. 4.4 are generated using the following experimental setup: the MEMS DM is fixed on a 5-degrees-of-freedom mount (x, y, z, and tip-tilt) and positioned in front of the interferometer. Two filters are also inserted in front of the interferometer window to optimize the fringe contrast and improve the measurement quality.

All volt maps and phase maps used in the following had a *reference area* and an *active array* (see Fig. 4.4, left). The reference area is the outer corona of seven actuators across (actuator 1 to 7 and 26 to 32 for both rows and columns). The central active array is eighteen by eighteen actuators wide. The reference area is set to 0 volt at all times and has two purposes:

- To accurately define a zero reference point for the interferometer measurements. Because the piston is not visible, this zero reference point is necessary to improve the accuracy in the estimate of the displacement for each actuator of the active array
- To mitigate the effect of the defective actuator (located at row 6, column 22). This actuator follows the motion of the array up to approximately 90 V, then stays below the other actuators when the voltage is pulled to higher values. The model performance is thus estimated for the active area, which contains only valid actuators.

Fig. 4.4 (right) shows a phase measurement of the array of 32 by 32 actuators pulled to 100 V. The dead actuator appears on the bottom right part of the image and the white dashed square shows the limit of the selected active array of the DM.

The level of precision of the interferometer measurements was verified to ensure it did not compromise the evaluation of the performance obtained with the model. Hence, the rms error on the interferometer measurements should be small compared

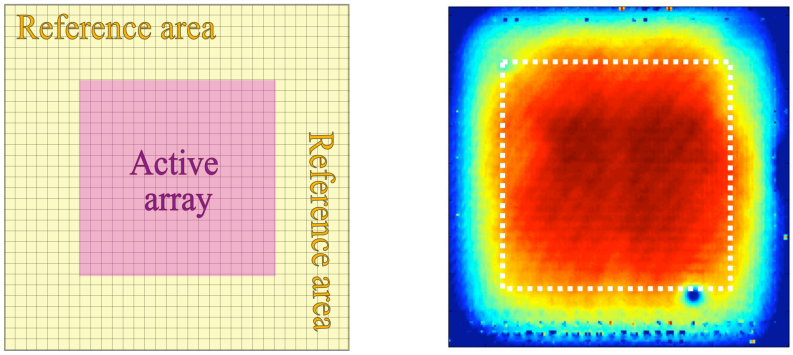

Figure 4.4: *Left, location of the active array and reference area. Right, phase measurement for the array of 32 by 32 actuators pulled to 100 V.*

with the model rms error, to confidently validate the model performances.

To evaluate the interferometer noise, the rms error for the difference of two consecutive measurements of the same phase screen is compared to the phase screen rms. The percentage obtained between the error rms and the phase screen rms is 0.0332%, which is roughly a factor one hundred smaller than the percentage obtained for the model performance evaluation. The interferometer precision is, thus, sufficient to validate the model performances.

4.3.2.1 Measurement of the DM maximum displacement (dp_{max})

The maximum vertical displacement dp_{max} should be reached when all actuators are pulled to the maximum voltage of the device, 200 volts. However, because a reference point is needed to accurately estimate the displacement, only the active array is set to 200 volts. This will not impact the performance of the model, because all volt maps will have the identical reference area and active array.

Fig.4.5 (top) shows the phase measurement of the 32 by 32 array with the active array set to 200 volts. The vertical cut along the centre of the membrane is presented on the bottom image. The maximum displacement is estimated as $dp_{max} = 1.6$ μm.

The interferometer measurements become corrupted when the dynamic range of the displacement become too large. This effect is evident in Fig. 4.5, where the reference area appeared split in two regions (dark blue and light blue).

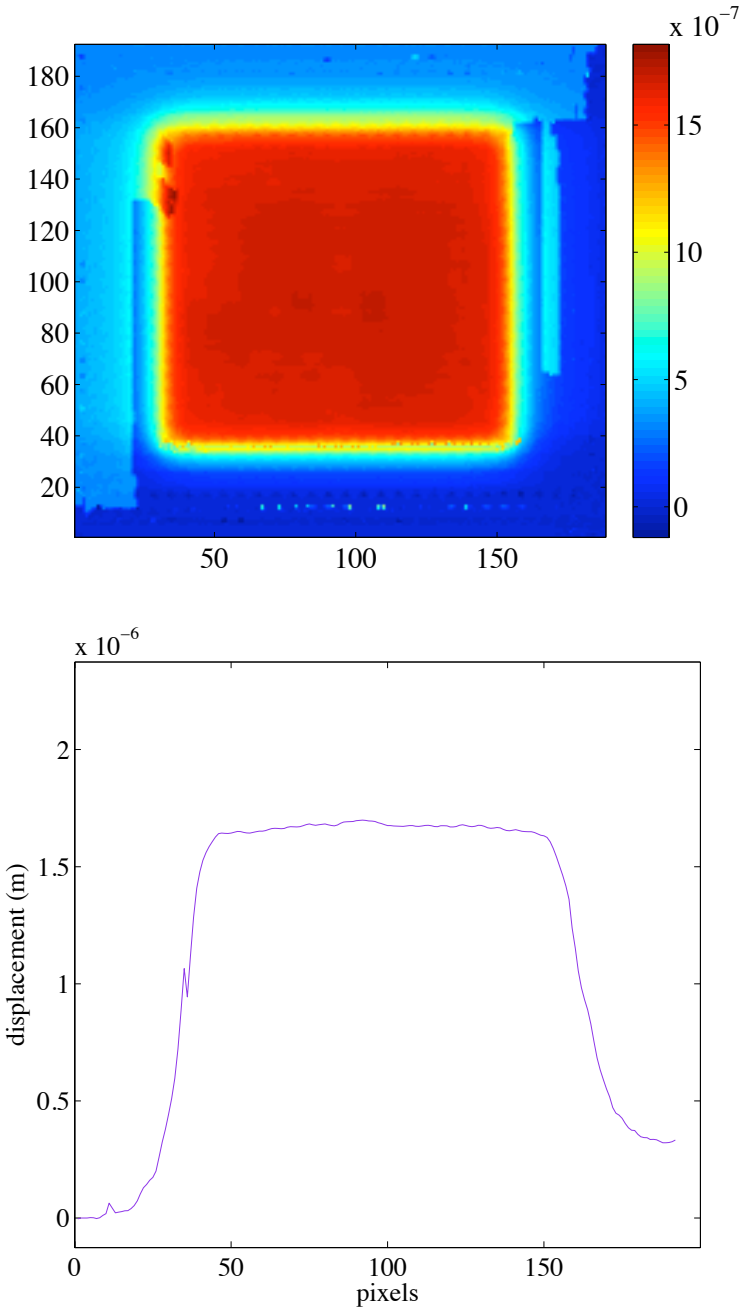

Figure 4.5: *Top, phase measurement of the 32 by 32 array. The active array is set to 200 V (in red), the reference area is left to 0 V (in blue). Bottom, transversal cut of the phase measurement.*

4.3.2.2 Measurement of the maximum displacement for the edge actuators (dp_{edge})

The motion of the first outer ring of actuators is constrained, because the membrane is clamped at the edges. To measure the maximum displacement of the edge actuators, all actuators of the 32 by 32 array are pulled to 200 volts, while the last five left rows are maintained to 0 volt. The zero-volt plateau is required to accurately measure the maximum displacement, as it provides a zero reference point for the measurement.

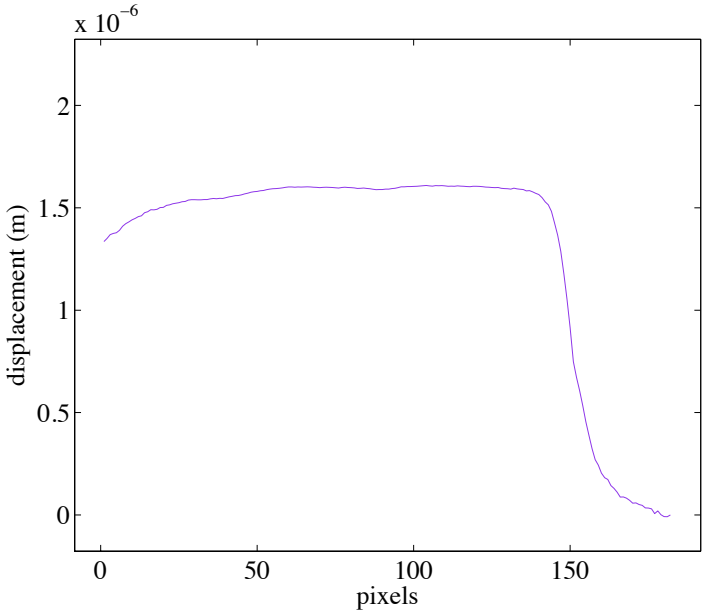

Figure 4.6: *Transversal cut of the phase measurement of the edge actuator maximum displacement.*

Fig. 4.6 shows a cross-sectional view along the membrane with the five rows of actuators maintained at 0 volt to the right and the lifted-up edge of the mirror to the left. The mean value of the measured displacement on the left edge is $dp_{edge} = 1.3\mu$m.

For this specific experimental setup, the evaluation of dp_{edge} is not critical because the seven outer coronas of actuators are constantly maintained at 0 volt. To apply this model to a full 32 by 32 active array, an accurate estimation of dp_{edge} would be an important constraint.

4.3.2.3 Measurement of the actuator influence function

During the transformation from the displacement map to the final phase map, a Gaussian function (defined by its FWHM) is used to represent the actuator influence function.

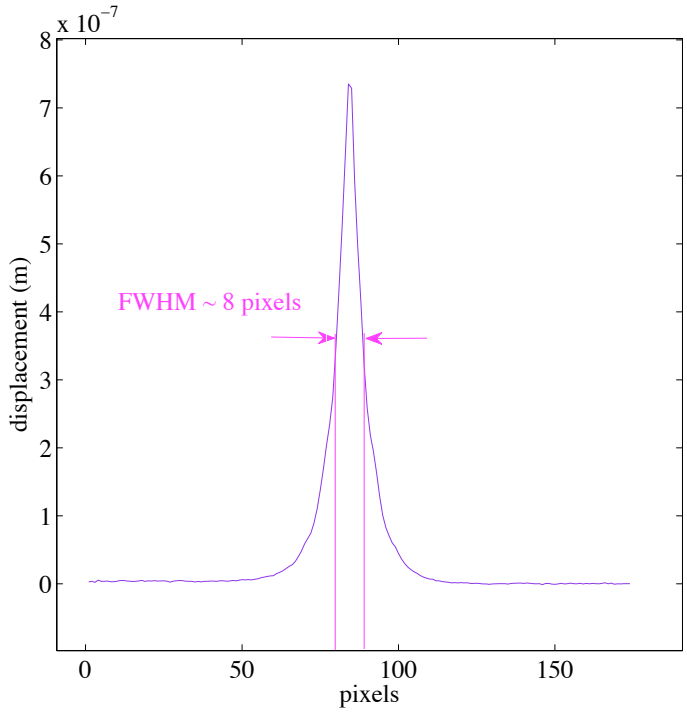

Figure 4.7: *Phase measurement (cross-sectional view) of the influence function.*

The parameter corresponding to the FWHM value can be experimentally estimated by measuring the real influence function of one of the actuators. Fig. 4.7 shows a measurement (cross-sectional view) of the influence function for actuator [16,16] when pulled to 160 volts, while the rest of the array is maintained at 0 volt. The FWHM can be estimated to approximately 8 pixels.

4.3.2.4 Measurement of the DM parameter k_r

The parameter k_r introduced in the restoring force equation (Eq. 4.7) is estimated experimentally by successively pushing the active array to voltages varying from 20

volts to 120 volts in steps of 20 volts, while the rest of the actuators (reference area) are maintained at zero.

For the actuators located at the centre of the active array, the mechanical coupling can be approximated to zero, because all actuators are at the same voltage and, therefore, at the same approximate vertical displacement. For the central actuator, the following assumptions are made:

- $F_{elec}(i,j)$ is computed from Eq. 4.4. The voltage is known and $k_e = 5.1153.10^{-19}$ F.m.
- $dp(i,j)$ is known from the interferometer measurement
- $F_{mec}(i,j)$ is approximated to zero.

Fig. 4.8 (top) shows the actuator displacement $dp(i,j)$ obtained along the central cross-section of the active array when pulled from 20 volts to 120 volts. The evaluation of $dp(i,j)$ is done by measuring the mean value over the range of pixels from 70 to 100 (black arrow above the plots). The variation of k_r with respect to $dp(i,j)$ is plotted in Fig. 4.8 (bottom).

Tab. 4.2 can be established using Eq. 4.10. The parameters obtained from the quadratic fit of k_r are presented in Tab. 4.3.

voltage [V]	dp [m]	k_r [N.m^{-1}]
20	$4.8471.10^{-8}$	-172.1756
40	$1.9796.10^{-7}$	-179.2956
60	$4.2673.10^{-7}$	-206.3309
80	$6.6975.10^{-7}$	-260.6816
100	$8.9657.10^{-7}$	-338.8381
120	$1.1125.10^{-6}$	-438.1271

Table 4.2: *Look up table established for the experimental evaluation of k_r.*

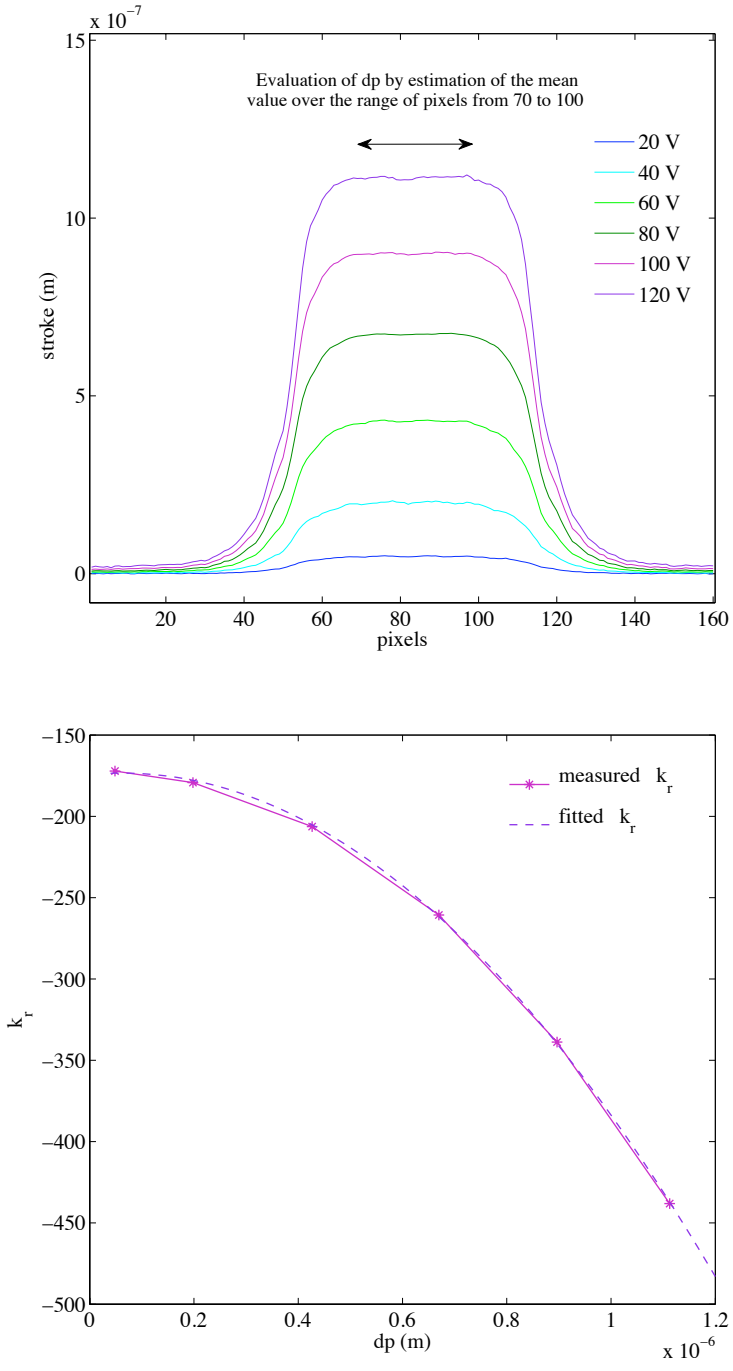

Figure 4.8: *Top, phase measurements of the vertical displacement obtained for the central active array. Bottom, variation of* k_r *with respect to* $dp(act_{16})$ *and its quadratic fit.*

k_{r_a}	k_{r_b}	k_{r_c}
-174.3638	$2.9753.10^{7}$	$-2.3916.10^{14}$

Table 4.3: *Values obtained during the experimental evaluation of* k_r.

4.3.2.5 Measurement of the DM parameter k_m

Once k_r is known for a given dp, the same process is applied to the membrane spring constant, k_m. The central active array of actuators is successively pulled from 40 volts to 120 volts in steps of 20 volts, while actuator [16,16] is maintained at 40 volts.

In this configuration, actuator [16,16], named act_{16}, is always subjected to the same voltage. Without mechanical coupling, the vertical position of this actuator should not vary when the rest of the active array moves from 40 V to 120 V. The observed increase in the vertical displacement of act_{16} is due to the action of the height neighbour actuators, which are pulling act_{16} upward through mechanical coupling of the membrane.

Fig. 4.9 (top) shows the cross-sectional view of the array passing on top of act_{16} for the five different voltages (40 V to 120 V) and the vertical displacement $dp(act_{16})$ for act_{16}. Δdp is estimated for each voltage by measuring the difference between the vertical displacement of act_{16} and the vertical displacement of its eight neighbours.

Using the following assumptions,

- k_r is estimated from the optimized values of the quadratic fit
- $F_{elec}(act_{16})$ is computed with $k_e = 5.1153.10^{-19}$ F.m.
- act_{16} diagonal and perpendicular neighbours are considered to be at the same lateral distance from act_{16} (this corresponded to set $k_l = 1$)
- Δdp is considered to be the same for each of the eight neighbours.

The value of k_m can be estimated from Eq. 4.4, Eq. 4.7 and Eq. 4.8,

$$k_m = \frac{-(F_{elec}(act_{16}) + k_r.dp(act_{16}))}{8.\Delta dp} \tag{4.14}$$

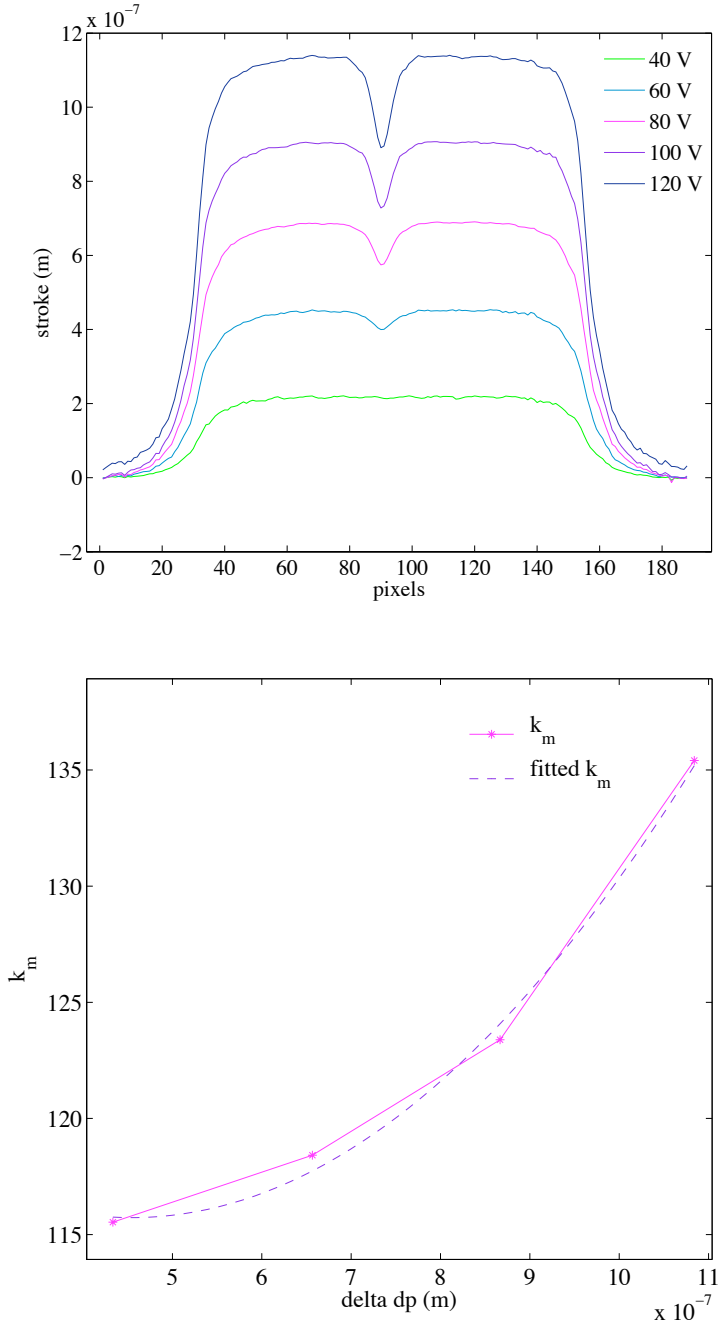

Figure 4.9: *Top, measurements of the displacement obtained along the vertical cut passing on top of* act_{16}*. Bottom, plots of* k_m *and its quadratic fit over the range of* Δdp*.*

Plotting k_m with respect to Δdp shows a quadratic variation. Fig. 4.9 (bottom) shows the plot of k_m with respect to Δdp and the corresponding quadratic fit.
The parameters obtained from the second order polynomial fit of k_m are presented in Tab. 4.4.

k_{m_a}	k_{m_b}	k_{m_c}
115.8480	-4.4560.10^7	4.9054.10^{13}

Table 4.4: *Values obtained during the experimental evaluation of k_m.*

As demonstrated above, both k_m and k_r (the spring constant for the inter-actuator mechanical coupling and the actuator top plate restoring force, respectively) are not of constant value, but instead vary following a quadratic law. This is due to the fact that the model is not perfect and uses a limited number of degrees of freedom to evaluate the shape of the DM membrane. During the MCMC optimization of the model parameters, the physical parameters of the DM, which are not taken into account by the model, will impact the value of the model parameters. This also explains the difference between the theoretical value (for k_e) and the experimental values (for $k_{m_{a-c}}$, $k_{r_{a-c}}$ and k_l) and their optimized counterparts (see Tab. 4.5).

4.4 First laboratory demonstration: evaluation of *Mod2* performance

4.4.1 Figures of merit

In accordance with the techniques of the previously reported experiments, two figures of merit (FOM) are described to quantify the model performance. The two FOM are similar to Guzmán [46] metric and are defined below:

- The ratio of the residual error rms to the Peak-to-Valley (PV) excursion of the desired wavefront correction

$$R_{rms/PV} = \frac{residual_{rms}}{desired_{PV}} \tag{4.15}$$

- The ratio of the residual error rms to the rms value of the desired wavefront correction

$$R_{rms/rms} = \frac{residual_{rms}}{desired_{rms}} \tag{4.16}$$

4.4.2 Performance of *Mod2* with Kolmogorov type phase screens

The model performance is assessed over the active array of 18 by 18 actuators (and, therefore, avoiding the defective actuator) and using the experimental setup discussed in Sec. 4.3.2. This corresponds to a central 100 by 100 pixels phase map.

Although Zernike polynomials (Appendix B) are commonly adopted to estimate a model performance, the goal of this experiment is to evaluate the phase residual when the model is confronted with phase aberrations similar to the one encountered with atmospheric turbulence. As a result, a set of ten different volt maps is generated, corresponding to voltages that would be sent to the DM when trying to compensate for Kolmogorov turbulence. We note that decomposition of Kolmogorov phase screens into Zernike polynomials can be performed to establish correspondence between the two metrics.

An offset of 90 V is applied to all volt maps to set the DM in the mid-range displacement. The model parameters are first estimated following the calibration procedure described in Sec. 4.3.2. Then, the MCMC optimization is accomplished by simultaneously minimizing the residual rms error (Eq. 2.5) obtained with five sets of measured phase and their corresponding modelled phases.

The number of measurements (ten) presented in this section is limited. However, provided that (i) the model assumes the parameters of the model are the same for all actuators and (ii) there are 18 by 18 actuators and 10 phase maps, the performance is evaluated over a sample of 3240 data points, which is much larger than the number of parameters to optimize (15). Furthermore, the ten phase screens used had PV values varying from 1311 nm to 1716 nm and rms values varying from 474 nm rms to 526 nm rms. For each actuator, the 10 displacement values sample approximately 500 nm rms of displacement around the actuator nominal position (chosen here to be 90 volts). Assuming the position of each actuator is a function of the voltage applied as well

as the voltage applied to its height surrounding actuators, the data sample consists of 360 independent 3 by 3 blocks of voltage with the differential voltage between adjacent actuators representing realistic atmospheric properties. When conservatively accounting for inter-actuator couplings, the number of independent measurements (360) is still much larger than the number of parameters (15) and we, therefore, conclude that the ten phase screens are sufficient to constrain these parameters.

We note that high precision derivation of the model parameters or, equivalently, high precision analysis of the residuals after parametrization of the DM with our model would require a larger number of phase screens. The goal of this chapter is, however, simply to present the first results from a new DM modelling approach. We want to show that *Mod2* and the iterative algorithm can be easily implemented and provides a significant improvement over the simple quadratic voltage-displacement law often used for MEMS devices. For these goals, analysis of ten phase screens is sufficient.

Mod2 performance is estimated, in percent, using the two figures of merit defined in Sec. 4.4.1. Five of the phase screens have been introduced inside the MCMC optimization algorithm. The five remaining ones are used to check the model performance and verify that *Mod2* can accurately reproduce a given phase screen once the parameters have been optimized. The number of iterations necessary for the model to converge to a state of equilibrium is low (≤ 15).

The residual error rms varied from 13 nm rms to 20 nm rms, resulting in model performances oscillating between **1.6**% and **3.2**% (for the "rms error/PV" FOM) and between **7.3**% and **14.6**% (for the "rms/rms" FOM).

The values of the model parameters defined during the MCMC optimization step and used to evaluate the *Mod2* performance are listed in Tab. 4.5. Fig. 4.10 shows five sets of measured phase maps (left) and their corresponding simulated phase maps (middle), as well as the difference between the measure and the model (right). The top two sets have been used to run the model parameter optimization.

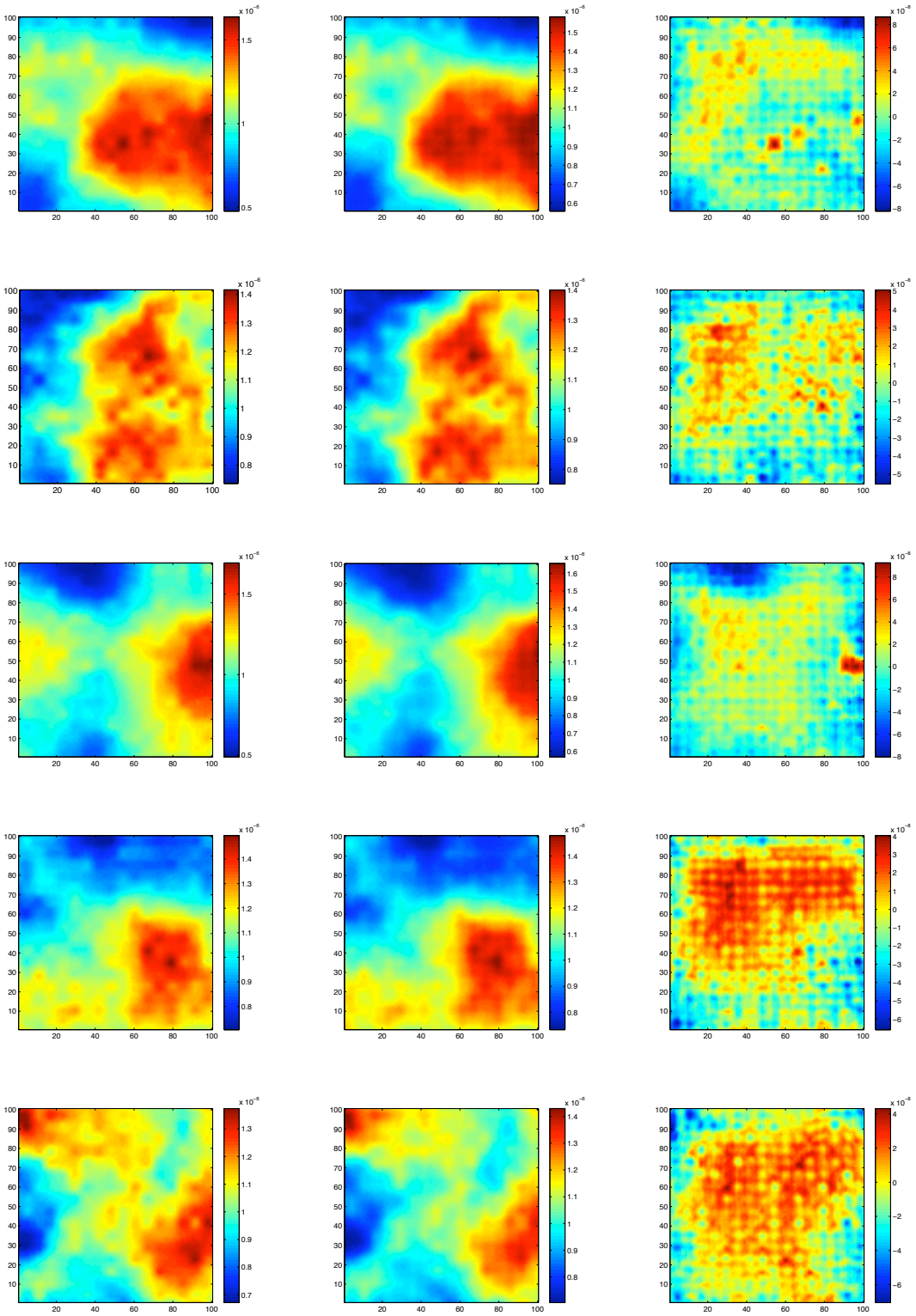

Figure 4.10: *Left column: measured phase (in m). Middle column: modelled phase (in m). Right column: difference between measured and modelled phase (in m).*

DM parameters		Geometrical parameters	
k_e [F.m]	$1.42299.10^{-18}$	Shift in x [m]	$-6.65599.10^{-5}$
k_{r_a} [N.m^{-1}]	-1332.66	Shift in y [m]	$-3.88445.10^{-5}$
k_{r_b} [N.m^{-2}]	$1.57182.10^{8}$	Rotation [rad]	0.00798692
k_{r_c} [N.m^{-3}]	$-7.25453.10^{14}$	Beam projection angle [ratio]	0.985234
k_{m_a} [N.m^{-1}]	35.5179	DM actuator size [m]	0.00065777
k_{m_b} [N.m^{-2}]	$1.12478.10^{-5}$	Pixel scale [m.px^{-1}]	0.0001052
k_{m_c} [N.m^{-3}]	$2.26682.10^{13}$	Gaussian FWHM [m]	$2.6579.10^{-7}$
k_l [-]	6.2802		

Table 4.5: *Model parameters resulting from the MCMC optimization. The phase map is 167 by 167 pixels.*

4.4.3 Performance comparison with previous modelling approaches

Mod2 performance is compared with Morzinski[62], Guzmán[46], and *Mod1*, as they correspond to the models tested using either Kolomogorov or random type phase screens. The values for *Mod2*, presented in Tab. 4.6, are the mean value over the ten phase screens under test.

Mod2 performance has been compared with the performance obtained using the standard quadratic model (SQM). The SQM gives the relationship between the actuator vertical displacement and the voltage applied to the actuator and is defined in Eq. 3.1. In this case, the offset is assumed to be equal to zero and the relationship can be simply written as

$$Displacement = \alpha \times Voltage^2 \tag{4.17}$$

with α a constant.

For the performance evaluation of the SQM, α is optimized using the MCMC algorithm with the set of ten phase screens used for our model performance evaluation.

It is important to note, in Tab. 4.6, that the values presented for *Mod1*, *Mod2* and SQM, under "Desired phase" (PV and rms), "Error rms", "$R_{rms/PV}$", and "$R_{rms/rms}$" are, each, the mean value over the sample of phase maps under test. Therefore, the values indicated under "$R_{rms/PV}$" are not the ratio of the values indicated under "Er-

ror rms" and the values indicated under "Desired phase" (PV), but instead, for each phase map under test, the $R_{rms/PV}$ value has been computed and the mean value of these $R_{rms/PV}$ values is indicated.

Authors	Phase type	Desired phase PV (nm)	Desired phase rms (nm)	Error rms (nm)	$R_{rms/PV}$ (%)	$R_{rms/rms}$ (%)
SQM	Kolmogorov	1448.3	489.5	47.5	6.6	32.2
Morzinski	Kolmogorov	480	—	16	3.33	—
Guzmán	Random	1320.8	320.0	40.6	3.07	12.68
Mod1	Kolmogorov	550	97	16.52	1.96	11.14
Mod2	Kolmogorov	1448.3	489.5	16.8	2.3	11.5

Table 4.6: *Model performance comparison. Values for Mod2 and SQM are the mean value over the ten phase screens under test.*

Tab. 4.6 shows that *Mod2* allows improvement of the DM control performance by approximately a factor three compared with the SQM.

Because the phase maps used for the evaluation of *Mod1* and *Mod2* are different (with the turbulence used for *Mod2*, being approximately three times stronger than the turbulence used for *Mod1*), a quantitative comparison between the two models performance cannot be established. However, the values obtained for $R_{rms/PV}$ and $R_{rms/rms}$ suggests that *Mod2* performs better than *Mod1*, as it provides a similar level of compensation than *Mod1*, which was compensating for a weaker turbulence.

4.5 Chapter conclusion

A new model, *Mod2*, allowing the accurate open-loop control of MEMS DMs, is presented. The model structure permits real-time utilization in an ExAO system. It must be coupled with an iterative process, which inputs a set of voltages and, after few iterations, outputs the phase map produced by the DM.

The model is flexible and allows changes to the parameters without requiring new algorithms to be developed. It allows quick determination of which parameters matter through trial and error. Therefore, the approach can be readily adapted to other

continuous membrane DM technologies. For example, one could replace the electrostatic force equation by the magnetic force equation for a magnetic motion driven DM.

It is critical to match the model to a specific DM and its associated optical setup. Therefore, a set of DM and geometrical parameters must be optimized. These parameters greatly influence the model performance, because they are part of the three force equations used to simulate the active forces during operation. To accurately estimate the values for the model parameters, a Markov Chain Monte Carlo algorithm is used during a preliminary optimization step. This modelling approach is fast because it does not need the use of intensive computational equations, such as the plate theory equation previously proposed for that purpose.

The first laboratory demonstration shows promising performance with **2.3**% residual rms error (for the "rms error/PV" FOM) and **11.5**% residual rms error (for the "rms/rms" FOM), corresponding to the mean values obtained over a set of ten phase screens with a mean PV of 1448 nm. This performance corresponds to an improvement of a factor three compared with the standard quadratic model (common relationship between the voltage sent and the actuator vertical displacement).

Chapter 5

Implementation of *Mod2* within the SCExAO wavefront control system

5.1 Chapter Introduction

Accurate OL control of a DM is particularly critical for the wavefront control of ExAO systems, such as SCExAO, which performs speckle control from the focal plane, using DM motions as a wavefront sensor. Once combined to a high efficiency coronagraph, the ExAO system can create a dark hole area free of most slow and quasi-static speckles and, therefore, open a new path toward direct detection and imaging of faint companions orbiting close to their primary star.

The SCExAO wavefront control system uses a 1024-actuator MEMS DM controlled in OL to measure and modulate speckles complex amplitude in order to distinguish: (i) speckles composed of starlight and due to static and slow-varying residual aberrations and (ii) genuine structures, such as exoplanets, which look like speckles.

Chap. 4 introduced *Mod2* and presented the first laboratory result (performance evaluated in the pupil plane) for a 1024-actuator MEMS DM. *Mod2* has been integrated within the SCExAO wavefront control software and this chapter reports *Mod2* performance in intensity when focal plan speckles are created. The decrease in speckle intensity occurring at high spatial frequencies is a common sign that the DM model

does not properly account for inter-actuator mechanical coupling. We show that using *Mod2* significantly mitigates this issue.

5.2 Implementing *Mod2* within SCExAO wavefront control system

During the implementation of the model within the SCExAO software system, the control software has been modified to allow the user to easily switch between DM command options. The DM can now be driven using either

- a basic quadratic model in which the actuator motion simply follows the quadratic relationship between the voltage applied and the actuator stroke. In the following, we will refer to this model as the SQM, for Standard Quadratic Model
- *Mod2*, which drives the actuators motion by taking into account the forces in action during DM operation and the mechanical coupling between neighbouring actuators.

The model parameter optimization is now performed with the DM directly mounted within the SCExAO bench. No interferometer was available to perform the wavefront measurements and instead the FPWFS is used to perform phase diversity and recover the phase information. Note that the phase diversity was using zonal reconstruction. This wavefront measurement technique uses intensity informations gathered in several planes located around the focal plane to retrieve the phase information. It is important to note that phase diversity measurement is not as precise as interferometer measurement. The optical elements of the bench (DM, lenses, PIAA, filter wheel, WFS cameras, etc.) can be controlled remotely through motorized stages. The SCExAO control computer is equipped with 16 processors and manages, simultaneously, the optics motion, WFS cameras operation and control of the various algorithms dedicated to drive the SCExAO components.

During the implementation efforts have also been focused on increasing the algorithm execution speed. For example, many “if/else” test loops have been replaced by

more efficient sections of code. Several lagging functions have also been rewritten.

Timing functions have been used to evaluate which sections of the model, within the iterative algorithm, were most time consuming. The phase map interpolation, which is the final operation, appeared to be the main lagging section. In order to minimise the computation time spent during the interpolation section, an openMP procedure has been added to the algorithm. For computers equipped with several processors, OpenMP is a multi-platform application, which provides an optimized sharing of the tasks (named threads) and memory available among the different processors. Therefore, using openMP results in an increased execution speed.

Before the implementation of the various code modifications described above, the time initially necessary to run 30 iterations of the MCMC optimization (with each MCMC iteration using several instance of the iterative algorithm) was 26.8 sec. This time moved down to 6.03 sec and the time necessary to run one iteration of the model itself is in the order of 1 ms.

The MCMC algorithm was also modified to optimize, separately, the DM parameters and geometrical parameters. Before this re-organisation, all model parameters were optimized simultaneously. This separation is possible because the set of geometrical parameters is not coupled to the set of physical parameters.

The separation allows the optimization to converge more rapidly (the convergence rate increases when the number of degree of freedom decreases). The MCMC is a more effective optimization approach than an exhaustive search, but as an example, we assume an exhaustive search is being performed on a similar set of DM and geometrical parameters for a search area defined over 100 sample points. When all model parameters are optimized simultaneously, the size of the search space is $100^{15} \backsim 10^{30}$. When the DM and geometrical parameters are optimized independently, the size of the search space becomes $100^7 + 100^8 \backsim 10^{16}$.

In order to improve the efficiency of optimizing the geometrical parameters, additional geometrical volt maps have been generated. These new “geometrical” volt maps have sharp vertical, horizontal, and diagonal features dedicated to easing the determination of rotations, shifts, and scaling properties measured in the resulting

phase maps. The voltage values along the geometrical features vary in order to contribute to the determination of the DM parameters.

The MCMC optimization is now conducted with a set of volt maps combining several Kolmogorov maps (already used for the optimization described in Chap. 4) with several geometrical maps. Four representative volt maps are shown in Fig. 5.1. Both images on the left side show Kolmogorov type volt maps. Both images on the right show geometrical volt maps. For each of the four images, the x- and y-axis represent the actuator array and the vertical color bar is in volts.

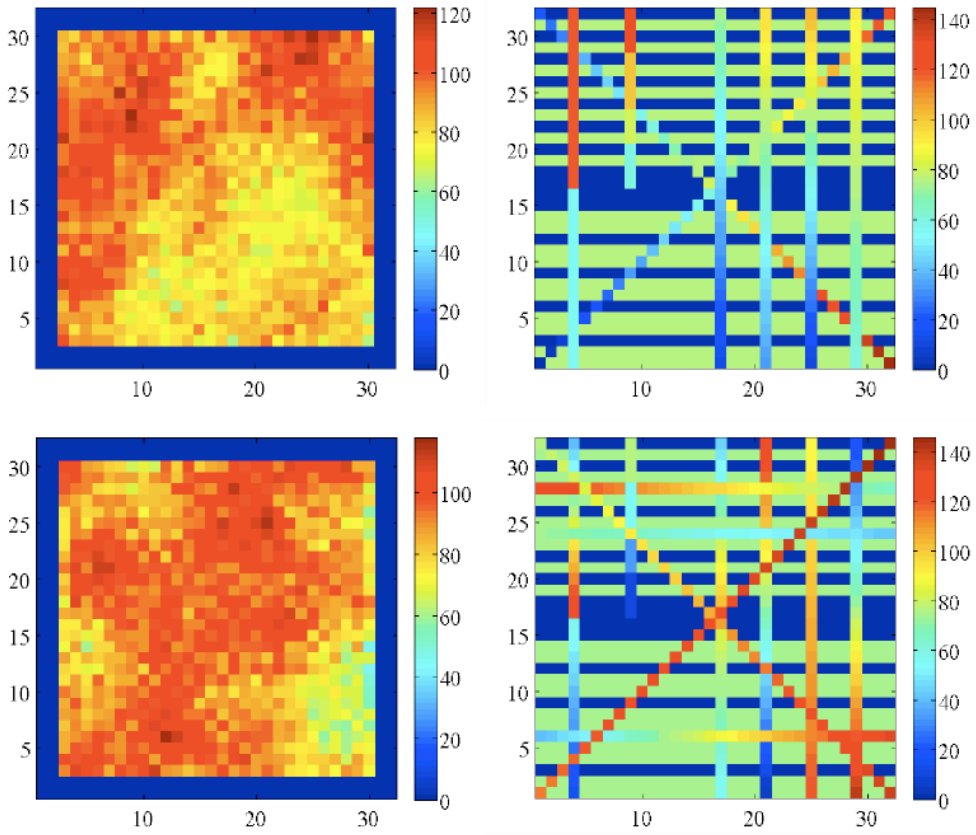

Figure 5.1: *Sample of volt maps used to run the MCMC optimization of the model parameters.*

The expression of the model parameters k_m and k_r, involved in the equations describing the inter-actuator mechanical coupling force and the actuator top plate restoring force (Eq. 4.7 and Eq. 4.8), respectively, have been modified to allow for a better understanding of the parameter physical meaning.

Eq. 4.11 and Eq. 4.12 become,

$$\begin{aligned} k_r &= k_{ra}\left[1+\frac{k_{rb}.dp_0}{k_{ra}}\left(\frac{dp}{dp_0}\right)+\frac{k_{rc}.{dp_0}^2}{k_{ra}}\left(\frac{dp}{dp_0}\right)^2\right] \\ &= \alpha_r\left[1+\beta_r\left(\frac{dp}{dp_0}\right)+\gamma_r\left(\frac{dp}{dp_0}\right)^2\right] \end{aligned} \tag{5.1}$$

$$\begin{aligned} k_m &= k_{ma}\left[1+\frac{k_{mb}.dp_0}{k_{ma}}\left(\frac{\Delta dp}{dp_0}\right)+\frac{k_{mc}.{dp_0}^2}{k_{ma}}\left(\frac{\Delta dp}{dp_0}\right)^2\right] \\ &= \alpha_m\left[1+\beta_m\left(\frac{\Delta dp}{dp_0}\right)+\gamma_m\left(\frac{\Delta dp}{dp_0}\right)^2\right] \end{aligned} \tag{5.2}$$

where β_r, γ_r, β_m and γ_m are corrective non-dimensional terms.

The normalising factor dp_0 equals 1 μm and is associated with the k_r and k_m parameters. With this value of 1 μm, the values of the four corrective terms should be found ≤ 1 and, therefore, the normalising factor is introduced to easily detect, if the optimization has converged toward non-physical values of the corrective terms.

New data processing functions have been added to the MCMC algorithm in order to properly interpret the phase measurements obtained with the phase diversity. The phase diversity outputs phase measurements, which do not contain any tip-tilt and focus components. To ensure that such components do not compromise the comparison of the measured phase and the modelled phase, a function is dedicated to remove the tip-tilt and focus modes in both sets of images.

Another function was dedicated to filtering the measurement noise contained in the phase diversity outputs (using convolution with a Gaussian kernel). Because the measurement noise remains high, even after adding this filter, it became necessary to take the mean value of several (~ 10) realisations of a given phase measurement. Reducing the measurement noise on the measured phase maps is critical to ensure the MCMC optimization converges toward accurate values for the model parameters. The

measurement noise over one measurement was evaluated as 0.13 radians rms. When taking the mean value over 10 realisations, the measurement noise was reduced to $0.13/\sqrt{10} \sim 0.043$ radians rms.

Fig. 5.2 presents typical images of the wavefront measurement obtained with the FPWFS using phase diversity. The left image is the phase obtained when driving the DM with a Kolmogorov volt map. The right image corresponds to the phase obtained when driving the DM with a geometrical volt map. In the image on the right, a mask is added in the data processing to remove actuators outside (not illuminated), or at the very edge (poorly illuminated) of the pupil.

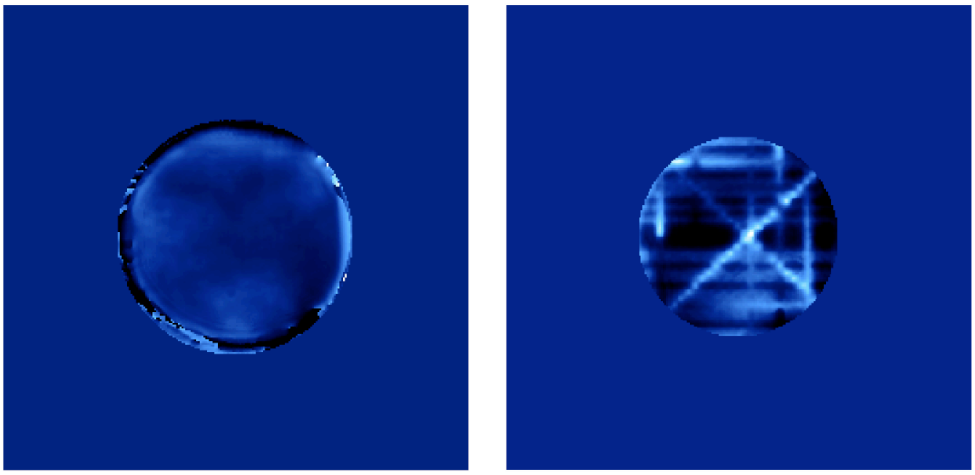

Figure 5.2: *Samples of wavefront measurements obtained with the FPWFS using phase diversity.*

Finally, the convergence of the iterative algorithm output (the value of the actuator displacements $dp(i,j)$), in function of the number of iterations performed within the iterative algorithm, was studied. A geometrical volt map was input into the algorithm. The displacements of 25 sample actuators, selected among the actuator array, was monitored when the algorithm iterates 50 times through Steps 1 to Step 5 (described in Sec. 4.2.4). The range of voltages applied to the sample actuators varied from 6 V to 145 V. The plots presented in Fig. 5.3 shows that the actuator displacement $dp(i,j)$ needs more iterations to converge toward a stable value when the voltage applied is high. All actuators driven under low- to mid-voltage values reach a stable position in less that 10 iterations.

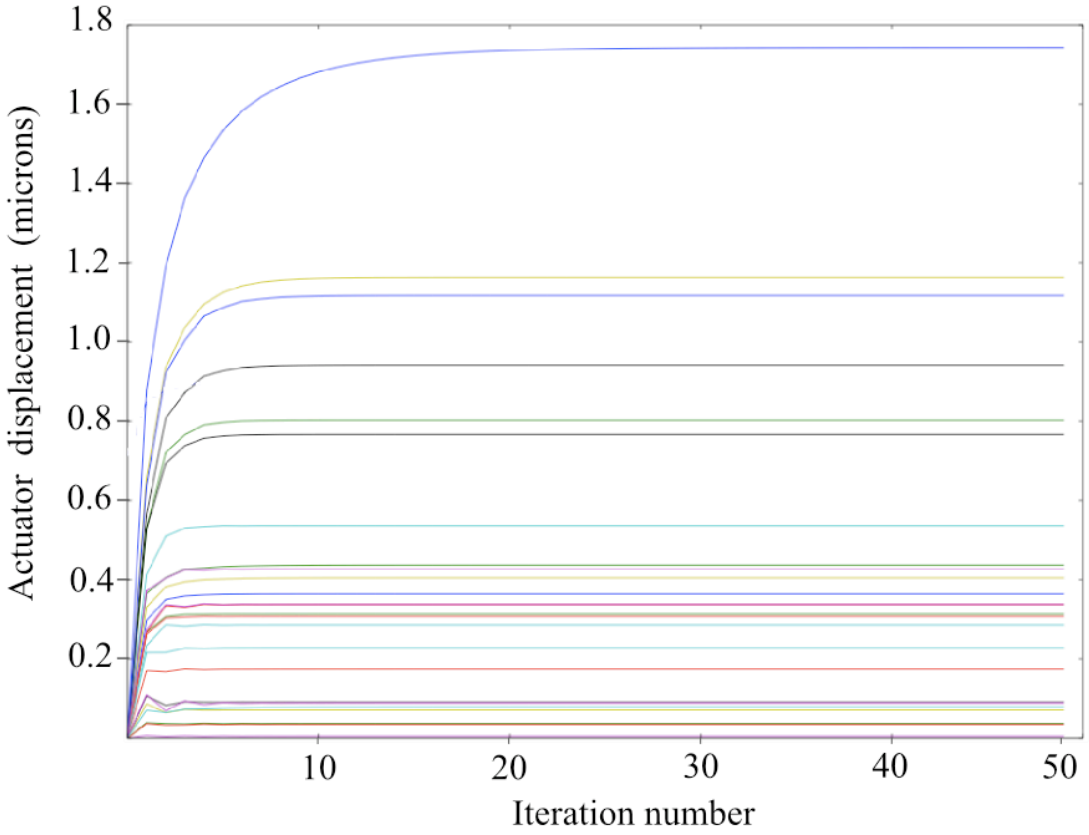

Figure 5.3: *Convergence of the actuator displacement value over 50 iterations.*

Note that in a closed-loop AO system, the variation of actuator displacement from one round of correction to another is small. After the first round of wavefront correction, the wavefront residual is small and the correction applied to each actuator by the feedback is minimal. The results presented in Fig. 5.3 suggests that using *Mod2* within an iterative algorithm for a closed-loop system could greatly increase the system operating speed. With *Mod2*, after 6 iterations, the displacement change reaches 99% of the final displacement (obtained after $\gg 6$ iterations). This is a great advantage over modelling approaches that use plate theory and computationally intense mathematical tools.

5.3 DM command for wavefront sensing and wavefront correction

Ultimately, *Mod2* will be used in the wavefront control system of SCExAO to command the DM when performing speckle nulling. This test has not been performed yet (the current speckle nulling test runs using the SQM to command the DM). However, the following section is devoted to describe how the DM is used in SCExAO to perform both wavefront sensing and wavefront correction.

The light of a residual speckle, due to atmospheric or non common-path error aberrations, is coherent with the starlight. The light coming from a planet, however, creates a speckle-like structure on the image, which is incoherent with the starlight. Unfortunately, residual speckles and planet light signatures are visually indistinguishable in the detector image. To differentiate a real planet from a residual speckle, one can use techniques like speckle nulling or focal plane coherent light modulation, which are all developed around a common approach: a DM located upstream of the coronagraph can be used to modulate speckles. Indeed, a pair of "DM-generated" speckles, symmetrically positioned around the central peak, can be created in the focal plane by adding a sine wave pattern to the DM.

Eq. 1.1 describes the pupil plane complex amplitude. A sine wave on the pupil will create 2 symmetric images of the central PSF[36]:

$$I(\overrightarrow{\alpha}) = PSF(\overrightarrow{\alpha}) \; + \; \left(\frac{\pi h}{\lambda}\right)^2 \; \left[PSF(\overrightarrow{\alpha} + \overrightarrow{f}\,\lambda) + PSF(\overrightarrow{\alpha} - \overrightarrow{f}\,\lambda)\right] \tag{5.3}$$

where λ is the imaging wavelength, $h \ll \lambda$ is the amplitude (in meter) of the sine wave phase aberration of spatial frequency $\overrightarrow{f}$, and $\overrightarrow{\alpha}$ is the angular coordinate on the sky.

DM-generated speckles can thus be superimposed on the existing speckles.

Fig. 5.4 illustrates how sine waves applied to the DM (top three images) result in symmetrical speckles in the focal plane (bottom three images). All sine patterns have the same amplitude (0.6 radians) and phase (0.0 radians). The spatial frequencies in

x and y (given in $actuator^{-1}$) varies, to show the correspondence between the speckles radial position and the spatial frequency.

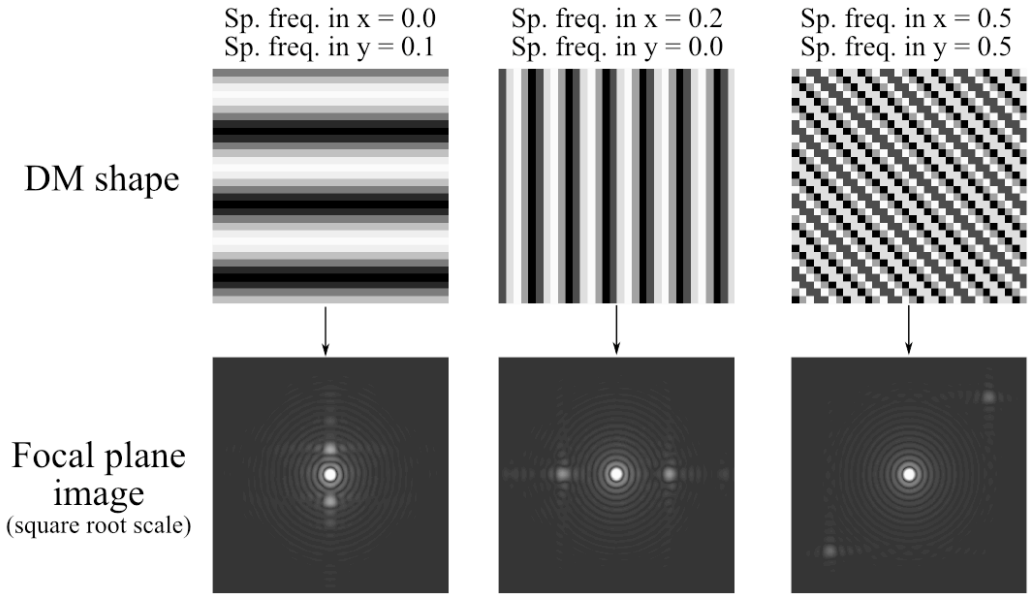

Figure 5.4: *Sample sine wave patterns applied to the DM (top images) and their corresponding simulated focal plane images (bottom images).*

If a DM-generated speckle (with the proper amplitude and a phase shift of π) is superimposed on a speckle composed of starlight, they both have the same coherence property and, as a result, can interfere destructively. If a DM-generated speckle is superimposed on a genuine structure (a planet), the two elements are incoherent and the planet light cannot be cancelled by the DM-generated speckle.

Assuming an accurate control of the DM, the properties of the DM-generated speckle can thus be controlled with great accuracy: the speckle intensity is proportional to the squared value of the sine wave amplitude, the spatial frequency, and orientation of the sine wave pattern defines the speckle location in the image and the sine wave phase encodes the speckle phase. A complex amplitude field can thus be added in the focal plane by linearly decomposing the field into a sum of speckles and by adding the corresponding sum of sine waves to the DM.

This technique, implemented in SCExAO, requires an extreme level of precision in the measure and control of the wavefront. Unlike classical adaptive optics applica-

tions, where the DM is used only to correct the wavefront aberrations, this particular mode of SCExAO employs the DM to perform both the wavefront sensing and the wavefront correction in the focal plane.

5.3.1 DM as a "speckle sensor"

A sine wave shape applied to the DM will create a pair of speckles of given intensity, spatial frequency, and phase in the focal plane. When a focal plane image is acquired, the information regarding the intensity and spatial frequencies of the existing speckles is directly encoded in the image, but the phase information must be indirectly recovered. To recover the phase information for a given speckle in the image, the following speckle sensing procedure, is used (this code was implemented by F. Matinache):

(i) A reference image (without DM-generated speckle) is recorded

(ii) The DM is driven to create sequencially, (a) a horizontal pair of speckles (the spatial frequency is user-defined), (b) a vertical pair of speckles, and (c) linear combination of (a) and (b).

(iii) The reference image is subtracted from the images obtained in (a), (b), and (c) in order to measure the x and y position of the created speckles in the image. The knowledge of the speckles position allows the establishment of a look up table between the spatial frequency and the speckle position in the image. The intensity is obtained directly in the image measurement.

(iv) The phase and amplitude must be determined indirectly. This information can be obtained by first adding a DM-generated speckle at the location of the speckle to be sensed. This DM-generated speckle must have the same intensity and a known phase equal to zero. The corresponding image is acquired (image i_1)

(v) Step (iv) is repeated three other times with phases equal to $\pi/2$, π, and $3\pi/2$, and images are acquired for each case (images i_2, i_3, i_4)

(vi) The four images (i_1, i_2, i_3, i_4) are used to compute the amplitude and phase characteristic of the original speckle. For image i_1, the intensity is $I(i_1) = |A_{dm}e^{i0} + A_{sp}e^{i\phi_{sp}}|^2$, with A_{dm} the known amplitude of the DM-generated speckle

and A_{sp} and ϕ_{sp} the unknown amplitude and phase of the speckle to be sensed. For image i_2, the intensity is $I(i_2) = |A_{dm}e^{i\pi/2} + A_{sp}e^{i\phi_{sp}}|^2$ and so on. With this system of four equations with two unknowns, A_{sp} and ϕ_{sp} can be determined.

This process can be run simultaneously on several speckles, because the creation of a speckle at a given spacial frequency does not affect the creation of additional speckles at other spatial frequencies.

It is important to note that *Mod2* enables to transform a volt map into a displacement map (the DM final shape). In the cases of (i) the DM used for wavefront sensing purpose, (ii) the DM used as wavefront corrector or (iii) the DM used for the speckle nulling process, the **inverse operation** must actually be done. One wants to transform a displacement map into a volt map. An additional routine, which uses and iteratively inverses *Mod2* has thus been included in the DM command process of SCExAO (developed by O. Guyon).

However, this routine was not necessary for the previous evaluations of the model performance in open-loop (described in Sec. 3.2.2 and 4.4). Indeed, for these previous tests, several voltages maps were both (i) sent to the DM and (ii) used as input to the model. The resulting wavefront measurements (measured phase) and model outputs (modelled phase) were then compared. The residual error between measured and modelled phases was used to evaluate the model performance. In this case, the transformation from a voltage map into a displacement map was the only necessary step, no inverse transformation of a phase map into a voltage map was involved.

5.3.2 DM as a "speckle corrector"

Once the phase property of the speckles of interest has been established, the DM shape, necessary to superimpose DM-generated speckles and cancel the focal plane speckles, is computed and projected onto the DM. Each speckle in the science image is treated with this process in order to create the dark hole area region and reach the highest possible contrast.

The iterative speckle nulling control loop has been tested on SCExAO (using the SQM for the DM command) and the result of a series of 50 speckle nulling iterations,

working on up to 10 speckles at a time, is presented in [58]. Future experiments will be dedicated to reproduce this speckle nulling control using *Mod2*.

5.4 Evaluation of the intensity of DM-generated speckles

The *Mod2* model parameters have been estimated within the SCExAO bench setup using the MCMC optimization. The optimum values (and their units, if applicable) are shown in Tab. 5.1.

DM parameters	Geometrical parameters
k_e = -3.25e-18 ± 4.5e-19 [F.m]	Rotation = 1.56 ± 0.01 [rad]
α_r = -1374.8 ± 96.1 [N.m^{-1}]	Projection angle = 0.91 ± 0.002 [ratio]
β_r = 0.39 ± 0.02 [-]	Pixel scale = 0.00016116 ± 1.34e-6 [m.px^{-1}]
γ_r = 0.08 ± 0.02 [-]	Actuator size = 0.00062427 ± 5.22e-6 [m]
α_m = -175.10 ± 42.6 [N.m^{-1}]	Shift in x = 0.0008469 ± 4.97e-5 [m]
β_m = 0.033 ± 0.01 [-]	Shift in y = 8.858e-6 ± 7.22e-7 [m]
γ_m = -0.09 ± 0.02 [-]	Gaussian FWHM = 0.00045684 ± 6e-6 [m]
k_l = 0.80 ± 0.05 [-]	

Table 5.1: *Model parameters for the SCExAO MEMS DM.*

Note, the DM is modelled in the pupil plane of SCExAO, but is actually located in a diverging beam ahead of the pupil. As a result, SCExAO sees a bigger DM than it physically is. This impacts the parameter related to the actuator size: the DM actuators physically measure approximately 300 μm, but once optimized, this value is approximately 600 μm.

Our test consists of creating a pair of DM-generated speckles in the focal plane by applying a sine wave to the DM. The performance of *Mod2* is estimated by comparing the intensity (measured in detector counts) of the DM-generated speckles when three different models are used to command the DM:

- *Mod2*

- the SQM

- a theoretical model, which will be called FMCM, for Free Mechanical Coupling Model.

Unlike the images for *Mod2* and the SQM, measured on the bench by the FPWFS, the images for the FMCM are obtained by numerical simulations (free of measurement noise). The FMCM simulates a *perfect* model for which the coupling between neighbouring actuator is accounted for. To create this model, sine shapes are created (of size 32 by 32 actuators) and an interpolation process is used to transform these displacement maps into phase maps. Fourier transforms are then used to create the resulting focal plane images. It is important to note that the interpolation process assumes perfect additivity of overlapping actuator influence functions but does take into account other coupling effects between actuators. This coupling is responsible for the intensity decrease observed when the spatial frequency increase (see the purple continuous plot in Fig. 5.7).

For each of these three modelling approaches, the DM-generated speckles are created following a similar process:

- The sine wave amplitude is set at 0.5 radians at 1.6 μm

- Each image Im_{sum} is obtained by taking the mean value of four images, with the speckle phase being changed between the 4 images.
  This process is performed in order to cancel interferences that would be generated in the eventuality that a speckle would already exist at the location of the DM-generated speckle. To illustrate, assume that a speckle Sp_1 (of complex amplitude $A_1 e^{i\phi_1}$) is already present at the location in the focal plane where one wants to add a DM-generated speckle Sp_2 (of complex amplitude $A_2 e^{i\phi_2}$). If only one image is acquired, the intensity measured (the squared modulus of the sum of the speckle complex amplitude) will be a combination of Sp_1, Sp_2, and their interference term. Taking the mean value of four images, in which the DM-generated speckle phase Sp_2 is, respectively, ϕ_2, $\phi_2 + \pi/2$, $\phi_2 + \pi$, and $\phi_2 + 3\pi/2$, allows to cancel the interference term. With this phase rotation, the intensity measurement in Im_{sum} now only accounts for Sp_1 and Sp_2. By

subtracting a reference image (containing Sp_1 but not Sp_2) to Im_{sum}, one can deduce the intensity of Sp_2

- The speckles are created along the horizontal axis only, so the y spatial frequency is always equal to 0, while the x spatial frequency varies from 0.1 $actuator^{-1}$ to 0.475 $actuator^{-1}$ by incrementing steps of 0.025 $actuator^{-1}$.

The unit used here is $1/period$ (with the period given in actuator units). The spatial frequency is usually given in cycle per aperture (CPA) units, which is the number of periods (cycles) per beam diameter. The DM is horizontally tilted in the beam ($-24°$). As a result, the density of actuators is not the same in the horizontal and vertical directions and, instead of illuminating all 32 available actuators across the pupil diameter, the beam spreads over a 27.2 x 24.8 actuator ellipse[58]. Thus, 0.1 $actuator^{-1}$ given in 1/period unit corresponds to 10 actuators across the period. With 27.2 actuators across the beam, this corresponds to a 2.72 CPA.

Fig. 5.5 shows four examples of the focal plane images obtained with the three models for spatial frequencies of 0.1, 0.2, 0.3 and 0.4 $actuator^{-1}$ (respectively $\sim$ 2.72, 5.44, 8.16 and 10.88 CPA). It should be noted that SCExAO is equipped with a removable pupil mask engraved to simulate the spider arms supporting the secondary mirror. *Mod2* and the SQM images have been acquired with the pupil mask in place. As a result, faint diffraction patterns created by the spider arms are also visible in both sets of images.

The spatial frequencies in x and y encode the radial position of the two speckles relative to the central peak. The speckles move away from the central peak as the spatial frequency increases (see Fig. 5.4). The highest spatial frequency (in the Nyquist sense) that can be applied to the DM without creating aliasing effects is thus constrained by the number of actuators along the pupil diameter. This maximum spatial frequency of 0.5 $actuator^{-1}$ corresponds to a sine wave with one row (or column) of actuators up and one row (or column) of actuators down (see Fig. 5.6).

The maximum spatial frequency has a direct impact on the variation of speckle intensity versus spatial frequency. Theoretically, when simulating the FMCM, we expect the maximum speckle intensity to be obtained at the smallest spatial frequency and decrease by a factor of two by the time the highest spatial frequency is reached.

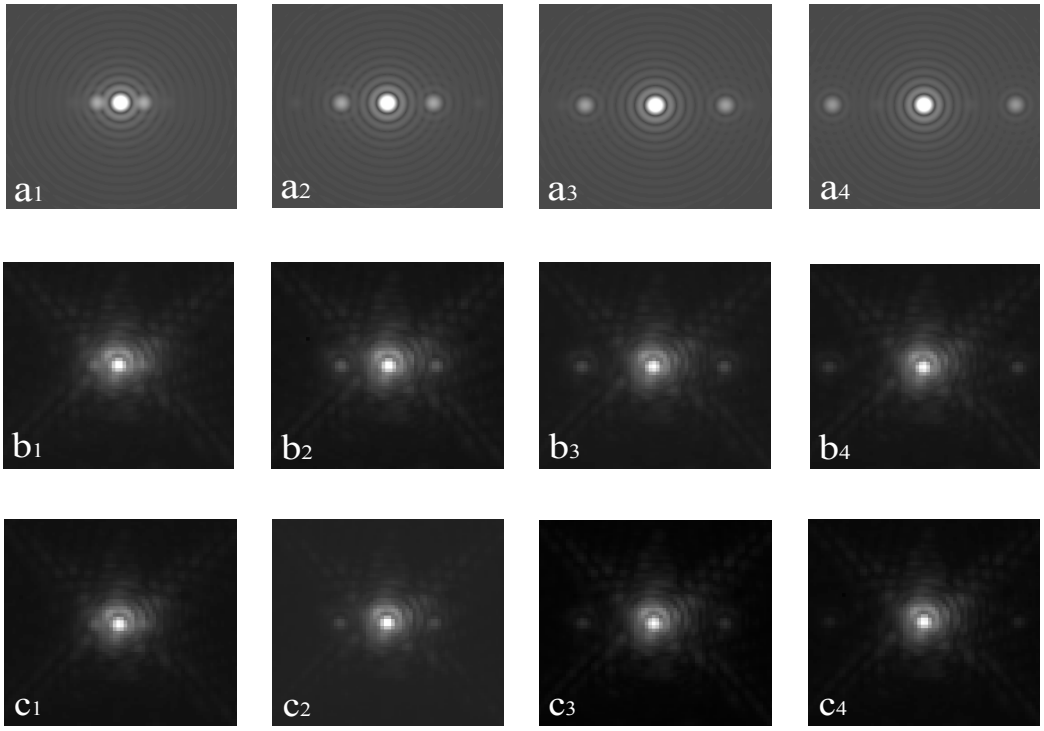

Figure 5.5: *Focal plane images of the DM-generated speckles for spatial frequencies of 0.1, 0.2, 0.3 and 0.4 actuator*$^{-1}$ *for the FMCM (simulated images* a_1 *to* a_4*), for Mod2 (experimental images* b_1 *to* b_4*) and for the SQM (experimental images* c_1 *to* c_4*). The images are displayed with a square root scale to emphasize the speckles and Airy patterns visibility.*

This reduction in intensity is due to the fact that at 0.5 *actuator*$^{-1}$, only half of the four images have a sine pattern. Indeed, at phase $\pi/2$ and $3\pi/2$, the sine wave projected onto the actuator array results in a flat DM and, therefore, no speckle is created in the focal plane image (see Fig. 5.6).

This effect is verified in Fig. 5.7, which presents the comparative plots of speckle intensity versus speckle spatial frequency obtained with *Mod2*, the SQM, and the FMCM. The factor of two decrease for the FMCM is confirmed and the plots show that (i) compared with the SQM, *Mod2* provides a higher speckle intensity at all spatial frequency and (ii) *Mod2* is a better match to the FMCM than the SQM. The oscillation of the plot for *Mod2*, at low spatial frequencies, is due to measurement noise. We note the values plotted in Fig. 5.7 have been obtained by subtracting a reference image (containing no speckle) from each image. In this figure, one can see that even tough Mod2 provides better results than the SQM, the intensity variation

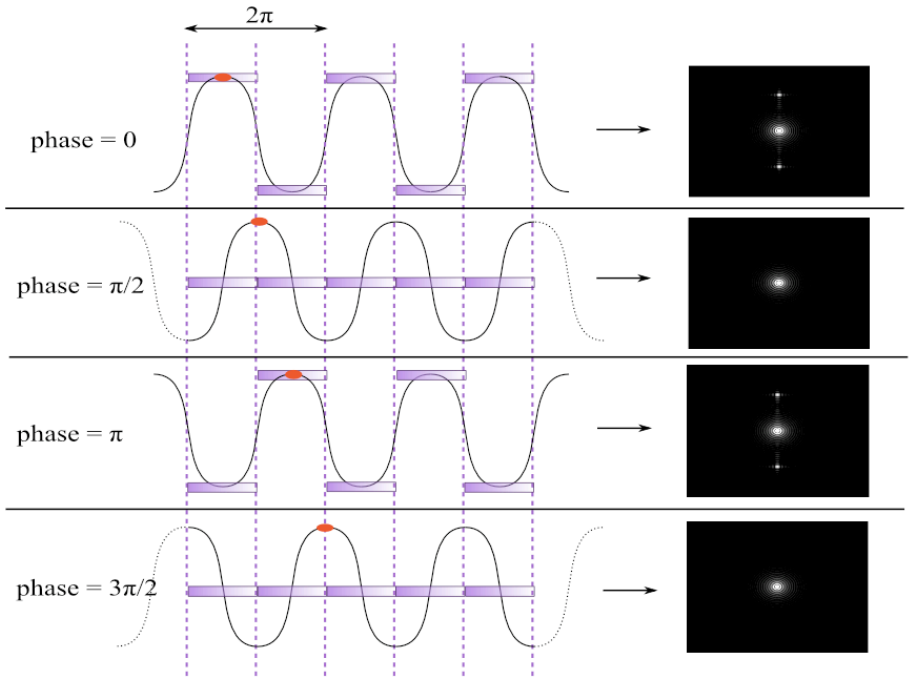

Figure 5.6: *Schematic of the effect of applying a sine wave of spatial frequency equal to 0.5 actuator*$^{-1}$ *to the DM. The purple rectangles represent the actuators.*

obtained with Mod2 does not perfectly match the intensity variation obtained with the FMCM, indicating that Mod2 does not perfectly compensate for all mechanical coupling effects in the system.

To emphasize the result shown in Fig. 5.7, Fig. 5.8 presents the ratio of speckle intensity of *Mod2* to the FMCM and compares it with the ratio of speckle intensity of the SQM to the FMCM. The dashed plot shows the ratio of speckle intensity of the SQM to the FMCM multiplied by a 1.22 scaling factor (bringing both plots to a common starting point). This rescaling emphasizes how *Mod2* provides a slower rate of decrease in speckle intensity when the spatial frequency increases.

5.5 Chapter conclusion

Mod2 has been implemented in the control software of SCExAO and is used to generate the DM command. This chapter reports progress results regarding the control of speckle intensity generated in the focal plan of SCExAO.

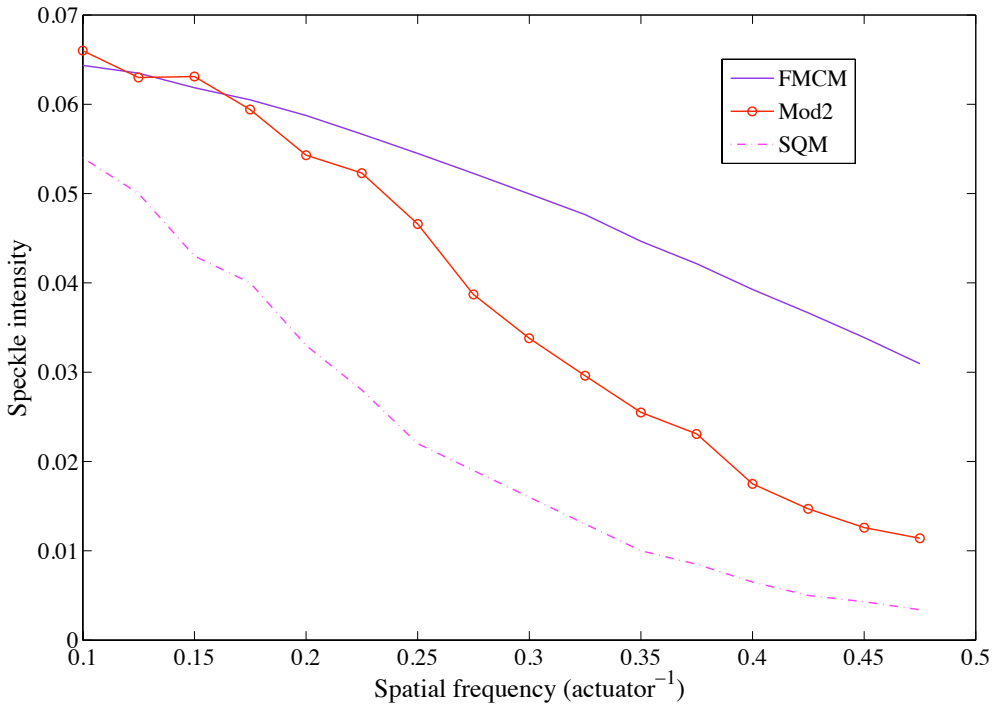

Figure 5.7: *Speckle intensity versus spatial frequency obtained with Mod2, the SQM, and the FMCM models.*

The major advantages of the *Mod2* approach are as follows: when a sine shape of a given amplitude (here 0.5 rad) is projected onto the DM using both the SQM and the *Mod2* models, (i) the speckle intensity obtained, for any spatial frequency, is always higher with *Mod2* (Fig. 5.7) and (ii) the decrease in speckle intensity is lower with *Mod2* (Fig. 5.8).

These two observations suggest that using *Mod2* should improve the system performance for the detection of exoplanets by: (i) reducing of the number of iterations in the speckle control loop and (ii) commensurately increasing the controller frame rate.

Therefore, the *Mod2* approach should help SCExAO to achieve a higher contrast level in the dark hole area and ultimately should increase the ability of SCExAO to detect/image fainter exoplanets.

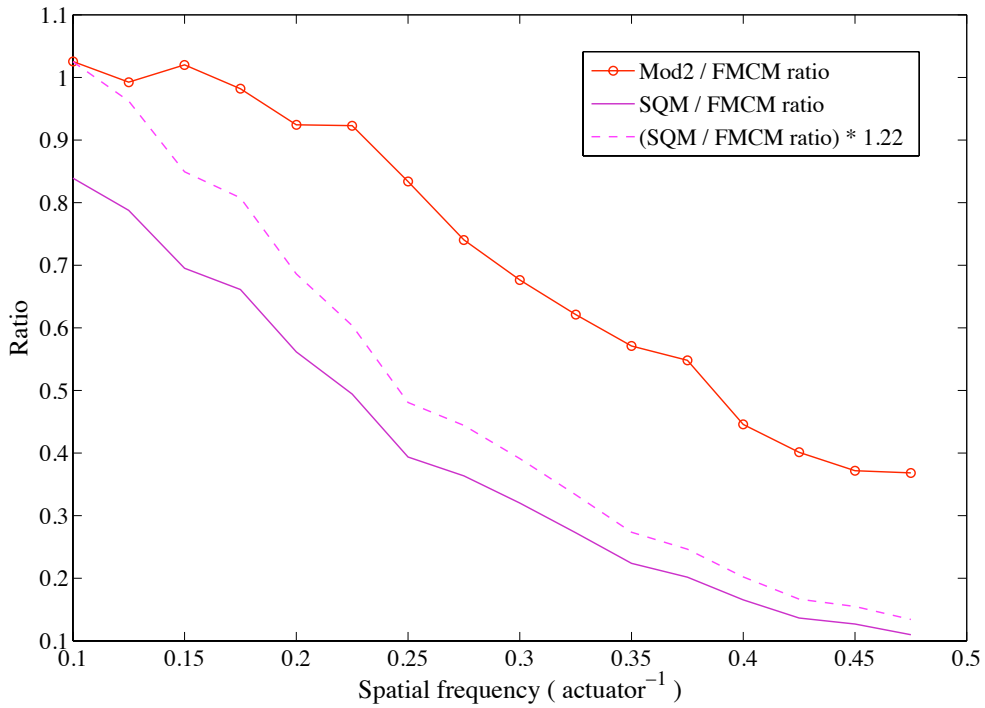

Figure 5.8: *Speckle intensity ratio of Mod2 to FMCM versus the speckle intensity ratio of the SQM to FMCM. The dashed plot shows the speckle intensity ratio of the SQM to FMCM multiplied by a 1.22 scaling factor.*

In the next stage of this work, *Mod2* will be used to command the DM during the speckle nulling process. Contrast in the dark hole area will be compared with the contrast previously obtained when the SQM was used to command the DM. Increasing the iterative algorithm execution speed will also be an important part of the future work, as execution speed is a critical parameter in order to operate the SCExAO system on-sky.

Chapter 6

Conclusion

The accurate open-loop control of MEMS DMs is a critical step toward the successful development of high contrast imaging instruments, such as SCExAO. Accurate open-loop control relies on the development of an accurate DM model.

In this dissertation, two main approaches have been investigated to reach such a goal. The first model, *Mod1*, is based on the experimental calibration of the actuator influence functions. The second model, *Mod2*, is based on the active forces during DM operation and on the characterization of model parameters, which match *Mod2* to both (i) the physical properties of a given MEMS DM, and (ii) the geometrical properties of the optical setup.

The description and development of both models have been reported. The implementation of *Mod2* within the SCExAO wavefront control system is also described. The model's performance in pupil plane and focal plane have been evaluated using a 1024-MEMS DM.

The open-loop performance for the standard quadratic model and for Mod1 are used below to compare with the performance of *Mod2*. This comparison is performed by (i) measuring the shape of the DM when driven with a given volt map and (ii) comparing this shape with the phase map predicted by the different DM command approaches when the same volt map is used as input for the model.

Tab. 6.1 gives the value of the difference (rms) between modelled and measured phase maps for the different DM command approaches. The properties of the volt

maps applied produce Kolmogorov type phase maps once projected onto the DM.

Modelling approach	Experimental setup	Desired phase PV (nm)	Error rms (nm)	$R_{rms/PV}$ (%)
Std. Quad. Model	Interferometer	1448.3	47.5	3.28
Mod1 (with 150 V)	Interferometer	300	11	3.66
Mod1 (with 200 V)	Interferometer	550	16.5	3.00
Mod2	Interferometer	1448.3	16.8	1.16
Mod2 (impl. on SCExAO)	Phase diversity	1448.3	47.2	3.25

Table 6.1: *Performance comparison between the standard quadratic model, Mod1 and Mod2.*

By comparing the performance obtained with *Mod2* using an interferometer and the phase diversity to measure the wavefront, one can see that the quality of the wavefront sensing device greatly impacts the final model performance.

With the experimental setup using the interferometer, the measurement noise is negligible. As a result, the model parameters optimization is able to precisely determine the value of each model parameter, resulting in small residual error rms in the phase maps comparison (modelled versus measured).

With the experimental setup using the phase diversity, even though the data processing has been adapted to minimize the measurement noise (addition of a systematic filtering treatment of the phase diversity output and averaging over several sets of measurements), the calibration of the model parameters is compromised by the residual measurement noise and, therefore, the model performance degrades. The SCExAO team is currently investigating alternatives to remedy this issue.

The advantages of *Mod2* are emphasized in Chap. 5: when a given sine wave shape is projected onto the DM using both the SQM and the *Mod2* models, (i) the speckle intensity obtained, for any spatial frequency, is always higher with *Mod2* and (ii) the decrease in speckle intensity is lower with *Mod2*.

The SCExAO instrument is still going through the engineering testing phase. The first on-sky results were obtained in the summer 2012[21].

In the next stage of this work, *Mod2* will be integrated to the speckle nulling process to evaluate the contrast obtained in the dark hole. The iterative algorithm execution speed remains too slow to efficiently operate on-sky. Therefore, additional code modifications will be performed in the near future, to bring the algorithm up to on-sky speed standards.

Bibliography

[1] J. Schneider, The Extrasolar Planets Encyclopaedia, retrieved on September 2012 from http://exoplanet.eu.

[2] M. Feinberg – Boston Micromachines Corporation, private communication.

[3] S. M. Ammons, L. Johnson, E. A. Laag, R. Kupke, and D. T. Gavel. Laboratory demonstrations of multi-object adaptive optics in the visible on a 10 meter telescope. In *Society of Photo-Optical Instrumentation Engineers (SPIE) Conference Series*, volume 7015 of *Society of Photo-Optical Instrumentation Engineers (SPIE) Conference Series*, July 2008.

[4] D. R. Andersen, S. S. Eikenberry, M. Fletcher, W. Gardhouse, B. Leckie, J.-P. Véran, D. Gavel, R. Clare, R. Guzman, L. Jolissaint, R. Julian, and W. Rambold. The MOAO system of the IRMOS near-infrared multi-object spectrograph for TMT. In *Society of Photo-Optical Instrumentation Engineers (SPIE) Conference Series*, volume 6269 of *Society of Photo-Optical Instrumentation Engineers (SPIE) Conference Series*, July 2006.

[5] D. R. Andersen, M. Fischer, R. Conan, M. Fletcher, and J.-P. Véran. VOLT: the Victoria Open Loop Testbed. In *Society of Photo-Optical Instrumentation Engineers (SPIE) Conference Series*, volume 7015 of *Society of Photo-Optical Instrumentation Engineers (SPIE) Conference Series*, July 2008.

[6] D. R. Andersen, K. J. Jackson, C. Blain, C. Bradley, C. Correia, M. Ito, O. Lardière, and J.-P. Véran. Performance Modeling for the RAVEN Multi-Object Adaptive Optics Demonstrator. *Publications of the Astronomical Society of the Pacific*, 124:469–484, 2012.

[7] H. W. Babcock. The Possibility of Compensating Astronomical Seeing. *Publications of the Astronomical Society of the Pacific*, 65:229, October 1953.

[8] G. J. Baker. A fast high-fidelity model for the deformation of continuous facesheet deformable mirrors. In *Society of Photo-Optical Instrumentation Engineers (SPIE) Conference Series*, volume 6272 of *Society of Photo-Optical Instrumentation Engineers (SPIE) Conference Series*, July 2006.

[9] P. Baudoz, A. Boccaletti, J. Baudrand, and D. Rouan. The Self-Coherent Camera: a new tool for planet detection. In C. Aime and F. Vakili, editors, *IAU Colloq. 200: Direct Imaging of Exoplanets: Science and Techniques*, pages 553–558, 2006.

[10] R. Belikov, E. Pluzhnik, F. C. Witteborn, D. H. Lynch, T. P. Greene, P. T. Zell, K. Balasubramanian, and O. Guyon. PIAA Coronagraph Development at NASA Ames: High Contrast Laboratory Demonstration at 2 l/D. In *American Astronomical Society Meeting Abstracts 217*, volume 43 of *Bulletin of the American Astronomical Society*, page 254.06, January 2011.

[11] T. Bifano, S. Cornelissen, and P. Bierden. MEMS deformable mirrors in astronomical adaptive optics. In *Adaptative Optics for Extremely Large Telescopes*, 2010.

[12] T. G. Bifano, R. Krishnamoorthy Mali, J. K. Dorton, J. Perreault, N. Vandelli, M. N. Horenstein, and D. A. Castanon. Continuous-membrane surface-micromachined silicon deformable mirror. *Optical Engineering*, 36:1354–1360, May 1997.

[13] C. Blain, R. Conan, C. Bradley, O. Guyon, and C. Vogel. Characterisation of the influence function non-additivities for a 1024-actuator MEMS deformable mirror. In *Adaptative Optics for Extremely Large Telescopes*, 2010.

[14] C. Blain, R. Conan, C. Bradley, O. Keskin, P. Hampton, and A. Hilton. Magnetic ALPAO and Piezo-Stack CILAS Deformable Mirrors Characterization . In *Optical Society of America, Proceedings of the Adaptive Optics: Methods, Analysis and Applications conference, Vancouver, BC*, page ATuC6, 2007.

[15] C. Blain, O. Guyon, , C. Bradley, F. Martinache, and C. Clergeon. An iterative model for MEMS deformable mirrors. In *Proceedings of the 2nd Adaptative Optics for Extremely Large Telescopes Conference, Victoria, BC*, 2012.

[16] C. Blain, O. Guyon, C. Bradley, and O. Lardire. Fast iterative algorithm (FIA) for controlling MEMS deformable mirrors: principle and laboratory demonstration. *Optics Express*, 19:21271–21294, 2011.

[17] C. Blain, O. Guyon, C. Rodolphe, and C. Bradley. Simple iterative method for open-loop control of MEMS deformable mirrors. In *Adaptive Optics Systems, Norbert Hubin; Claire E. Max; Peter L. Wizinowich*, volume 701534, 2008.

[18] C. Blain, C. Rodolphe, C. Bradley, and O. Guyon. Open-loop control demonstration of micro-electro-mechanical-system MEMS deformable mirror. *Optics Express*, 18:5433–5448, 2010.

[19] C. Blain, C. Rodolphe, C. Bradley, O. Guyon, D. Gamroth, and R. Nash. Real-time open-loop control of a 1024-actuator MEMS deformable mirror. In *Adaptive Optics Systems II,Brent L. Ellerbroek; Michael Hart; Norbert Hubin; Peter L. Wizinowich*, volume 7736, 2010.

[20] P. J. Bordé and W. A. Traub. High-Contrast Imaging from Space: Speckle Nulling in a Low-Aberration Regime. *Astroph. Journal*, 638:488, February 2006.

[21] C. Clergeon, O. Guyon, and F. Martinache. The Subaru Coronagraphic Extreme AO Project: First On-sky Results. In *American Astronomical Society Meeting Abstracts 219*, volume 219 of *American Astronomical Society Meeting Abstracts*, page 422.12, January 2012.

[22] R. Conan, C. Bradley, O. Lardière, C. Blain, K. Venn, D. Andersen, L. Simard, J.-P. Véran, G. Herriot, D. Loop, T. Usuda, S. Oya, Y. Hayano, H. Terada, and M. Akiyama. Raven: a harbinger of multi-object adaptive optics-based instruments at the Subaru Telescope. In *Society of Photo-Optical Instrumentation Engineers (SPIE) Conference Series*, volume 7736 of *Society of Photo-Optical Instrumentation Engineers (SPIE) Conference Series*, July 2010.

[23] S. A. Cornelissen, A. L. Hartzell, J. B. Stewart, T. G. Bifano, and P. A. Bierden. MEMS deformable mirrors for astronomical adaptive optics. In *Society of Photo-Optical Instrumentation Engineers (SPIE) Conference Series*, volume 7736 of *Society of Photo-Optical Instrumentation Engineers (SPIE) Conference Series*, July 2010.

[24] S. Eikenberry, D. Andersen, R. Guzman, J. Bally, S. Cuevas, M. Fletcher, R. Gardhouse, D. Gavel, A. Gonzalez, N. Gruel, F. Hamann, S. Hamner, R. Julian, J. Julian, D. Koo, E. Lada, B. Leckie, J. A. Lopez, R. Pello, J. Perez, W. Rambold, C. Roman, A. Sarajedini, J. Tan, K. Venn, J.-P. Veran, and J. Ziegert. IRMOS: The near-infrared multi-object spectrograph for the TMT. In *Society of Photo-Optical Instrumentation Engineers (SPIE) Conference Series*, volume 6269 of *Society of Photo-Optical Instrumentation Engineers (SPIE) Conference Series*, July 2006.

[25] J. W. Evans, B. Macintosh, L. Poyneer, K. Morzinski, S. Severson, D. Dillon, D. Gavel, and L. Reza. Demonstrating sub-nm closed loop MEMS flattening. *Optics Express*, 14:5558–5570, June 2006.

[26] J. W. Evans, K. Morzinski, L. Reza, S. Severson, L. Poyneer, B. A. Macintosh, D. Dillon, G. Sommargren, D. Palmer, D. Gavel, and S. Olivier. Extreme adaptive optics testbed: high contrast measurements with a MEMS deformable mirror. In D. R. Coulter, editor, *Society of Photo-Optical Instrumentation Engineers (SPIE) Conference Series*, volume 5905 of *Society of Photo-Optical Instrumentation Engineers (SPIE) Conference Series*, pages 303–310, August 2005.

[27] C. Ftaclas, A. Kellerer, and M. Chun. Advanced Curvature Deformable Mirrors. In *Advanced Maui Optical and Space Surveillance Technologies Conference*, September 2010.

[28] R. Galicher, P. Baudoz, and G. Rousset. Principles, Simulations and Performances of the Self-Coherent Camera. In *In the Spirit of Bernard Lyot: The Direct Detection of Planets and Circumstellar Disks in the 21st Century*, June 2007.

[29] R. Galicher, P. Baudoz, and G. Rousset. Wavefront error correction and Earth-like planet detection by a self-coherent camera in space. *Astronomy and Astrophysics*, 488:L9–L12, September 2008.

[30] R. Galicher, P. Baudoz, G. Rousset, J. Totems, and M. Mas. Self-coherent camera as a focal plane wavefront sensor: simulations. *Astronomy and Astrophysics*, 509:A31, January 2010.

[31] D. Gavel, S. Severson, B. Bauman, D. Dillon, M. Reinig, C. Lockwood, D. Palmer, K. Morzinski, M. Ammons, E. Gates, and B. Grigsby. Villages: an

on-sky visible wavelength astronomy AO experiment using a MEMS deformable mirror. In *Society of Photo-Optical Instrumentation Engineers (SPIE) Conference Series*, volume 6888 of *Society of Photo-Optical Instrumentation Engineers (SPIE) Conference Series*, March 2008.

[32] A. Give'on, B. Kern, S. Shaklan, D. C. Moody, and L. Pueyo. Electric Field Conjugation - A Broadband Wavefront Correction Algorithm For High-contrast Imaging Systems. In *American Astronomical Society Meeting Abstracts*, volume 39 of *Bulletin of the American Astronomical Society*, page 135.20, December 2007.

[33] A. Give'on, S. Shaklan, and B. Kern. Electric Field Conjugation-based Wavefront Correction Algorithm for High Contrast Imaging Systems - Experimental Results. In *In the Spirit of Bernard Lyot: The Direct Detection of Planets and Circumstellar Disks in the 21st Century*, June 2007.

[34] J. W. Goodman. *Speckle Phenomena in Optics: Theory and Applications*. Roberts and Company, Englewood Colorado, 2007.

[35] O. Guyon. Phase-induced amplitude apodization of telescope pupils for extrasolar terrestrial planet imaging. *aap*, 404:379–387, June 2003.

[36] O. Guyon. Limits of Adaptive Optics for High-Contrast Imaging. *Astroph. Journal*, 629:592–614, August 2005.

[37] O. Guyon. High Sensitivity Wavefront Sensing with a Nonlinear Curvature Wavefront Sensor. *Publications of the Astronomical Society of the Pacific*, 122:49–62, January 2010.

[38] O. Guyon, B. Gallet, E. A. Pluzhnik, H. Takami, and M. Tamura. High contrast imaging with focal plane wavefront sensing for ground based telescopes. In *Society of Photo-Optical Instrumentation Engineers (SPIE) Conference Series*, volume 6272 of *Society of Photo-Optical Instrumentation Engineers (SPIE) Conference Series*, July 2006.

[39] O. Guyon, B. Kern, R. Belikov, S. Shaklan, A. Kuhnert, and A. Give'On. Phase-Induced Amplitude Apodization (PIAA) coronagraphy: recent results and future

prospects. In *Society of Photo-Optical Instrumentation Engineers (SPIE) Conference Series*, volume 8151 of *Society of Photo-Optical Instrumentation Engineers (SPIE) Conference Series*, September 2011.

[40] O. Guyon, B. Kern, R. Belikov, S. Shaklan, A. Kuhnert, A. Giveon, F. Martinache, T. Greene, and E. Pluzhnik. High Contrast Imaging With Phase-induced Amplitude Apodization (PIAA). In *American Astronomical Society Meeting Abstracts 219*, volume 219 of *American Astronomical Society Meeting Abstracts*, page 155.15, January 2012.

[41] O. Guyon, F. Martinache, V. Garrel, F. Vogt, K. Yokochi, and T. Yoshikawa. The Subaru coronagraphic extreme AO (SCExAO) system: wavefront control and detection of exoplanets with coherent light modulation in the focal plane. In *Society of Photo-Optical Instrumentation Engineers (SPIE) Conference Series*, volume 7736 of *Society of Photo-Optical Instrumentation Engineers (SPIE) Conference Series*, July 2010.

[42] O. Guyon, F. Martinache, V. Garrel, F. Vogt, K. Yokochi, and T. Yoshikawa. The Subaru coronagraphic extreme AO (SCExAO) system: wavefront control and detection of exoplanets with coherent light modulation in the focal plane. In *Society of Photo-Optical Instrumentation Engineers (SPIE) Conference Series*, volume 7736 of *Society of Photo-Optical Instrumentation Engineers (SPIE) Conference Series*, July 2010.

[43] O. Guyon, T. Matsuo, and R. Angel. Coronagraphic Low-Order Wave-Front Sensor: Principle and Application to a Phase-Induced Amplitude Coronagraph. *Astroph. Journal*, 693:75–84, March 2009.

[44] O. Guyon, E. Pluzhnik, F. Martinache, J. Totems, S. Tanaka, T. Matsuo, C. Blain, and R. Belikov. High-Contrast Imaging and Wavefront Control with a PIAA Coronagraph: Laboratory System Validation. *Publications of the Astronomical Society of the Pacific*, 122:71–84, January 2010.

[45] D. Guzmán, F. J. Juez, F. S. Lasheras, R. Myers, and L. Young. Deformable mirror model for open-loop adaptive optics using multivariate adaptive regression splines. *Optics Express*, 18:6492–6505, 2010.

[46] D. Guzmán, F. J. Juez, R. Myers, A. Guesalaga, and F. S. Lasheras. Modeling a MEMS deformabe mirror using non-parametric estimation techniques. *Optics Express*, 18:21356–21369, 2010.

[47] C. L. Hom, P. D. Dean, and S. R. Winzer. Simulating electrostrictive deformable mirrors: I. Nonlinear static analysis. *Smart Materials and Structures*, 8:691–699, 1999.

[48] B. Kern, O. Guyon, A. Give'On, A. Kuhnert, and A. Niessner. Laboratory testing of a Phase-Induced Amplitude Apodization (PIAA) coronagraph. In *Society of Photo-Optical Instrumentation Engineers (SPIE) Conference Series*, volume 8151 of *Society of Photo-Optical Instrumentation Engineers (SPIE) Conference Series*, September 2011.

[49] L. A. Lisa A. Poyneer, D. Dillon, S. Thomas, and B. A. Macintosh. Laboratory demonstration of accurate and efficient nanometer-level wavefront control for extreme adaptive optics. *Optics Express*, 47:1317–1326, 2008.

[50] B. A. Macintosh, A. Anthony, J. Atwood, N. Barriga, B. Bauman, K. Caputa, J. Chilcote, D. Dillon, R. Doyon, J. Dunn, D. T. Gavel, R. Galvez, S. J. Goodsell, J. R. Graham, M. Hartung, J. Isaacs, D. Kerley, Q. Konopacky, K. Labrie, J. E. Larkin, J. Maire, C. Marois, M. Millar-Blanchaer, A. Nunez, B. R. Oppenheimer, D. W. Palmer, J. Pazder, M. Perrin, L. A. Poyneer, C. Quirez, F. Rantakyro, V. Reshtov, L. Saddlemyer, N. Sadakuni, D. Savransky, A. Sivaramakrishnan, M. Smith, R. Soummer, S. Thomas, J. K. Wallace, J. Weiss, and S. Wiktorowicz. The Gemini Planet Imager: integration and status. In *Society of Photo-Optical Instrumentation Engineers (SPIE) Conference Series*, volume 8446 of *Society of Photo-Optical Instrumentation Engineers (SPIE) Conference Series*, September 2012.

[51] B. A. Macintosh, J. R. Graham, D. W. Palmer, R. Doyon, J. Dunn, D. T. Gavel, J. Larkin, B. Oppenheimer, L. Saddlemyer, A. Sivaramakrishnan, J. K. Wallace, B. Bauman, D. A. Erickson, C. Marois, L. A. Poyneer, and R. Soummer. The Gemini Planet Imager: from science to design to construction. In *Society of Photo-Optical Instrumentation Engineers (SPIE) Conference Series*, volume 7015 of *Society of Photo-Optical Instrumentation Engineers (SPIE) Conference Series*, July 2008.

[52] F. Malbet, J. W. Yu, and M. Shao. High-Dynamic-Range Imaging Using a Deformable Mirror for Space Coronography. *Publications of the Astronomical Society of the Pacific*, 107:386, April 1995.

[53] C. Marois, R. Doyon, D. Nadeau, R. Racine, and G. A. H. Walker. Effects of Quasi-Static Aberrations in Faint Companion Searches. In C. Aime and R. Soummer, editors, *EAS Publications Series*, volume 8 of *EAS Publications Series*, pages 233–243, 2003.

[54] C. Marois, D. Lafrenière, R. Doyon, B. Macintosh, and D. Nadeau. Angular Differential Imaging: A Powerful High-Contrast Imaging Technique. *Astroph. Journal*, 641:556–564, April 2006.

[55] C. Marois, B. Macintosh, T. Barman, B. Zuckerman, I. Song, J. Patience, D. Lafrenière, and R. Doyon. Direct Imaging of Multiple Planets Orbiting the Star HR 8799. *Science*, 322:1348–, November 2008.

[56] C. Marois, B. Zuckerman, Q. M. Konopacky, B. Macintosh, and T. Barman. Images of a fourth planet orbiting HR 8799. *Nature*, 468:1080–1083, December 2010.

[57] F. Martinache and O. Guyon. The Subaru Coronagraphic Extreme AO Project. In V. Coudé Du Foresto, D. M. Gelino, and I. Ribas, editors, *Pathways Towards Habitable Planets*, volume 430 of *Astronomical Society of the Pacific Conference Series*, page 497, October 2010.

[58] F. Martinache, O. Guyon, C. Clergeon, and C. Blain. Speckle Control with a remapped-pupil PIAA-coronagraph. *ArXiv e-prints*, June 2012.

[59] F. Martinache, O. Guyon, V. Garrel, C. Clergeon, T. Groff, P. Stewart, R. Russell, and C. Blain. The Subaru coronagraphic extreme AO project: progress report. In *Society of Photo-Optical Instrumentation Engineers (SPIE) Conference Series*, volume 8151 of *Society of Photo-Optical Instrumentation Engineers (SPIE) Conference Series*, September 2011.

[60] Y. Minowa, Y. Hayano, S. Oya, M. Watanabe, M. Hattori, O. Guyon, S. Egner, Y. Saito, M. Ito, H. Takami, V. Garrel, S. Colley, T. Golota, and M. Iye. Performance of Subaru adaptive optics system AO188. In *Society of Photo-Optical*

Instrumentation Engineers (SPIE) Conference Series, volume 7736 of *Society of Photo-Optical Instrumentation Engineers (SPIE) Conference Series*, July 2010.

[61] K. M. Morzinski, J. W. Evans, S. Severson, B. Macintosh, D. Dillon, D. Gavel, C. Max, and D. Palmer. Characterizing the potential of MEMS deformable mirrors for astronomical adaptive optics. In *Society of Photo-Optical Instrumentation Engineers (SPIE) Conference Series*, volume 6272 of *Society of Photo-Optical Instrumentation Engineers (SPIE) Conference Series*, July 2006.

[62] K. M. Morzinski, D. T. Gavel, A. P. Norton, D. R. Dillon, and M. R. Reinig. Characterizing MEMS deformable mirrors for open-loop operation: high-resolution measurements of thin-plate behavior. In *Society of Photo-Optical Instrumentation Engineers (SPIE) Conference Series*, volume 6888 of *Society of Photo-Optical Instrumentation Engineers (SPIE) Conference Series*, March 2008.

[63] D. Mouillet, J.-L. Beuzit, M. Feldt, K. Dohlen, P. Puget, F. Wildi, A. Boccaletti, T. Henning, C. Moutou, H. M. Schmid, M. Turatto, S. Udry, F. Vakili, R. Waters, A. Baruffolo, J. Charton, R. Claudi, T. Fusco, R. Gratton, N. Hubin, M. Kasper, M. Langlois, J. Pragt, R. Roelfsema, and M. Saisse. SPHERE: A 'Planet Finder' Instrument for the VLT. In A. Moorwood, editor, *Science with the VLT in the ELT Era*, page 337, 2009.

[64] J. A. Perreault, P. A. Bierden, M. N. Horenstein, and T. G. Bifano. Manufacturing of an optical-quality mirror system for adaptive optics. In J. D. Gonglewski, M. A. Vorontsov, and M. T. Gruneisen, editors, *Society of Photo-Optical Instrumentation Engineers (SPIE) Conference Series*, volume 4493 of *Society of Photo-Optical Instrumentation Engineers (SPIE) Conference Series*, pages 13–20, February 2002.

[65] M. A. C. Perryman. *The exoplanet handbook*. Cambridge ; New York : Cambridge University Press, 2011.

[66] S. P. Quanz, H. M. Schmid, K. Geissler, M. R. Meyer, T. Henning, W. Brandner, and S. Wolf. Very Large Telescope/NACO Polarimetric Differential Imaging of HD100546–Disk Structure and Dust Grain Properties between 10 and 140 AU. *Astroph. Journal*, 738:23, September 2011.

[67] G. Rousset, T. Fusco, F. Assemat, E. Gendron, T. Morris, C. Robert, R. Myers, M. Cohen, N. Dipper, C. Evans, D. Gratadour, P. Jagourel, P. Laporte, D. Le Mignant, M. Puech, H. Schnetler, W. Taylor, F. Vidal, J.-G. Cuby, M. Lehnert, S. Morris, and P. Parr-Burman. EAGLE MOAO system conceptual design and related technologies. In *Society of Photo-Optical Instrumentation Engineers (SPIE) Conference Series*, volume 7736 of *Society of Photo-Optical Instrumentation Engineers (SPIE) Conference Series*, July 2010.

[68] W. H. Smith. Spectral differential imaging detection of planets about nearby stars. *Publications of the Astronomical Society of the Pacific*, 99:1344–1353, December 1987.

[69] J. B. Stewart, A. Diouf, Y. Zhou, and T. Bifano. Open-loop control of a MEMS deformable mirror for large-amplitude wavefront control. *J. Opt. Soc. of America, A*, 24:3827–33, 2007.

[70] R. Suzuki, M. Tamura, H. Suto, J.-I. Morino, J. Hashimoto, T. Kudo, R. Kandori, N. Murakami, J. Nishikawa, N. Ukita, H. Takami, O. Guyon, T. Nishimura, M. Hayashi, H. Izumiura, L. Abe, A. Tavrov, S. Jacobson, V. Stahlberger, H. Yamada, R. Shelton, and K. Hodapp. HiCIAO: A High-contrast Instrument for the Next Generation Subaru Adaptive Optics. In T. Usuda, M. Tamura, and M. Ishii, editors, *American Institute of Physics Conference Series*, volume 1158 of *American Institute of Physics Conference Series*, pages 293–298, August 2009.

[71] J. Totems and O. Guyon. High Contrast Tests with a PIAA Coronagraph in Air. In *In the Spirit of Bernard Lyot: The Direct Detection of Planets and Circumstellar Disks in the 21st Century*, page 41, June 2007.

[72] J. T. Trauger and W. A. Traub. A laboratory demonstration of the capability to image an Earth-like extrasolar planet. *Nature*, 446:771–773, April 2007.

[73] C. R. Vogel, G. Tyler, Y. Lu, T. Bifano, R. Conan, and C. Blain. Modeling and parameter estimation for point-actuated continuous-facesheet deformable mirrors. *J. Opt. Soc. of America, A*, 27:A56–63, 2006.

[74] C. R. Vogel and Q. Yang. Modeling, simulation, and open-loop control of a continuous facesheet MEMS deformable mirror. *J. Opt. Soc. of America, A*, 23:1074–1081, 2006.

Appendix A

Typical characterization of a deformable mirror

The results from typical characterization procedures for a piezo-stack DM (CILAS) and a magnetic DM (ALPAO) are presented[14]. The maximum stroke, inter-actuator coupling, linearity, hysteresis, best flat, and shape at rest are measured. The main manufacturer specifications for both DMs are given in Tab. A.1.

Piezo-stack DM	Magnetic DM
57 actuators(9 by 9 grid)	52 actuators (8 by 8 grid)
5 mm actuator pitch	2.5 mm actuator pitch
actuator stroke: 10 μm PV	actuator stroke: up to 25 μm
inter-actuator stroke: 1.9 μm	5nm RMS best flat
inter-actuator coupling: 10-25 %	high linearity
operating temperature: down to -35°C	no hysteresis

Table A.1: *Main properties of the CILAS and ALPAO DMs.*

For each DM, a Zygo PTI 250 interferometer is pointed onto the DM and used to take surface measurements. All measurements are taken at room temperature. In addition, the piezo-stack DM is also tested at 0°C and -35°C. For the tests at 0°C and -35°C, the DM is set inside a small cold chamber (the experimental setup with the cold chamber is shown on Fig. A.1).

The minimum/maximum voltages applied to the DMs during the tests are -0.45/+0.45 V for the magnetic DM and -400/+400 V for the piezo-stack DM.

Figure A.1: *(a) Piezo-stack DM enclosure opened, the electronic connections at the back of the DM are visible. (b) DM set on the mount in front of the interferometer. The cold chamber is visible on the right. (c) Full experimental setup.*

For each DM, the following measurements are taken:

- Maximum stroke of each actuator: each actuators is sequentially pushed to the maximum voltage then pulled to the minimum and both corresponding mirror deformations are saved. The minimum is then subtracted from the maximum during data processing

- Maximum stroke for an array of 3 by 3 actuators: each set of 3 by 3 actuators is sequentially pushed to the maximum voltage then pulled to the minimum voltage and the corresponding mirror deformations are saved. The minimum is then subtracted from the maximum during data processing

- Horizontal, vertical and diagonal inter-actuator stroke: each actuator is sequentially pushed to the maximum voltage while its neighbour (either vertical, horizontal or diagonal) is pulled to the minimum voltage. The reference mirror surface (for all the actuators set to 0 volt) is also saved for each measurement and then subtracted during data processing

- Linearity

- Hysteresis (for the piezo-stack DM only)

- Best flat (for the piezo-stack DM only)

- Shape at rest (for the piezo-stack DM only).

The performance of each actuator is evaluated individually. Ten measurements have been repeated for each actuator. The maximum, minimum, mean, median, and standard deviation are extracted from the 10 measurements.

To illustrate the results obtained, actuator color maps are presented. These maps show the mean value obtained for each actuator. In the case of the sets of 3 by 3 actuators, the mean value of each set is displayed on the actuator located at the centre of the 3 by 3 array.

The main results for the magnetic DM are presented in Fig. A.2. The values are quite different along the mirror surface. Statistics reveal a maximum single actuator stroke of 7.35 μm and a mean of 5.80 μm. For the 3 by 3 array of actuators, the membrane displacements are twice the value obtained for single actuators with a maximum of 15.31 μm and a mean of 12.47 μm. The 3 by 3 array map also presents an unexpected result with a drop in the centre of the membrane.

The main results for the piezo-stack DM are presented in Fig. A.3 for the tests at room temperature, in Fig. A.4 for the tests at 0°C and in Fig. A.5 for the tests at -35°C.

Statistics show a maximum of 5.69 μm and a mean of 5.47 μm for the single actuator maximum stroke measurements. For the 3 by 3 array of actuators, membrane displacements appear to be twice the value obtained for single actuators with a maximum of 12.74 μm and a mean of 11.83 μm.

The piezo-stack DM measurements for the 3 by 3 array of actuators match well the expected behaviour of the membrane where the central actuators tend to have more stroke than the edge actuators. The shape at rest varies greatly with temperature variation and the hysteresis at -35°C presents unexpected behaviour with a steep jump in vertical position around the centre position of the actuator.

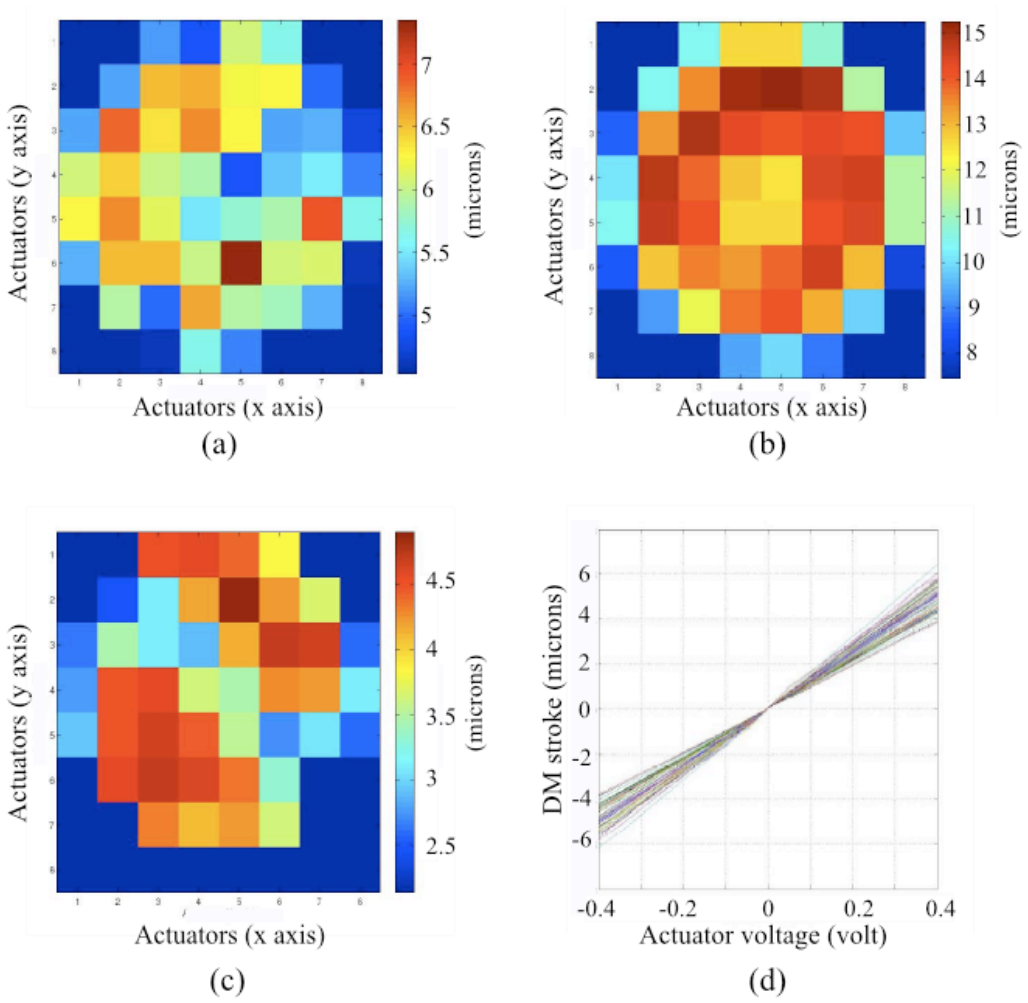

Figure A.2: *(a) Single actuator maximum stroke. (b) 3 by 3 maximum actuator stroke. (c) Vertical inter-actuator stroke. (d) Actuators linearity.*

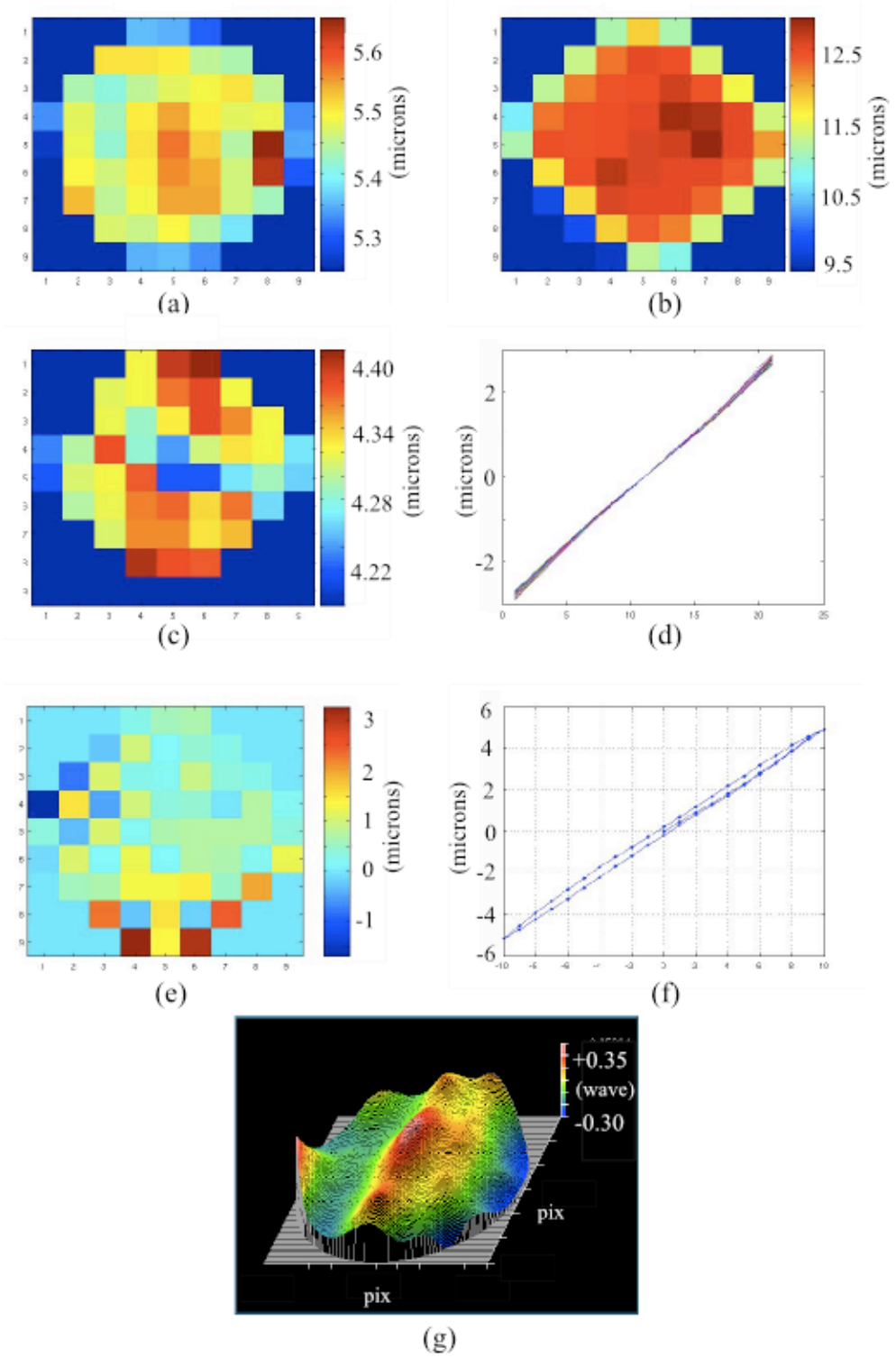

Figure A.3: *Piezo-stack DM tests at room temperature. (a) Single maximum actuator stroke. (b) 3 by 3 maximum actuator stroke (c) Vertical inter-actuator coupling. (d) Linearity. (e) Best flat. (f) Hysteresis. (g) Shape at rest.*

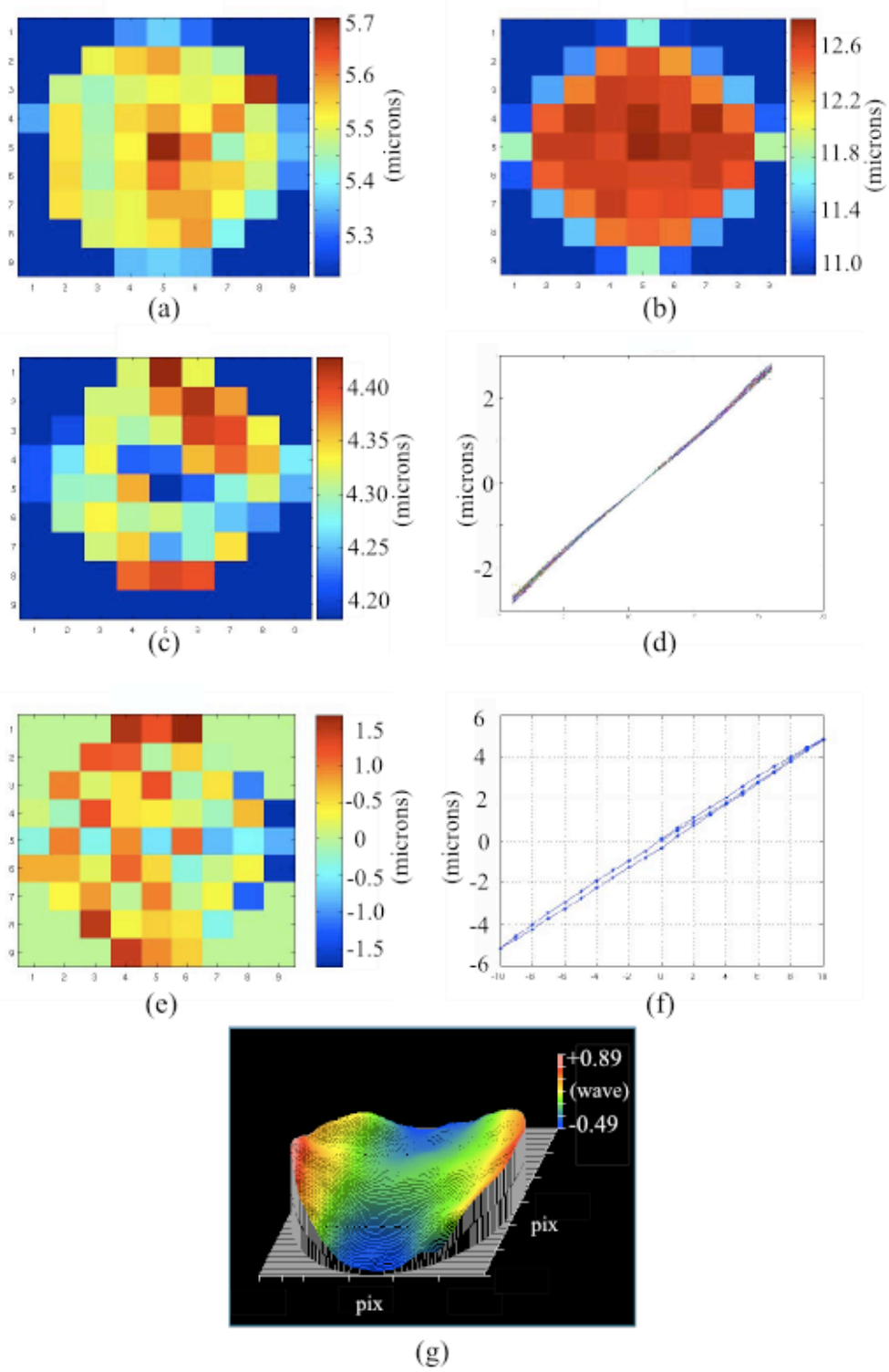

Figure A.4: *Piezo-stack DM test at 0°C. (a) Single maximum actuator stroke. (b) 3 by 3 maximum actuator stroke (c) Vertical inter-actuator coupling. (d) Linearity. (e) Best flat. (f) Hysteresis. (g) Shape at rest.*

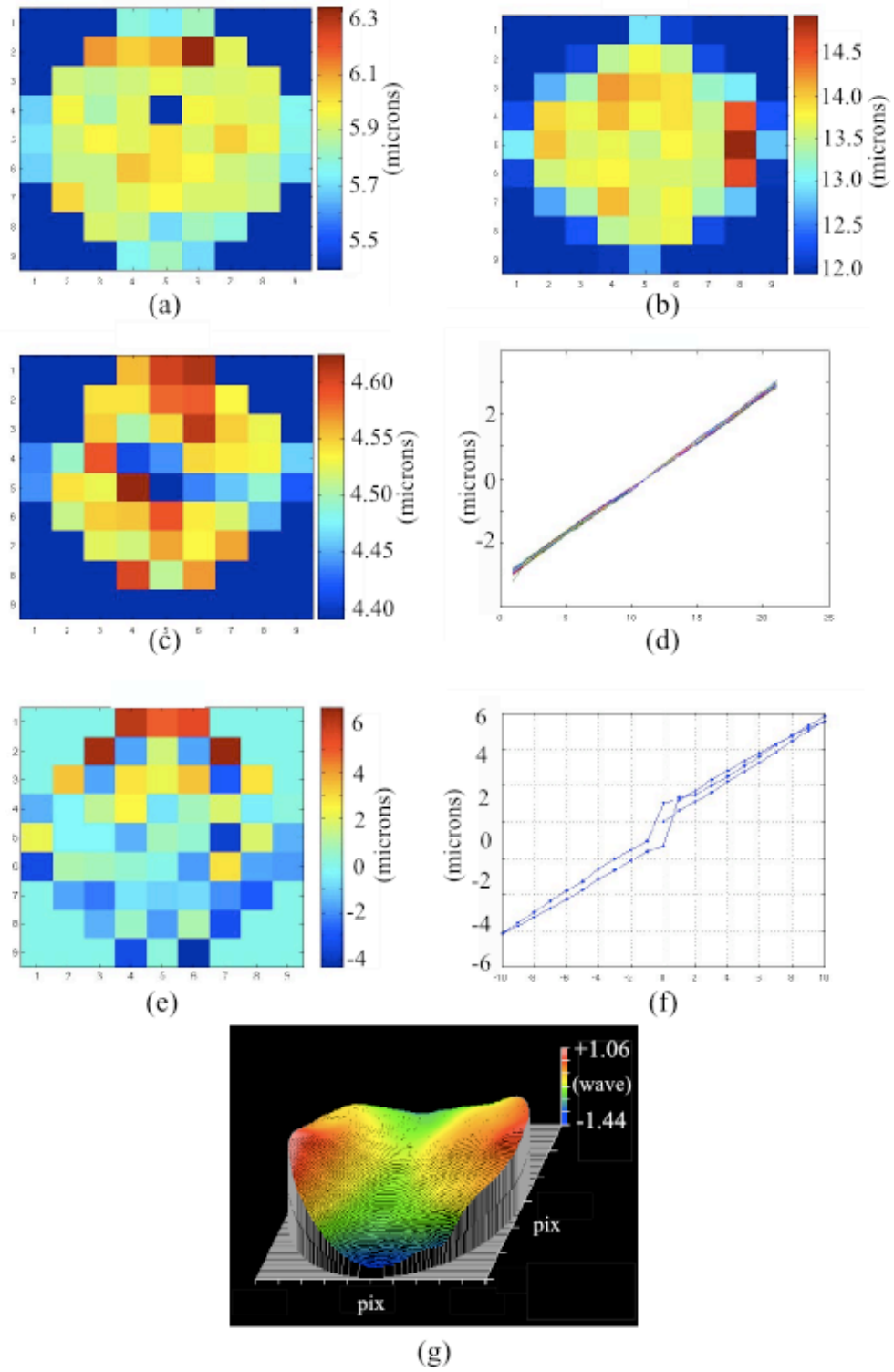

Figure A.5: *Piezo-stack DM test at −35°C. (a) Single maximum actuator stroke. (b) 3 by 3 maximum actuator stroke (c) Vertical inter-actuator coupling. (d) Linearity. (e) Best flat. (f) Hysteresis. (g) Shape at rest.*

Appendix B

Zernike polynomials

Zernike polynomials are a sequence of polynomials that are orthogonal to each other on a unit disk. In adaptive optics, they are widely used as a convenient basis of functions to describe the effect of the turbulence on the wavefront aberration over the circular pupil of the telescope[1]. This basis is convenient for AO, because it allows one to organize the modes by increasing spatial order.

As illustrated in Fig. B.1, the lower modes have the biggest contribution on wavefront aberration. Most of the turbulent energy can thus be grouped in the first low order-high power modes: the tip, the tilt, and the focus.

The first mode, named piston, cannot be measured by the WFS and, therefore, has no impact on the measurement of the turbulent phase. As the order of the modes increases, each mode contribution decreases. However, the sum of all the high order modes can slowly add up to the contribution of the first few low order modes.

Zernike polynomials have even and odd components which can be defined in polar coordinate as follow:

$$\begin{cases} m \neq 0, & Z_{i,even} = \sqrt{n+1} R_n^m(r) \sqrt{2} cos(m\theta) \\ m \neq 0, & Z_{i,odd} \ = \sqrt{n+1} R_n^m(r) \sqrt{2} sin(m\theta) \\ m = 0, & \qquad Z_i = \sqrt{n+1} R_n^0(r) \sqrt{2} \end{cases} \tag{B.1}$$

[1]Noll extended the work of Fried to develop a new way to use the Zernike polynomials to represent the Kolmogorov spectrum of turbulence, which allows to compute analytically the strength of the statistical aberrations.

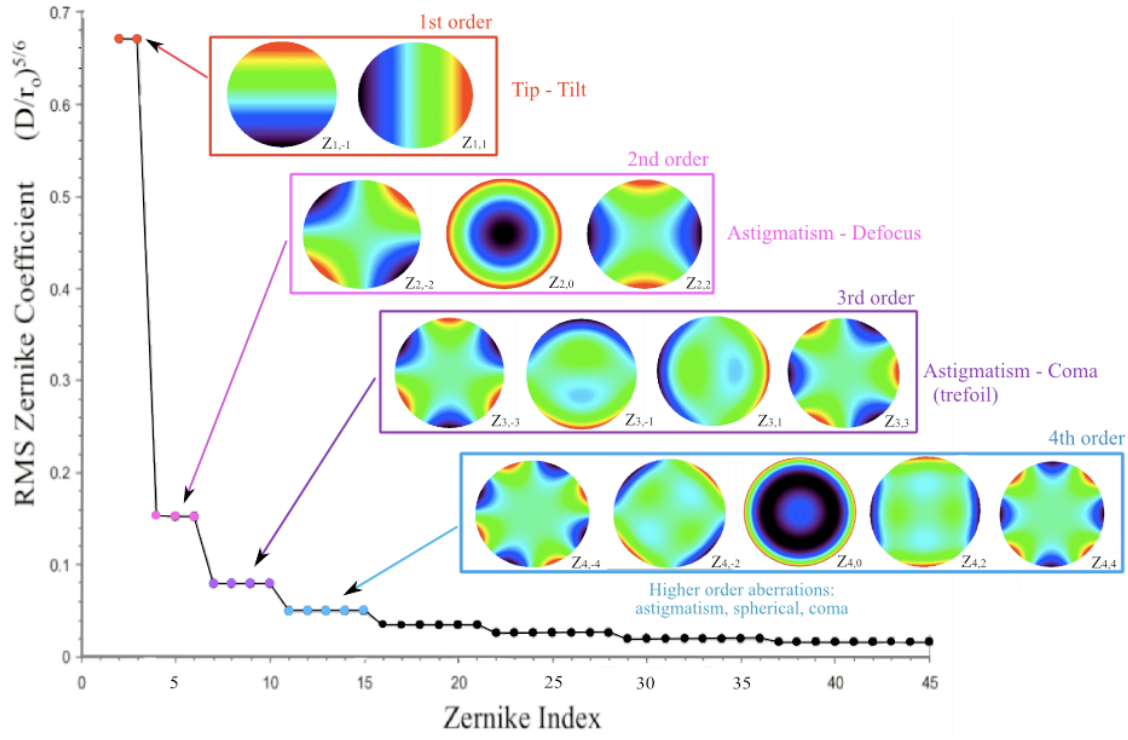

Figure B.1: *Representation of the wavefront shape for the first four orders Zernike polynomials and a plot of the RMS Zernike coefficient (the strength for atmospheric turbulence following Kolmogorov statistics) of the first 45 Zernikes.*

where $R_n^m(r)$ can be defined as:

$$R_n^m(r) = \sum_{s=0}^{(m-n)/2} \frac{(-1)^s (n-s)!}{s!((n+m)/2-s)!((n-m)/2-s)!} r^{n-2s} \tag{B.2}$$

with $n = 0, 1, 2, ...$, the radial degree and $m = 0, \pm 1, \pm 2, ...$, the azimuthal frequency. The indices n and m must satisfy $m \leq n$ and $n - m$ must be even.

The phase aberration can thus be decomposed using the Zernike polynomials basis as:

$$\phi_{turb}(r) = \sum_{i=2}^{\infty} a_i Z_i(r) \quad with \quad Z_i(r) = Z_n^m(r) \tag{B.3}$$

where a_i represents the coefficients of the Zernike polynomials for a given aberrated phase.